9-2021

Stochastic Satellite Air Drag with the Ballistic Coefficient as a Random Variable

Everett B. Palmer IV

Recommended Citation

Palmer, Everett B. IV, "Stochastic Satellite Air Drag with the Ballistic Coefficient as a Random Variable" (2021). *Theses and Dissertations*. 5091.
https://scholar.afit.edu/etd/5091

Stochastic Satellite Air Drag with the Ballistic Coefficient as a Random Variable

DISSERTATION

Everett B. Palmer IV, Major, USAF
AFIT-ENY-DS-21-S-103

DEPARTMENT OF THE AIR FORCE
AIR UNIVERSITY

AIR FORCE INSTITUTE OF TECHNOLOGY

Wright-Patterson Air Force Base, Ohio

AFIT-ENY-DS-21-S-103

STOCHASTIC SATELLITE AIR DRAG WITH THE BALLISTIC COEFFICIENT AS A RANDOM VARIABLE

DISSERTATION

Presented to the Faculty
Graduate School of Engineering and Management
Air Force Institute of Technology
Air University
Air Education and Training Command
in Partial Fulfillment of the Requirements for the
Degree of Doctor of Philosophy

Everett B. Palmer IV, BS, MS
Major, USAF

August 2021

AFIT-ENY-DS-21-S-103

STOCHASTIC SATELLITE AIR DRAG WITH THE BALLISTIC COEFFICIENT AS A RANDOM VARIABLE

DISSERTATION

Everett B. Palmer IV, BS, MS
Major, USAF

Committee Membership:

Dr. William E. Wiesel
Chairman

Dr. Richard G. Cobb
Member

Lt. Col. Kirk W. Johnson, PhD
Member

Dr. Clark N. Taylor
Member

ADEDJI B. BADIRU, PhD
Dean, Graduate School of Engineering and Management

AFIT-ENY-DS-21-S-103

Abstract

Predicting the orbits of satellites is a critical capability for organizations involved in space operations. It is often just as important to know how uncertain such a prediction is. Therefore, satellite prediction models must be capable of accurately reporting the uncertainty of their predictions if they are to be most useful.

The drag acceleration caused by the Earth's atmosphere is a significant cause of prediction uncertainty for low Earth orbit satellites. Most existing research has focused on improving deterministic atmospheric density predictions or on density as a random variable. This research investigates a new paradigm and focuses on modeling the uncertainty caused by air drag using the ballistic coefficient, a component of air drag that is independent of the model used to predict the density.

By considering the ballistic coefficient to be a random variable in a stochastic dynamical system, this research calculates time series of ballistic coefficient values and models them as random processes. These random processes are then used as the foundation of a stochastic satellite prediction model that, given observational data in the form of position and velocity vectors, calculates the parameters of the random processes and predicts satellite orbits with realistic uncertainty. The model is developed using the Unscented Transform and is validated using Monte Carlo simulation and empirical analysis.

Finally, the model proves effective for any choice of atmospheric density model and a variety of dynamical formulations. This validates the novel paradigm of this research and demonstrates that modeling the ballistic coefficient as a random variable can effectively model the overall prediction uncertainty of the underlying dynamics formulation.

AFIT-ENY-DS-21-S-103

For my wife and children.

Acknowledgements

I am extraordinarily grateful to my wife and children for their patience, support, sacrifice, and perseverance throughout this arduous endeavor. It has truly been a family effort, and any associated achievement is theirs as much as mine.

I'm also thankful for the mentorship of my advisor, Dr. William Wiesel, whose expertise and guidance have been invaluable.

Finally, I'd like to thank the other members of my research committee for their time and support.

Everett B. Palmer IV

Table of Contents

List of Figures

List of Tables

List of Abbreviations

ABM	Adams-Bashforth-Moulton
CDF	cumulative density function
CFSCC	Combined Force Space Component Command
CHAMP	Challenging Minisatellite Payload
DoD	Department of Defense
EA	empirical analysis
ECEF	Earth-centered, Earth-fixed
EKF	Extended Kalman Filter
GPIM	Green Propellant Infusion Mission
GPS	Global Positioning System
GRACE	Gravity Recovery and Climate Experiment
LEO	low Earth orbit
MC	Monte Carlo
PDF	probability density function
RP	random process
RTN	radial, transverse, normal
SDA	Space Domain Awareness
SGP4	Simplified General Perturbations-4
SOGM	second-order Gauss-Markov
SOS	Space Object Self-Tracker
SP	special perturbations
TLE	two-line element set
UKF	Unscented Kalman Filter
UT	Unscented Transform
UTC	Universal Time Coordinated

STOCHASTIC SATELLITE AIR DRAG WITH THE BALLISTIC COEFFICIENT AS A RANDOM VARIABLE

I. Introduction

Estimating the future positions and velocities of satellites is a critical competency for military, government, and civilian organizations. Accurate satellite orbit prediction enables or enhances Space Domain Awareness (SDA), conjunction analysis, mission planning, and other important functions [1]. (Note that the term "satellite" throughout this document refers generally to any resident space object orbiting the Earth and is used to aid readability.)

Tools for estimating the future state of a satellite are often referred to as orbit "prediction" or "propagation" methods and model the satellite's spatial and temporal behavior using a variety of dynamical system formulations. Some of these formulations leverage analytical expressions, while others require numerical integration of the system's differential equations of motion. The dynamics of an Earth-orbiting satellite are complex, dynamic, and subject to several perturbing external forces, and these attributes create decision points for anyone trying to model them.

Analytical methods, for example, often incorporate fewer physical phenomenon in their development than numerical methods (to make them tractable), and therefore tend to yield more approximate results. The benefit of analytical methods, however, is that they are generally faster to calculate than numerical methods. Numerical methods, contrarily, can model as many physical phenomena as desired, however there is a trade-off between accuracy and computational requirements (speed and stability) as equations of motion get more complex.

Even the most accurate numerical orbit propagators, regardless of their formulation, are not perfect in their results. This uncertainty has several causes, such as measurement error, unknown or ignored physical phenomena, or uncertainty within the environment. This reality—the impossibility of perfect estimates—implies that just predicting the future state of a satellite is not enough. The uncertainty of the estimate must also be characterized.

With respect to satellite predictions, the appropriate characterization of uncertainty depends on the underlying probability density function (PDF) (as any uncertain state prediction is really a random variable). If the initial uncertainty distribution is assumed to be Gaussian and the system dynamics are linearized, for example, uncertainty is exactly characterized by the covariance matrix of the multi-dimensional Gaussian random vector that is the estimate. In this case, the positional uncertainty of the satellite can be visualized as a three-dimensional ellipsoid [2, pg. 26]. While this is simple to understand and visualize, it is based on simplified, linearized dynamical systems and Gaussian assumptions, and it represents the true uncertainty of the estimate only so far as the linearization and Gaussian assumptions are valid.

Thus, keen interest in "uncertainty realism" has developed within the field of astrodynamics—that is characterizing the uncertainty of satellite predictions in a way that accurately reflects the "true" uncertainty. Performing astrodynamics work with realistic characterizations of uncertainty is critical. In the absence of uncertainty realism, conjunction analysis becomes less reliable, track correlation in the realm of SDA becomes difficult, tracking asset allocation and scheduling is ill-informed, and mission planning decisions may be misguided [1].

Uncertainty in a satellite state prediction is the result of many factors, including sensor inaccuracies, mismatches between the dynamics model and reality, and random or chaotic behavior within the satellite's environment [1]. Regarding the space environment, satellites in low Earth orbit (LEO) (those with a perigee of less than 2000 km [3], though there is little consensus on this value [4, pg. 37]) encounter air in the upper regions of Earth's atmosphere, and this air imparts a drag force on those satellites. A representation of the air drag acceleration on a satellite in LEO is [5, pg. 551]

$$\boldsymbol{a}_D = -\frac{1}{2}\frac{C_D A}{m}\rho \boldsymbol{v}_{\text{rel}} v_{\text{rel}} \tag{1}$$

$$\boldsymbol{a}_D = -B^* \rho \boldsymbol{v}_{\text{rel}} v_{\text{rel}} \tag{2}$$

where ρ is the air density, $\boldsymbol{v}_{\text{rel}}$ is the velocity of the spacecraft relative to the atmosphere and v_{rel} is its magnitude, A is the projected cross-sectional area, m is the mass, and C_D is the drag coefficient. The first three variables in Equation 1 and the leading $1/2$ are often grouped into a single parameter called the ballistic coefficient $B^* = (1/2)C_D A/m$ as in Equation 2 (defined here without the use of a reference air density as it sometimes is).

Every variable in Equation 2 is potentially uncertain to some degree, particularly when predicted into the future:

- C_D is an imperfectly known quantity in general, and is difficult to calculate accurately [6–8].

- For active satellites, the cross-sectional area A changes with satellite orientation or upon actuation of movable parts, and even if known at a given time by the operator may not be reliably predicted. For inactive satellites or debris A and its fluctuations may not be known at all.

- The mass m is likely known to some detail by the operator for active satellites, but fuel consumption or initial load-out may be imperfectly measured. Mass can also be difficult or impossible to determine for third-party satellites or debris.

- Air density ρ is uncertain due to modeling errors and the difficulty of predicting the behavior of the upper atmosphere, despite the significant levels of accuracy achieved by recent atmospheric models [8].
- Relative velocity v_{rel} is not perfectly known (even if the satellite's inertial velocity somehow is) due to uncertainty in the movements of gases in the upper atmosphere.

Therefore, while the exact probabilistic nature of the acceleration due to air drag may not be fully known, it is evident that the effect of air drag is uncertain to some degree. Further, because air drag acts in a direction opposite to the satellite's velocity vector relative to the atmosphere (which is close to the satellite's inertial velocity vector), its contribution to the uncertainty of a satellite prediction is applied almost entirely in the "in-track" direction. This has the effect of elongating the positional uncertainty of the satellite along the orbit path and implies that the orbit path is more well-known than the satellite's location on the path [9].

This insight has great bearing on uncertainty realism, as a prediction model which does not incorporate the effects of air drag on uncertainty will likely dramatically underestimate its prediction uncertainty along the orbit track. In light of this, the overall aim of this research is to assess the effects of air drag on prediction uncertainty and develop a novel method of ensuring prediction uncertainty characterizations realistically capture those effects.

1.1 Motivation

The principal motivator of this research is enhancing the uncertainty realism of LEO satellite state predictions via analysis of air drag as a dynamically stochastic effect. It is discussed above that some or all constituent variables of Equation 2 are uncertain to some degree, and given that many of these variables are time-varying (the air density and relative velocity, for example) uncertainty likely exists *within* the system's dynamics. If air drag is considered to be dynamically stochastic in the formulation of a satellite state prediction method, then the dynamical system's equations of motion become stochastic differential equations. Modeling the dynamics of the system as stochastic in this way, rather than as deterministic, is essential to generating satellite state estimates with realistic uncertainty characterizations [9–12].

Assuming that the system dynamics (particularly the effect of air drag) are stochastic raises additional questions with respect to building a satellite prediction model: because every variable of the air drag equation is potentially stochastic, the designer of such a model must decide which of these components to model stochastically and which to model deterministically. Modeling all variables as random variables greatly increases the complexity of uncertainty characterization due to the non-linear nature of their relationship in Equation 2. Additionally, the data available to a prediction model may or may not grant observability of the various terms, meaning that only certain combinations of terms may or may not be simultaneously estimated. As a result, existing prediction models that involve stochastic dynamics tend to consider only one component of air drag as a random variable, and allow the error associated with modeling other truly stochastic terms as deterministic to accumulate into the single random variable.

Most existing work considers the atmospheric density to be the lone random variable of air drag [6, 13–21]. Doing so seems intuitive since the behavior of the upper atmosphere is chaotic and difficult to predict, but developments which take this approach are generally tied to the atmospheric model used to calculate the air density or to a class of these models. While such prediction models can be effective and provide realistic characterizations of uncertainty, their linkage to specific atmospheric models and potential dependence on assumed random processes for either the density error or atmospheric model inputs limits their general applicability.

Ultimately, selecting only one component of air drag to model as a random variable leaves some uncertainty un-modeled, and those phenomena which are modeled stochastically are done so imperfectly (i.e. no atmospheric model output is exactly known, nor is the uncertainty of any such output). Therefore, regardless of which component of $\boldsymbol{a}_D$ is modeled stochastically, errors from the deterministically modeled components will accumulate in the uncertainty of the estimate [12]. Other efforts have attempted to rectify the potential mismatch caused by modeling a stochastic reality with deterministic dynamics via the use of covariance scaling methods or consider parameters, but scaling covariance matrices often requires manual tuning or other modeling assumptions, and consider parameters are generally more suited to time spans within the scope of available observational data than to prediction [21].

In summary, previous approaches either (a) work around or ignore the stochastics which are likely present within the dynamics (which makes such approaches ill-suited to prediction) or (b) consider the atmospheric density as a random variable, often assuming a random process model for the density error or atmospheric model inputs. Instead, this research is motivated by the possibility of a prediction method that produces realistic characterizations of uncertainty whilst remaining indifferent to the choice of atmospheric model and requiring no manual tuning of random process parameters or manual scaling of uncertainty characterizations. Ideally all information needed for the prediction model could be available on-board a satellite and require no operator input whatsoever.

Considering these desires, there is an insight to be gained from the discussion above: if accurate estimates with realistic characterizations of uncertainty can be obtained by modeling only one component of $\boldsymbol{a}_D$ as a random variable, then choosing the ballistic coefficient B^* as that single random variable makes a great deal of sense [9]. A prediction model that considers B^* as the only random variable would have the following novel benefits:

- Interoperability with a wide range of atmospheric density models.
- Adaptability to various dynamics formulations and perturbation forces.
- Dependence on observational data to inform the parameters of the random process within the stochastic dynamics, rather than assuming them
- Adaptability to on-board use if regular observational data is available (from an on-board Global Positioning System (GPS) receiver, for example).

It is these potential advantages of modeling B^* as the only random variable in a stochastic satellite prediction model that are the principal motivation of this research.

1.2 Research Hypotheses and Tasks

1.2.1 Research Hypotheses

The preceding section made several assertions, which are summarized here as the research's hypotheses:

1. Air drag is the principal source of model prediction uncertainty for LEO satellites.

2. The ballistic coefficient B^* can be analyzed as a stochastic process and parameterized via analysis of a time-series of B^* estimates calculated from observational data.

3. A stochastic prediction model which models aerodynamic uncertainty using B^* as the only random variable of air drag can produce accurate predictions with realistic uncertainty.

The following section enumerates the research tasks that were undertaken in assessing these hypotheses.

1.2.2 Research Tasks

The research introduced above was organized around completing the following research tasks:

1. Confirm the effect of air drag on model prediction uncertainty via analysis of the time-growth of covariance matrices calculated from observational data (referred to below as “empirical covariance analysis”).

2. Calculate and analyze a time-series of ballistic coefficient B^* values, characterize the resulting B^* random process, and construct a method of parameterizing the random process using the B^* time series.

3. Create a B^* random process generator which generates realizations of said random processes.

4. Develop a dynamically stochastic prediction model which, given initial conditions and previously estimated B^* random process parameters, predicts the

future state of a satellite and provides a realistic characterization of the prediction's uncertainty, considering only B^* to be a random constituent variable of air drag.

5. Validate the stochastic prediction model using Monte Carlo simulation.

1.3 Summary of Literature Review

A robust review of current literature on the aforementioned topics is presented in Chapter II. A summary of this review is presented here to facilitate the discussion of research contributions in the next section.

The introduction of the literature review briefly discusses the foundations of orbit estimation [22, 23], and re-emphasizes the importance of accurate orbit estimation and the realistic characterization of estimate uncertainty [1]. Deterministic orbit estimation methods (methods using only deterministic dynamics models) are then reviewed, including general perturbations [19, 24–47], SP methods [5, 48–52], and hybrid/semi-analytical methods [53–56].

Next, the generation and deterministic propagation of estimate uncertainty is reviewed. The phrase "deterministic propagation of uncertainty" seems paradoxical, but it refers to propagating some initial characterization of an estimate's uncertainty to a different time using *deterministic* dynamics models. Until quite recently, the majority of uncertainty characterizations were propagated this way using a variety of methods [57–85]. This section of the literature review also discusses methods of generating an approximate estimate uncertainty using different types of available data [9, 86–91].

The concept of *stochastic* orbit estimation (orbit estimation using dynamics models which include uncertainty) is then introduced and reviewed and is of the most interest to this research and the upcoming section regarding its originality.

One topic that is related, but ancillary to, this research is "density calibration", or using satellite data to improve atmospheric density models, develop new models, or refine density calculations for scientific purposes [92–97]. Atmospheric density is the focus of most existing research in stochastic orbit estimation, the bulk of which considers atmospheric density ρ in Equation 2 to be the only uncertain variable in the system's dynamics [6, 11–21]. A smaller number of research efforts have considered the ballistic coefficient B^* as an uncertain variable [18, 94]. Some of this work is based on Wright and Woodburn's development of a method which considered both ρ and B^* to be uncertain and estimated them simultaneously using a batch method [94, 98]. Multiple researchers have also explored the linkage between dynamical uncertainty of air drag and positional uncertainty [9–12, 14, 20, 99], while others have shown the effects of uncertain air drag on positional uncertainty using only deterministic dynamics [100–102]. Finally, while many of the aforementioned methods attempt to estimate (solve-for) one or more uncertain variables (such as ρ or B^*), Markley developed the use of "consider parameters" (variables which are considered uncertain for the purpose of uncertainty characterization but which are not estimated) in orbit estimation [103, 104]. Consider parameters are currently in use by the Department of Defense (DoD), as well [1, 17].

Finally, a critical component of realistic uncertainty characterizations is the coordinate frame in which the state estimate is resolved, and various choices of coordinate frame and how the choice of coordinate frame affects underlying probability distributions are reviewed [9, 62, 63, 105–110].

1.4 Contributions

The following novel contributions to the field of astrodynamics are described in this research and are summarized here for reference.

The first contribution is expanded confirmation that air drag is a dominant source of prediction uncertainty for LEO satellites. This is significant for the research hypotheses because two SP prediction models with very different atmospheric models calculate essentially the same empirical uncertainty when estimating B^* as an augmented element of the state vector, as is detailed in Chapter IV. This contribution is distinct from previous work [9, 86–91] in that this research considers multiple satellites, additional prediction methods including analytical and special perturbations varieties, and more robust observational data.

The second contribution of this research is the analysis of B^* as a random process based upon calculation of time-series of B^* estimates derived from robust observational data. This is the first analysis of the behavior of B^* as a random process derived from observational data and the first application of such an analysis to satellite prediction model uncertainty. While previous research efforts have utilized stochastic satellite dynamics and modeled the atmospheric density error or ballistic coefficient as a Gauss-Markov process [14–16, 94], Ornstein-Uhlenbeck process [6], or other (i.e. manually tuned white noise, Brownian motion, etc.) process [12, 18, 91], these processes have been selected using either assumptive or theoretical justifications. One exception is the work of Rich et al., wherein B^* values from a selection of two-line element sets (TLEs) were used to create a histogram that was fit with a Gaussian PDF to help justify the assumption that the B^* random process is likely Gauss-Markov. However, none of these previous efforts have used satellite data to construct a time-series of B^* estimates, and from this analyze and parameterize the B^* random process.

The final contribution of this research is a stochastic satellite prediction model which provides realistic uncertainty characterizations considering B^* as the only dynamically random variable. A principal advantage of this model compared with previous efforts is that it permits any choice of atmospheric model. This includes atmospheric models which do not require external data (such as indices of solar activity) to function, making the model potentially viable for on-board use if a GPS receiver is available. The model can also include a variety of perturbing forces (third body perturbations, etc.)—the only restriction on the dynamics is the use of an air drag model described by Equation 2, which is very common. This contribution is distinct from previous work in dynamically stochastic orbit estimation, the bulk of which focuses on modeling the atmospheric density or the solar inputs to atmospheric models as uncertain, rather than only the ballistic coefficient [6, 10–21, 99] or requires some manual tuning or assumptions regarding random process parameters [91, 94, 98]. This research is also distinct from the work of Rich et al. [9], which does consider B^* as the only uncertain variable, as their work used only TLEs and Simplified General Perturbations-4 (SGP4) to assert the stochastic nature of B^* and did not build a prediction method.

1.5 Document Outline

The remainder of this document is structured in the following way. The next chapter presents a review of previous literature in the field. Chapter III then discusses several topics that are relevant to multiple or all of the subsequent chapters.

The following three chapters (Chapters IV—VI) are structured such that each one covers a single main research concept and details the methodology, results, and conclusions relating to that concept. These three concepts are the analysis of empirically calculated prediction covariance matrices, the analysis of the ballistic coefficient as a dynamically random process, and the development of the stochastic prediction model. Finally, conclusions are presented in Chapter VII, followed by appendices and the bibliography.

II. Literature Review

2.1 Introduction

The study of astrodynamics and the prediction of orbits can trace its roots to antiquity [22], and much work has been done in the field over the successive centuries. Before Newton, Kepler derived his three laws of planetary motion and solved the two-body problem with his famous equation in the early 17th century [22]. Gauss then developed a method for estimating an orbit using observational data when he successfully predicted the orbit of the asteroid Ceres in 1801 [23]. Gauss realized that the measurements used to predict Ceres' orbit were imperfect, however the astrodynamics used were deterministic.

While these and other foundational advances were concerned with predicting the positions of the celestial bodies, astrodynamics and orbit prediction surged in importance with the dawn of the space age in the 1950s. As humankind launched its first artificial Earth-orbiting satellites, ways to accurately model their dynamics and predict their positions were needed and developed. These methods have been expanded and refined in the successive decades, and many are currently employed to track and control (if possible) the 23,287 tracked objects in Earth orbit (as of June 1, 2021) [111].

The ever-increasing number of satellites and debris in Earth orbit have made orbit prediction an engineering necessity. Being able to accurately predict a satellite's location and motion is fundamental to avoiding conjunctions, pointing ground-based control and tracking equipment, mission planning, communication, and analyzing scientific data. However, it is not possible to know the *exact* value of any physical quantity (such as the position and velocity of a satellite) because all measurements are beset with some level of error and uncertainty, models constructed to emulate physical realities are imperfect, and the physical reality itself often contains elements of random chance. Therefore, it is essential to recognize that any predicted satellite state is an *estimate*, and also to have some measure of how good that estimate is. The accurate quantification of uncertainty, then, is critical to useful orbit prediction [1].

Uncertainty in satellite orbit prediction comes from many sources, such as measurement errors, imperfectly known physical quantities, internal dissipative forces, and the unpredictable space environment. One particular component of the LEO space environment that is difficult to predict is air drag. Despite advances in modeling the behavior of the outer atmosphere, a certain amount of unpredictability appears to be inescapable. Despite employing advanced atmospheric models to predict the behavior of the atmosphere, some methods of orbit prediction ignore the inherent uncertainty in air drag by propagating satellite orbits as though drag effects were perfectly known (as if they were *deterministic* when they are likely *stochastic*) [9]. A good deal of air drag research remains rooted in the same determinism as the origins of astrodynamics.

In the following subsections, current methods of deterministic orbit prediction and deterministic propagation of uncertainty are reviewed. Then, dynamically stochastic orbit prediction methods are considered. Finally, research regarding the effects of coordinate frames on orbit estimation is reviewed, as are current widely available orbit prediction models.

2.2 Deterministic Orbit Propagation

There are two general categories of satellite orbit prediction methods. "General perturbation" methods are based on (often simplified) analytical perturbation theory and can usually be applied to an entire class of satellite orbits (hence "general”), while “special perturbations” methods are based on numerically integrating the dynamical system’s differential equations of motion, and generally only apply to the satellite orbit for which the initial conditions are valid (hence “special”). A third category also exists, and consists of hybrid methods which incorporate combinations of general perturbations, special perturbations, and other techniques.

2.2.1 General Perturbations

Though earlier formulations were used during the first years of satellite tracking [24], the analytical foundations of many implementations of general perturbations are established in the works of Brouwer [25] and Kozai [26]. These analytical satellite theories were updated over the years by many contributors, including an improvement by Lyddane [27] to remove some mathematical singularities and the addition of terms to account for air drag, and were eventually synthesized into an implementation known as Simplified General Perturbations [24]. An analytical model for atmospheric density that improved drag calculations was thereafter developed by Lane and Cranford, and was implemented in 1969. By that time, however, the number of satellites to catalog had grown to the point that available computers lacked the processing to implement the full model, and the model was simplified significantly to create SGP4, deployed operationally in 1970 [24]. All of this development was under the auspices of project SPACETRACK [24], and detailed development of the 1970 implementation of SGP4 was published by Lane and Hoots in SPACETRACK Report No. 2 [28].

After the launch of the first “deep space” satellites (those with a period of greater than 225 minutes), SGP4 was updated to include effects of the Moon, the Sun, and some Earth resonance terms [24]. Details of this updated version of SGP4 were published by Hoots and Roehrich [29], and a version of the model is still used today by Combined Force Space Component Command (CFSCC) to create the publicly available satellite catalog in the form of TLEs [30].

Although SGP4 is the analytical model in use by CFSCC and the only recommended propagation method for CFSCC TLEs [30], the current version has been updated substantially since its implementation in 1979 [32]. For those wishing to implement SGP4, source code which is believed to closely represent the CFSCC implementation is provided by Vallado in multiple programming languages [31, 32]. Compiled libraries of the actual CFSCC implementation are also available from CFSCC's public website [30].

While SGP4 is a common analytical method of orbit propagation in use today, it is certainly not the only one. Although special perturbations is typically regarded as achieving higher accuracy than general perturbations, the analytical methods of general perturbations can often produce results of acceptable accuracy using fewer computational resources. The computational efficiency of general perturbation methods can be particularly desirable for predicting large numbers of satellites for purposes such as cataloging and conjunction analysis [33].

Wnuk provides an informative review of various advancements in analytical orbit theories (up to 1999) as they relate to perturbations caused by the Earth's non-spherical geopotential and the effects of various resonant periods with the Earth's rotation [33]. Advances in the treatment of Earth's gravitational potential (the "geopotential") start with the aforementioned work of Brouwer [25] and Lyddane [27], which were first-order theories incorporating only the second and fourth zonal harmonics [33], then progress through the works to extend this theory to higher orders by Kozai [112], Deprit and Rom [34], Aksnes [35], Kinoshita [36], and Coffey and Deprit [37], before culminating in Wnuk's own general formulation [33] and Breiter's more recent second-order theory to arbitrary degree in the geopotential [38].

With respect to resonance effects, Wnuk notes that the general solution of the perturbation effects due to all resonances remains unsolved, despite the work of many others regarding resonances in the geopotential [33] and other recent advancements by Sochilina [39], Lane [40], and Delhaise and Henrard [41]. These advancements, while distinct, generally seek to provide a fundamentally similar type of solution—an analytical perturbation method which (by incorporating more complex perturbations) is more accurate while remaining non-singular.

Another particular class of analytical general perturbation methods which has seen recent advancements involves transforming the Newtonian form of the perturbed two-body problem by way of a time transformation and use of Kustaanheimo-Stiefel (K-S) coordinates using the method presented by Scheifele and Stiefel [19]. Bond derived perturbed K-S canonical equations using variation of parameters which permits perturbations that can be derived from a potential function and those which cannot, though the resulting equations were not solved in closed form and must be numerically integrated [42]. Engels and Junkins also used K-S coordinates to formulate a solution to Lambert's problem (finding the initial velocity given a satellite's initial and final positions) that can be solved analytically up to inclusion of the J_2 ("oblateness") term [43]. Raj and Sharma have developed a non-singular analytical method using K-S canonical equations that incorporates the J_2, J_3, and J_4 zonal harmonics for short-term periodic orbits which agrees with a numerically integrated solution to within tens of meters [113]. This is based on Sharma's earlier analytical theory which incorporated the J_2 oblateness term and air drag [45]. More recent work by Raj and Sharma applies the K-S canonical equations to obtain a non-singular analytical solution to long-term orbits incorporating Earth's oblateness and air drag (using a spherical atmosphere) [44].

Other recent developments in general perturbations include those of Martinusi et al., who developed a non-singular analytical propagation method for low eccentricity, near Earth satellites which incorporates the Earth's oblateness and air drag, using the equinoctial elements and "averaging" the equations of motion [46]. Lara et al. have examined the 3 to 5 tesseral resonance ratio as it applies to the constellation of Galileo satellites, which can be done analytically by itself or coupled with numerical integration when the perturbation effects of the Moon and Sun are included [47] (hybridization of general and special perturbations is reviewed in Section 2.2.3).

2.2.2 Special Perturbations

Special perturbations as a category of orbit propagation methods encompasses a vast diversity of implementations. Since special perturbations generally refers to any propagation method which numerically integrates the satellite's equations of motion, the array of implementations is as varied as the possible combinations of satellite equations of motion and numerical integration schemes.

Far too many formulations exist to review them all here, however a good starting place for a review may be the work of Montenbruck, which compares various numerical integration methods available circa 1992 and assesses their applicability to orbit propagation of celestial bodies and Earth satellites. This work compared various single-step, multi-step, and extrapolation methods and found that multistep methods are generally preferable [48].

It is also worthwhile to note that special perturbation methods often leverage one of two general formulation types: Cowell's Method, in which the equations of motion are integrated directly, or Encke's Method, in which a nominal two-body problem is calculated via a known solution and the error between this reference trajectory and the more detailed dynamics models is solved for numerically [5, pg. 523].

Work on new and improved special perturbation techniques continues. For example, Bradley et al. developed a new technique that employs "generalized Gaussian quadratures" coupled with a collocation method instead of polynomials with an implicit Runge-Kutta integration, to decrease the computational resources required of special perturbations to keep pace with the increasing size of the satellite catalog. Results showed that the new method is (for the case of LEO satellites) equally or more efficient than other currently utilized numerical integration techniques, with further expected improvements if the implementation is optimized for parallel processing [49, 50].

In a 2012 survey of numerical propagation methods, Jones and Anderson reference the historical foundations of some methods commonly in use today (noting that "special perturbation propagation of the Air Force space object catalog relies on the Gauss-Jackson integrator first presented in 1924") before reviewing newer approaches which use either a symplectic formulation of the Hamiltonian dynamics or collocation methods (as in Bradley et al., from above). Their work showed that collocation methods are effective and relevant for application to astrodynamic numerical integration problems like special perturbations of Earth satellites and that while symplectic methods showed promise, more work was needed before they could be readily applied to such problems [51].

It is worthwhile to note that while most perturbations methods (general or special) use the classical Keplerian two-body problem as the fundamental problem (with known solution) which is then perturbed, any sound mathematical satellite model which can be formulated as a system of ordinary differential equations can be used with special perturbations. For example, Wiesel has developed a theory for nearly circular drag-free orbits using periodic orbits and the full zonal geopotential as the fundamental problem, achieving meter-level agreement for at least one numerical experiment [52].

2.2.3 Semi-Analytical Methods

Recently, semi-analytical or "hybrid" methods have been employed to merge the computational efficiency of analytical methods and the high accuracy of numerical integration together. As more and more orbiting objects need to be tracked and cataloged by various agencies concerned with SDA, fast but accurate methods of orbit propagation are desirable. Additionally, the precision required of a propagation method varies by task, which suggests that a method which is adjustable concerning the output accuracy and, by association, computation time could be valuable [53].

For example, the Draper Semi-analytical Satellite Theory (DSST) Standalone Orbit Propagator Package is a semi-analytical propagator for which development started in 1984 and that has been improved as reported by Neelon et al. to include the Earth geopotential up to order and degree 50, tidal motion, and enhancements to the modeling of short-term periodic motion [54].

Setty et al. compared an improved version of the DSST to high-fidelity numerical integration methods for a variety of orbit altitudes, eccentricities, and inclinations. The results of this comparison showed that the DSST semi-analytical method achieved the required accuracy with computational savings of 70-90% compared to pure special perturbations. Their work also examined the feasibility of the DSST method within the context of maintaining the entire space catalog, concluding that doing so results in vast computational savings at the cost of propagation accuracy, but that the resulting propagations were accurate enough for general SDA requirements. The results were not compared directly with CFSCC's current TLE public catalog [53].

Additionally, Lara et al. have applied the semi-analytical approach to the long-term effects of third-body perturbations. After considering the short-term periodic effects analytically, the remaining system can be numerically integrated using "very long time-steps" at significant computational savings [55]. Recently, Nie et al. similarly applied semi-analytical theory to the general third-body perturbation problem, but improved the results by altering the averaging method applied to the analytical portion [56].

Notably, all of the above analytical theories treat the dynamical propagation of a satellite's state deterministically.

2.3 Generation and Propagation of Uncertainty

The previous section reviewed deterministic methods of propagating a satellite orbit. The term *deterministic* implies that the dynamical process is perfectly known—that there is no uncertainty—so what is meant by the phrase "propagation of uncertainty"? While it is true that in a deterministic prediction model the mathematics of the dynamics are assumed to be perfectly known, there is no guarantee (in fact it would be quite impossible in reality) that the original satellite state estimate to be propagated is perfectly known. In other words, even a deterministically propagated orbit will have uncertainty associated with it, and this uncertainty should not be expected to remain constant—it also must be propagated through time.

2.3.1 Generation of Uncertainty

Before the uncertainty of a satellite state estimate can be propagated, a characterization of the uncertainty must be available. This section reviews methods of characterizing the uncertainty of an orbit estimate.

One relevant type of uncertainty is *model prediction uncertainty*, the uncertainty due to errors in the prediction method itself (from mis-modeled dynamics or excluded physical phenomena, for example). Calculating a true prediction uncertainty can be difficult because obtaining the true error between a prediction and the true satellite state is often impossible, however methods exist for estimating the prediction uncertainty using available data.

Many researchers have used public information in the form of TLEs published by CFSCC to generate covariance matrices and analyze the prediction uncertainty of satellite orbits. This is necessary because covariance information is not provided with published TLEs [86]. Peterson et al., for example, generated estimated covariances via pair-wise differencing using TLEs alone [87]. More recently, Geul et al. proposed a new method of estimating covariance matrices from TLE data which removed some of the earlier results' difficulties with time bias [88].

The choice of coordinate frame when estimating covariance matrices greatly influences their subsequent analysis. Resolving a covariance matrix in the inertial frame (as in the above efforts), for example, makes assessing the uncertainty in the satellite-orbit frame directions quite difficult. Osweiler, however, estimated covariances using TLEs but resolved the errors in a radial, in-track, and cross-track coordinate frame [89]. Rich et al. expanded Osweiler's effort but calculated the in-track error separately before calculating the out-of-track errors in a rotated orbital coordinate frame, which isolated in-track error growth for analysis [9].

While the above efforts used TLEs exclusively, others have used more precise orbit data to analyze satellite prediction errors. Kelso used precision ephemerides of GPS satellites to investigate the validity of prediction covariances generated using the method of Peterson et al., and discovered biases in them [86]. Hyeon-Jeong and Dae-Won used high-precision data from the KOMPSAT-2 satellite to validate covariances generated using Osweiler's TLE method and concluded that TLE-generated covariances were sufficient for preliminary analysis, but that time-shift biases were present [90]. They appear to have used the same coordinate frame as Osweiler, and while the results show that the largest errors are in-track, they also exhibit large radial errors.

Additionally, Hesar et al. detail a method of generating realistic prediction covariances for the NASA GPM spacecraft called the Covariance Realism Tool (CRT), which has been operating since early 2017. CRT works by first performing an "overlap comparison analysis" that compares a precise orbit-determination solution to propagated satellite states to form an initial covariance [91]. The method also adds "process noise" into the propagation, and this is discussed in Section 2.4.

Another relevant type of uncertainty is *orbit estimation uncertainty*, which is the result of estimating the orbit of a satellite from imperfect observational data. Due to measurement errors and mis-modeled or un-modeled dynamics, the result of an orbit determination method is an orbit estimate with some error with respect to the true state, and this error is the root of uncertainty in the estimate.

One common method of orbit estimation, weighted non-linear least squares (which originated with Gauss), produces the covariance of its estimate directly as an output of the algorithm [2, pg. 72]. In addition to these "theoretical state error covariances", Frisbee has developed a method of calculating an empirical covariance matrix from the observational data and asserts that mismatches between this method and least squares may indicate significant modeling or measurement errors [114].

While weighted least squares is a batch method that ingests all available observations to produce a state estimate, sequential estimation methods also exist. There are many varieties, from the Bayes filter which takes as input a previous estimate and its associated covariance along with the data to the fully-sequential Kalman family of filters that ingest observations individually. Though many varieties of the Kalman filter exist and can be used in orbit determination, the key similarity is that they output a state estimate and an associated covariance.

2.3.2 Propagation of Uncertainty

Once the uncertainty of a satellite state estimate is known, propagating it forward in time is possible via several methods. In this context, uncertainty propagation refers to *deterministically* propagating estimate uncertainty to another point in time, versus the upcoming discussion in Section 2.4 which reviews fully stochastic satellite state estimation methods in which dynamical uncertainty is incorporated into the prediction.

First, it should be noted that while uncertainty is often characterized by a covariance matrix, this implies that the underlying probability density function is a multi-dimensional Gaussian, and is thus sufficiently described by the mean and covariance [115]. This is not necessarily the case for satellite orbit prediction, even if the initial uncertainty is Gaussian, due to the non-linear dynamics involved. Many of the methods discussed below are applicable only if the dynamics are linearized and all PDFs are Gaussian (or assumed to be Gaussian), while others can be applied to fully non-linear models and arbitrary PDFs. If employing a method which linearizes the system in some way and assumes Gaussian PDFs, the more general term “uncertainty” is typically replaced by the “covariance” matrix of the

Gaussian distribution.

Many methods of propagating uncertainty exist and are reviewed quite thoroughly by Luo and Yang [57]. Many of the methods described below are summarized in their review. Broadly speaking, propagation methods fall into two general categories: those that require linearization of the system and those that do not.

2.3.2.1 Linearization Methods

Typically, methods which require linearization of the system dynamics do so in conjunction with the assumption that all PDFs are Gaussian [57]. Doing so often greatly simplifies uncertainty propagation, as the PDF of a Gaussian distribution is fully described by the mean and covariance matrix and remains Gaussian after a linear transformation [115].

Perhaps one of the most well-known examples of propagating a covariance matrix is by way of a Kalman-type filter, such as an extended Kalman filter in which the dynamics are linearized and the error between the linearized solution and a reference solution is estimated [116]. This type of linearization, wherein the system dynamics are linearized, is termed “local linearization” by Luo and Yang [57]. Linearizing the system dynamics usually consists of evaluating the Jacobian of the deterministic dynamics at one or many linearization points.

This type of linearization method was applied by Geller and Geller et al. in the context of autonomous orbital rendezvous [58, 59]. Lee et al. also applied this type of linearization in developing an analytical method of calculating the uncertainty in the position of a deputy satellite in satellite formation flying [60].

2.3.2.2 Non-Linearization Methods

Methods that do not linearize the system can sometimes offer greater accuracy than linearization methods at the expense of greater computation time [57].

A well-researched and often used non-linear method is Monte Carlo (MC) simulation, in which many random samples of the uncertain system are propagated using the full non-linear dynamics. The distribution of these random samples very closely approximates the arbitrary PDF of the uncertain estimate when the number of samples is large, via the Law of Large Numbers. This concept also forms the basis of the propagation step of the particle filter [117].

As accurate Monte Carlo simulation requires a large number of samples to effectively approximate the estimate's PDF, the method is computationally expensive. Arora et al. recently developed an orbital propagation tool that used Monte Carlo simulation and parallel processing on a graphics processing unit to dramatically speed-up the method [61].

Several researchers have concluded that orbital prediction errors (and therefore estimate uncertainty) become non-Gaussian when the propagation time is large due to the non-linear dynamics [62–65], though this is somewhat dependent on the choice of coordinates (see Section 2.5). This inherent non-linearity of orbital mechanics is the key motivating factor for using methods which require less-restrictive PDF assumptions, like Monte Carlo methods and many of the other types of methods described below.

One method of incorporating non-linear dynamics and non-Gaussian PDFs without using the computational resources required by Monte Carlo methods is to approximate a non-Gaussian PDF as the weighted sum of Gaussian PDFs using Gaussian mixture models [66]. In a Gaussian mixture, the mean and covariance matrix of each Gaussian random variable is propagated and the weights are chosen via some numerical optimization method. The method of determining these weights is the focus of more recent research on Gaussian mixture models. Various methods and implementations of Gaussian mixture models were proposed by Terejanu et al. in their original paper [66], by Horwood et al. [67], and DeMars and DeMars et al. [68–70].

Another way to handle the non-linearity of orbital dynamics in propagating uncertainty is to employ the Unscented Transform (UT) developed by Julier et al. (which forms the basis of the Unscented Kalman Filter (UKF)), the premise of which is to approximately fit a Gaussian to the propagated distribution of key "sigma points" rather than approximate the system's dynamics via linearization [71, 72]. With regard to orbital dynamics, Raihan and Chakravorty designed a hybrid estimator using a UKF and Monte Carlo methods for space object tracking [73].

Polynomial chaos methods represent another tool for handling non-linear dynamics when propagating estimate uncertainty [118]. Such methods, applied to stochastic differential equations by Xiu and Karniadakis [74] and to the propagation of orbit estimation uncertainty by Jones et al. [75], can utilize existing propagators as a "black box", including orbital non-linearities [57]. Jones et al. and others have also applied polynomial chaos methods to collision probability estimation that is not based on Gaussian assumptions [76, 77].

Whereas most non-linearization methods rely on numerical solutions in some way, there exist analytical methods of propagating estimate uncertainty which are based on higher-order Taylor series approximations of the non-linear dynamics. These higher-order Taylor series approximations (versus first-order in the linearization case) result in "state transition tensors" which are used to propagate a Gaussian mean and covariance in a non-linear manner, as in the work of Park and Scheeres [78, 79]. State transition tensors are also used by Majji et al. for the higher-order "j^{th}-Moment Extended Kalman Filter", which is then applied to orbit estimation given sparse measurements [80]. Park also used state transition tensors, coupled with a purposefully simplified dynamics model, to analytically and non-linearly propagate satellite estimate uncertainty [81, 82].

2.3.2.3 Hybrid Methods

Other approaches for propagating uncertainty exist which are hybrids of aforementioned methods.

Jones and Weisman, for instance, recently developed a hybrid method of uncertainty propagation that uses a quick, but less accurate, "low-fidelity" solver to propagate a particle ensemble and then identify the most important members of the ensemble for re-propagation using a more computationally expensive, but much more accurate, "high-fidelity" solver [83].

Another hybrid application which leverages Monte Carlo methods is that of Aristoff et al., wherein an implicit Runge-Kutta method is used to propagate the ensemble of particles collectively rather than propagating each particle individually by noting that the propagation problems have similar initial conditions and are otherwise identical, resulting in significant computational savings [84].

A third hybrid method is that of DeMars, which applies a synergistic approach to the problem of uncertainty propagation in developing a new algorithm for uncertainty propagation called the "splitting Gaussian mixture unscented Kalman filter" which detects when a non-linear prediction of uncertainty disagrees sufficiently with a simpler linear prediction, and only then applies a splitting Gaussian mixture algorithm to account for the non-linearities [68].

Finally, Vittaldev et al. developed a hybrid method composed of Gaussian mixture models and polynomial chaos, wherein the use of Gaussian mixture models decreased the order of polynomial necessary to achieve a desired accuracy, thereby mitigating the computational costs of applying polynomial chaos expansions to systems of high dimensionality [85].

2.4 Stochastic Orbit Prediction

Stochastic orbit prediction refers to satellite estimation or prediction methods which incorporate uncertainty within the system's dynamics (sometimes referred to as "process noise"). This is in contrast to the previous section, in which dynamics formulations were deterministic. In stochastic formulations, the system states are random variables and the equations of motion represent a system of stochastic differential equations. As such, any state prediction is an estimate with probabilistic properties.

Of the various sources of dynamic uncertainty present in the prediction of orbits, uncertainty in the density of the upper atmosphere (and thus uncertainty in the perturbing acceleration due to air drag) was noted as a key driver of satellite position uncertainty as early as 1962, by Karrenberg et al. [10]. While air drag is not the only source of dynamical uncertainty for Earth satellites, it is widely regarded as the most influential for those in LEO [92, 94, 98, 99].

Consider again the representation of satellite air drag given in Equation 2, in which all the variables may be uncertain. Uncertainties in the atmospheric density ρ and the ballistic coefficient B^* are correlated, but can be estimated and considered separately as well, as shown by Wright and Woodburn in their development of a real-time sequential estimator and batch smoother which are capable of estimating errors and uncertainty of both atmospheric density and ballistic coefficient simultaneously [98]. Their method used a Jacchia atmosphere [119] with the solar input converted from three-hour step function to a continuous spline. Half-lives for the ρ and B^* Gauss-Markov processes appeared to have been chosen based on earlier work of Akella et al. [15], and the research found that the half-lives of atmospheric density and ballistic coefficient must be considerably different to allow observability and estimation of both simultaneously. Their work also concluded that atmospheric density errors are highly correlated with position estimate errors, while errors in the ballistic coefficient were negligibly correlated with position estimate errors when both types of error were considered simultaneously.

Uncertainty in air drag effects many types of calculations and analyses involving LEO satellites, including collision probability in the realm of conjunction analysis [13, 17] and calculating decay lifetimes [99, 120, 121]. Thus, the development of orbit determination and propagation methods which acknowledge uncertain air drag in their dynamics, estimate relevant uncertain parameters, and output orbit estimates with realistic uncertainty characterizations is of great interest.

Marcos et al. recognized the role of air drag uncertainty and improved orbit determination accuracy by using satellite data to calculate updates to atmospheric models [92]. Nazarenko et al. also applied corrections to atmospheric density using multiple satellites, and implemented a “density tracking process” in parallel with an orbit determination method to improve the orbit determination results [93].

While these efforts estimated the errors of atmospheric models to calculate corrections, Lee and Alfriend examined the effect of employing stochastic versus deterministic atmospheric density models in more detail. By modeling the atmospheric density error as first-order Gauss-Markov random processes, their work investigated the errors introduced by calculating the probability of collision of a secondary object with the International Space Station using a perfect dynamics model versus modeling atmospheric density as uncertain [14]. Their work also utilized MC simulation in the calculation of covariance matrices.

Using similar stochastic representations, Wilkins and Alfriend improved the method of scaling a deterministically computed covariance matrix to achieve better realism by incorporating dynamical uncertainty in the form of first-order Gauss-Markov processes into an Extended Kalman Filter (EKF)-based orbit determination method. Parameters of the Gauss-Markov random processes were tuned manually, and the method used multiple processes with different time-scale parameters. Along with estimating the orbit, the EKF also estimated the overall density perturbation (but not the individual components or parameters of the processes) and the ballistic coefficient. The authors conclude that the use of the EKF with Gauss-Markov process noise results in more realistic covariance growth [16]. Their choice of using a first-order Gauss-Markov process to characterize the atmospheric density uncertainty was informed by prior work by Akella et al., which concluded that atmospheric density perturbations could be modeled by a stationary first-order Gauss-Markov process [15]. Akella et al. chose to model density errors as first-order Gauss-Markov processes for the purposes of "illustration", and noted that other distributions could be used but that drag uncertainty was inherently difficult to parameterize due to its variables' being functions of both position and time.

Other types of stochastic processes have been applied to characterizing uncertainty in atmospheric density, such as the modified Ornstein-Uhlenbeck process employed by Sagnieres and Sharf in their study of the effect of atmospheric model uncertainties on satellite orbit prediction. In their study, Sagnieres and Sharf analyzed three atmospheric models using modified Ornstein-Uhlenbeck random processes to characterize density uncertainty and then numerically solved the resulting stochastic differential equation to analyze the atmospheric uncertainty's effect on orbit prediction. The purpose of their study was concerned more with the orbit itself than the satellite's position within the orbit, and therefore the analysis was focused on the uncertainty's effect on the orbit's parameters, specifically semi-major axis and mean anomaly [6].

McLaughlin et al. also estimated atmospheric density, using Wright and Woodburn's technique [98], in a precise orbit determination method. Using precise orbit data from the Challenging Minisatellite Payload (CHAMP) satellite, the method estimates two different corrections to the modeled atmospheric density (one "consistent" over a long time scale and one "dynamic" which fluctuated on a shorter time scale) and applied the corrections during orbit determination. The method then applied a smoother using all the data which improved accuracy and estimated the ballistic coefficient [94].

McLaughlin et al. also used data from multiple satellites to estimate atmospheric densities, and compared the results to accelerometer-based truth data and found general agreement [95]. Others have employed satellite data to refine our knowledge of the upper atmosphere and improve existing atmospheric models or develop entirely new ones [96, 97]. Many more examples exist of density calibration efforts, however they are not reviewed here as this research is focused on linkages to uncertainty characterizations, and not on improving or analyzing atmospheric models.

Additionally, Anderson et al. used data from the CHAMP satellite to numerically analyze the effects of atmospheric variation on the error of satellite orbit predictions, in an effort to characterize the sensitivity of such predictions to variations in the atmosphere and thus inform future improvements to atmospheric models [100]. Subsequent work by Anderson et al. studied how the time lag between an unexpected atmospheric disturbance and when an atmospheric model reflected the effects of the disturbance (often on the order of 1–4 hours) related to errors in orbit prediction, and found that the time lag caused noticeable errors in orbit predictions [101]. Both works used deterministic dynamics models, but demonstrate that uncertainty in atmospheric properties contribute directly to errors and uncertainty in orbit predictions. Leonard et al. performed a similar type of analysis on the fluctuations of the troposphere and their effect on orbit prediction (again using deterministic dynamics), and found that this type of atmospheric fluctuation causes significant (on the order of 200 meters) satellite prediction errors in the in-track direction [102].

Emmert et al. have made multiple contributions to the aforementioned problem of using stochastic dynamics to improve uncertainty realism. Motivated by reducing false-positives in conjunction analysis, Emmert et al. developed a method of analytically approximating in-track position uncertainty from uncertainty in the relative density error [11]. A more recent work by Emmert et al. developed equations for analytically approximating errors of the mean motion and mean anomaly of a satellite orbit from atmospheric density errors. Their results showed that the in-track prediction variance grows with Δt^3 if the relative density error is a white noise process, and Δt^5 if it is a Brownian motion process [12]. Schiemenz et al. also developed extended least squares estimation algorithms that incorporate the variance relationships developed by Emmert et al. [21]. Another, apparently concurrent effort by Schiemenz et al. developed an analytical method for relating uncertainties in atmospheric model inputs (indexes of solar activity) directly to uncertainty in the relative atmospheric density, independent of the atmospheric model itself (i.e. without another call to the atmospheric model) [20].

The aforementioned work of Rich et al. examined the time-growth of in-track variance using a simplified perturbation theory approach which used the ballistic coefficient B^* as the single random constituent variable of air drag rather than assigning random processes to the density error. Their results showed that in-track position variance grows with Δt^4 using the most recent TLE as a proxy for the true satellite state [9]. Coppola and Tanygin also noted that position uncertainty tends to be greater in the in-track direction, and noted that Cartesian ellipsoids do not model positional uncertainty well [107].

The impact of air drag uncertainty on conjunction analysis (specifically probability of collision calculation) was studied by Bussy-Virat et al. using the Spacecraft Orbital Characterization Kit (SpOCK) [17]. SpOCK is a full-featured mission design tool which is capable of propagating satellite orbits with uncertainty in the satellite state and attitude, atmospheric density, and ballistic coefficient. In the presence of uncertain dynamics (i.e. non-zero uncertainty for atmospheric density or ballistic coefficient), SpOCK uses Monte Carlo methods to propagate an ensemble of trajectories and thus compute a realistic uncertainty along with the state estimates [18]. The conjunction analysis study used Monte Carlo methods and uncertainty in the atmospheric model input parameters and resulted in accurate conjunction calculations in approximately 1 hour "using 200 cores". The authors also note that the DoD recently (circa 2018) began considering atmospheric density errors in conjunction analyses through use of a "consider-parameter" [17]. Consider parameters were developed by Markley et al. in their presentation of batch and sequential methods capable of dealing with many forms of uncertainty (including uncertain dynamics), by splitting the system state vector space into "solve-for" (elements which are to be estimated by the methods) and "consider" (elements which are not to be estimated but are considered to be uncertain, and therefore impact the resulting uncertainty calculations) parameters [103, 104]. Another conjunction analysis which considered drag uncertainty was performed by Hejduk and Snow, and focused solely on re-processing “serious conjunction events” to determine if the consideration of uncertainty in air drag resulted in changing the severity category of the conjunction. They found that in many cases the inclusion of uncertain drag effects upgraded the severity of possible conjunctions [13].

A final example of an implementation which incorporates uncertainty in the satellite dynamics is the Covariance Realism Tool (CRT) in use for maneuver planning of the NASA GPM satellite (mentioned above in Section 2.3.1), which adds dynamical process noise in the form of linear additive white Gaussian noise to the propagation of state estimate uncertainty. The tool does not attempt to characterize the parameters of the added noise, but requires “tuning” by the operator to ensure the covariance growth of the prediction coincides statistically with previous characterizations [91].

2.5 Coordinate Frames

In any effort to estimate the future state of a satellite and characterize that estimate’s uncertainty, the choice of coordinate frame has a significant impact on the underlying probability distributions. Critically, the linearity of the system (and therefore the Gaussian nature of any errors and uncertainty) is preserved better in some coordinate frames than in others.

For example, the two-body problem dynamics are linear in the equinoctial elements, and thus propagation of an initially Gaussian uncertainty remains Gaussian [105]. Contrarily, the dynamics are not linear when resolved in Cartesian coordinates, and propagation of an initially Gaussian uncertainty quickly becomes non-Gaussian because linear approximations are valid only near the reference point. This concept extends to perturbed dynamics which are still dominated by two-body dynamics, in that dynamics resolved in equinoctial elements are nearly linear and propagated uncertainty remains Gaussian longer than if resolved in Cartesian coordinates [63, 105]. Polar coordinates represent another option for leveraging linear dynamics and Gaussian uncertainty characteristics [9], as initial Gaussian uncertainty remains Gaussian when propagated using polar coordinates for two-body circular orbits [63], however this breaks down for eccentric orbits as non-linearities appear [62, 106].

Equinoctial element formulations, while offering the advantage of increased linearity versus cartesian coordinates, suffer from a co-mingling of position and velocity information which makes visualizing position uncertainty difficult [107]. This, coupled with polar coordinates only preserving linearity for circular orbits, motivates the use of "curvilinear" coordinates which preserve linearity and Gaussian characteristics well for eccentric orbits [106–109].

Multiple researchers have concluded that equinoctial elements and curvilinear coordinates preserve linearity and Gaussian characteristics better than Cartesian representations [63, 106–108]. Methods have also been developed to transform uncertainty characterizations from polar to Cartesian [63] and Cartesian to curvilinear [107], and also for analyzing proximity operations in curvilinear coordinates [110].

2.6 Review of Widely Available Estimators

Within the realm of orbit prediction there a several widely available software packages, both commercial and open-source. Of these, the most widely used seem to be Analytical Graphics Inc.'s Systems Took Kit (STK), FreeFlyer by a.i. solutions, NASA's General Mission Analysis Toolkit (GMAT), and the open-source Java Astrodynamics Toolkit (JAT).

Of these products, only STK is capable of considering stochastic air drag. This consideration takes the form of treating the ballistic coefficient as a consider parameter within STK's high-precision orbit propagator (HPOP) [122].

The other three products use only deterministic dynamics. GMAT accepts standard deviation values in solar input data files, but this appears to be for file interpretation purposes as the drag calculation is entirely deterministic [123]. FreeFlyer offers a variety of atmospheric models, but calculates all dynamics deterministically [124], and JAT uses only deterministic dynamics as well [125].

2.7 Summary

This chapter has presented a review of previous research related to satellite orbit prediction (both deterministic and stochastic), the generation and propagation of model uncertainty, coordinate frames and their relationship to satellite dynamics, and current widely used satellite estimators.

III. Preliminaries

Chapters IV–VI below share some or all of the same prediction models, observational data sources, analysis scenarios, and coordinate frame considerations. This chapter details these preliminary topics for clarity.

3.1 Prediction Models

3.1.1 Models

The literature review of Chapter II noted that satellite orbit prediction models can be generally divided into two groups: analytical methods or "general perturbations" and numerical methods or "special perturbations". The research detailed in the following chapters uses both.

The analytical model used is SGP4, in two implementations. The first implementation was obtained via Vallado et al. [32] and is referred to henceforth as "SGP4 A". This implementation is believed by Vallado et al. to be close to the version in use by CFSCC, which was obtained from CFSCC's public website [30] in compiled library form and is referred to henceforth as "SGP4 B". TLEs were also obtained for all relevant satellites from CFSCC's public catalog [126] for use with these two prediction models.

The SP methods used refer to numerical integration of the satellite system's dynamical equations of motion. These numerical equations of motion are formulated identically for the two models, and are derived such that they are of the form

$$\frac{d\boldsymbol{X}}{dt} = \dot{\boldsymbol{X}} = \boldsymbol{f}(\boldsymbol{X}, t) \tag{3}$$

where $\boldsymbol{X}$ is the system state vector. Let this state vector be composed of the satellite's Cartesian position $\boldsymbol{r} = \{x, y, z\}$ and velocity $\boldsymbol{v} = \{v_x, v_y, v_z\}$ in an Earth-centered inertial reference frame, along with the ballistic coefficient B^* as in Equation 4. The ballistic coefficient is appended to the state vector so that it may be estimated from observational data along with position and velocity. This is necessary even though a constant B^* could be approximated from satellite properties because estimating B^* from observational data allows B^* to act as a catch-all for modeling errors and discrepancies, following from the hypothesis that letting B^* be the single random variable in the air drag equation (Equation 2) can capture the model's overall prediction uncertainty (Research Hypothesis 3).

$$\boldsymbol{X} = \left\{x, y, z, v_x, v_y, v_z, B^*\right\}^T \tag{4}$$

The equations of motion are formed using Hamiltonian coordinates $\boldsymbol{q} = (x, y, z)^T$ and momenta (which per unit mass are simply velocities) $\boldsymbol{p} = (v_x, v_y, v_z)^T$. For an Earth satellite affected only by the Earth's gravity in an inertial reference frame, the Hamiltonian ($\mathcal{H}$) per unit satellite mass is

$$\mathcal{H} = \frac{1}{2}\left(v_x^2 + v_y^2 + v_z^2\right) + V \tag{5}$$

where V is the Earth's geopotential function. Then the equations of motion in

Equation 6 are obtained from Hamilton's canonical equations.

$$\dot{\boldsymbol{X}} = \boldsymbol{f}(\boldsymbol{X}, t) = \begin{bmatrix} \frac{\partial \mathcal{H}}{\partial v_x} \\ \frac{\partial \mathcal{H}}{\partial v_y} \\ \frac{\partial \mathcal{H}}{\partial v_z} \\ -\frac{\partial \mathcal{H}}{\partial x} \\ -\frac{\partial \mathcal{H}}{\partial y} \\ -\frac{\partial \mathcal{H}}{\partial z} \\ 0 \end{bmatrix} = \begin{bmatrix} v_x \\ v_y \\ v_z \\ -\frac{\partial V}{\partial x} \\ -\frac{\partial V}{\partial y} \\ -\frac{\partial V}{\partial z} \\ 0 \end{bmatrix} \tag{6}$$

Note that B^* and its associated equation of motion $\dot{B}^* = 0$ have been appended to the state vector and the equations of motion. In a deterministic sense (and when satellite attitude is not considered, as it is not in this case), letting $\dot{B}^* = 0$ is the best *predictive* statement about the dynamics of B^* that can be made. This is the case for the analysis in Chapter IV, however the analysis of B^* as a random process in Chapter V will lead to this formulation morphing into a stochastic one in Chapter VI. Also note that augmenting the state vector with B^* allows initial conditions that include B^* to be estimated for each prediction by applying non-linear least squares to a subset of data preceding each prediction's initial time, but also has the effect of grouping additional modeling errors into the B^* estimates as mentioned above.

The Earth's aspherical geopotential V is implemented using the common spherical harmonics model given by Equation 7

$$V = -\frac{\mu}{r} \sum_{n=0}^{\infty} \sum_{m=0}^{n} \left(\frac{r}{R_{\oplus}} \right)^{-n} P_n^m \sin(\delta) \big(C_{nm} \cos(m\lambda) + S_{nm} \sin(m\lambda) \big) \tag{7}$$

where μ is the gravitational parameter, $R_{\oplus}$ is the equatorial radius of the Earth,

P_n^m are the associated Legendre polynomials, C_{nm} and S_{nm} are gravitational model coefficients, n and m are the degree and order of the gravity model, $r = \sqrt{x^2 + y^2 + z^2}$ is the magnitude of the satellite's position vector, δ is the satellite's geocentric latitude, and λ is the satellite's longitude [52]. The geopotential model coefficients C_{nm} and S_{nm} are provided by the gravity models described below.

The partial derivatives of the geopotential with respect to the Cartesian x, y, and z coordinates in Equation 6 are not carried out directly. Rather, the satellite's position vector is converted to an Earth-fixed reference frame and the first and second derivatives of the geopotential are carried out using a modified version (to enable normalized calculation of the second partial derivatives) of Pines' algorithm as provided by Eckman et al. [127, 128]. The resulting acceleration vector and matrix of second partials is then converted back to the inertial reference frame for use in the predictions. Derivations of the partial derivatives of V are widely available (for example in Vallado [5, pgs. 549–550]) and are not reproduced here.

The effects of air drag are then applied to equations of motion simply by adding the components of the air drag acceleration given by Equation 2, resulting in the equations of motion in Equation 8.

$$\dot{\boldsymbol{X}} = \boldsymbol{f}(\boldsymbol{X}, t) = \begin{bmatrix} v_x \\ v_y \\ v_z \\ -\frac{\partial V}{\partial x} + a_{D,x} \\ -\frac{\partial V}{\partial y} + a_{D,y} \\ -\frac{\partial V}{\partial z} + a_{D,z} \\ 0 \end{bmatrix} \tag{8}$$

The velocity of the spacecraft relative to the Earth's atmosphere (v_{rel} in Equation 2) is calculated by assuming that the atmosphere rotates with the Earth via Equation 9, where $\omega_{\oplus}$ is the rotation rate of the Earth in radians per second.

$$v_{\text{rel}} = \begin{bmatrix} v_x + \omega_{\oplus} y \\ v_y - \omega_{\oplus} x \\ v_z \end{bmatrix} \tag{9}$$

Both SP models are formulated per the preceding development. The difference between the two SP models is the coefficients used within the gravity expansion (referred to as "gravity models") and the atmospheric models used to obtain the density in the air drag acceleration. The first SP model, termed "SP A", uses the EGM96 gravity model [129] and a relatively simple atmosphere model from Regan and Anandakrishnan [130]. This atmosphere model requires no input other that the satellite's position. The second SP model, termed "SP B", uses the more up to date EGM2008 gravity model [131] and NRLMSISE-00 atmospheric model [132]. The NRLMSISE-00 atmospheric model is more robust than that of Regan and Anandakrishnan, and requires several types of input data along with the satellite's position, including two varieties of the solar flux and various geomagnetic activity indices (see Section 3.2 for information regarding data sources).

In addition to the equations of motion used for numerical integration, the differential state transition matrix $\Phi(t, t_0)$ is required for the SP models for use in non-linear least squares estimation of system states (both for initial conditions and for estimating B^* time series). $\Phi(t, t_0)$ is obtained by calculating the first-order linearization matrix A and numerically integrating according to

$$A(t) = \left.\frac{\partial f}{\partial \boldsymbol{X}}\right|_{\boldsymbol{X}(t)} \tag{10}$$

$$\dot{\Phi}(t, t_0) = A(t)\Phi(t, t_0) \tag{11}$$

where $\Phi(t_0, t_0) = I$ and I is the identity matrix. Details on calculating the A matrix are given in Appendix A and an overview of the non-linear least squares algorithm used is given in Appendix B.

Numerical integration of Equations 8 and 11 was accomplished with the Adams-Bashforth-Moulton (ABM) numerical integrator. The ABM integrator is a variable-step-size, variable order (up to order 12) predictor corrector method [133] which accepts desired relative and absolute error values as inputs and adapts its step size to maintain those error thresholds. The ABM integrator is also the basis of MATLAB's "`ode113`" numerical integrator [134], which is said to be very suitable for orbital dynamics work [135]. Source code for the ABM integrator in the C++ language was obtained from the website of Florida State University [136] and modified for use in special perturbations by the author.

3.1.2 Parameter Sensitivity

While the SGP4 models needed no input parameters aside from pre-formatted CFSCC TLEs, the SP models have many tunable parameters that alter their performance. The values for these parameters used generally throughout this research are tabulated in Table 1, where σ_r and σ_v are the standard deviations of the input position and velocity observational data used in least squares estimation and N_{LS} is the number of data points used for each least squares estimation, unless otherwise specified.

Table 1. Special Perturbations Prediction Model Parameters

Parameter	Value
Geopotential Order	25
Geopotential Degree	25
Absolute Integration Tolerance	1×10^{-9}
Relative Integration Tolerance	1×10^{-9}
σ_r (CHAMP, GRACE A/B)	$5\,\mathrm{cm}$
σ_v (CHAMP, GRACE A/B)	$5\,\mathrm{cm\,s^{-1}}$
σ_r (SOS)	$1\,\mathrm{m}$
σ_v (SOS)	$1\,\mathrm{mm\,s^{-1}}$
N_{LS}	540

The performance of the SP models is sensitive to these parameters. The two most impactful parameters are the order and degree of the geopotential model and the number of data points used as input to the least squares estimation of initial conditions (N_{LS}). Results of a sensitivity analysis performed by executing 3-day Monte Carlo simulations for various values of N_{LS} and the degree/order of the geopotential are tabulated in Tables 2 and 3 and visualized in Figure 1.

Table 2. Sensitivity of Special Perturbations Models to Degree and Order of Geopotential ($N_{\mathrm{LS}} = 720$)

Geopotential Order & Degree	Average Position Error (km)	Computation Time (min)
10	21.8	1.48
15	17.8	2.16
20	10.3	2.47
25	8.88	3.58
30	8.83	4.38
35	8.30	5.22

In general, the effect of N_{LS} on the SP models is to increase model prediction accuracy as N_{LS} increases, and increasing the degree and order of the geopotential also had the effect of improving model accuracy (though the accuracy improvement decreases noticeably after the order and geopotential reach about 25). The

Table 3. Sensitivity of SP Models to N_{LS} (Geopotential Degree/Order of 25)

N_{LS}	Average Position Error (km)	Computation Time (min)
360	20.4	2.11
540	12.5	2.73
720	8.88	3.50
900	7.58	4.15
1080	6.90	4.66

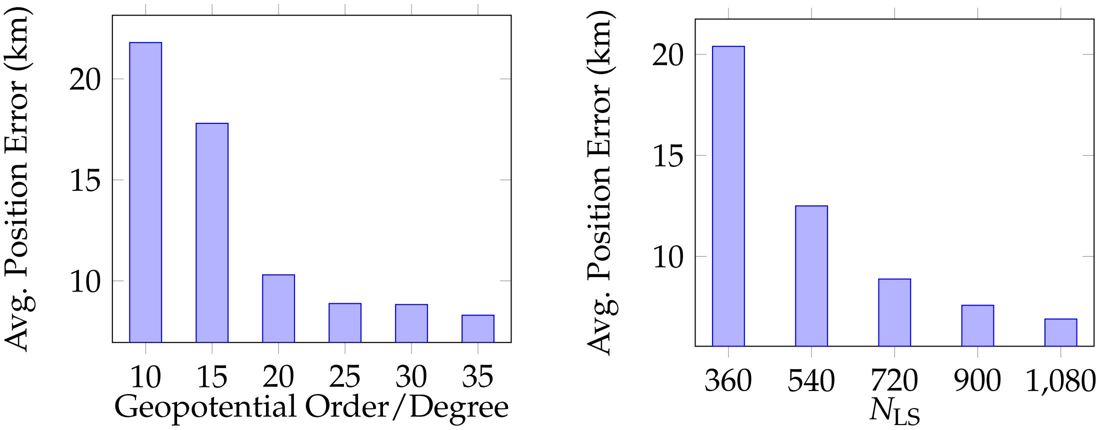

Figure 1. Sensitivity of Special Perturbations Models to Degree and Order of Geopotential and Number of Data Points Used for Least Squares Estimation

trade-off for increased accuracy is computation time, however. Therefore, the values of 540 for N_{LS} and 25 for the degree and order of the geopotential were chosen for this research as a balance between model fidelity and computation time. Recall also that this research is concerned with the uncertainty realism of the models, not necessarily their accuracy when compared to truth data, so long as they're of a representatively useful fidelity. Similar reasoning informed the choice of 1×10^{-9} for the integration tolerances, while σ_r and σ_v were chosen to best match the quoted or assumed accuracy of the respective observational data (see Section 3.2).

Finally, it is not surprising that altering the various input parameters changes the performance of the SP models. Changing any significant parameters (the order of the geopotential model, for example) should affect model performance—what's important is that the models are self-consistent for similar parameters, which is why the analyses in Chapters IV–VI use the common parameterization given by Table 1 (unless otherwise noted) and common scenarios given in Tables 6 and 7 (analysis scenarios are discussed in greater detail below). After all, this research is an examination of *modeling* uncertainty—different models will exhibit different performance characteristics, and the aim here is to have the SP models reflect accurate characterizations of their own modeling uncertainty, which is certainly tied to the parameters inherent within the models.

3.2 Data Sources

Two types of observational satellite data were needed for the research activities described in Chapters IV–VI, namely TLEs and vector position and velocity data. Data of these types was acquired for four different LEO satellites to facilitate the various analyses: Challenging Minisatellite Payload (CHAMP), Gravity Recovery and Climate Experiment (GRACE)-A/B, and the Air Force Institute of Technology Center of Space Research and Assurance's Space Object Self-Tracker (SOS) payload.

CHAMP was a German satellite that operated from 2000-2010 fulfilling various science missions related to Earth's gravity field, magnetic field, and ionosphere [137]. CHAMP's orbit was nearly circular (eccentricity $\approx$ 0.004) and nearly polar (inclination $\approx$ 87 deg), with an altitude between 300 km and 450 km [138]. An artist's impression of the CHAMP satellite is shown in Figure 2.

The GRACE mission consisted of an identical pair of satellites (A/B) and was a joint US/German mission that operated from 2004-2017, making detailed observations of Earth's gravity field from an approximate altitude of 500 km [140]. The pair of GRACE orbits were also nearly circular (eccentricity $\approx$ 0.001) and nearly polar

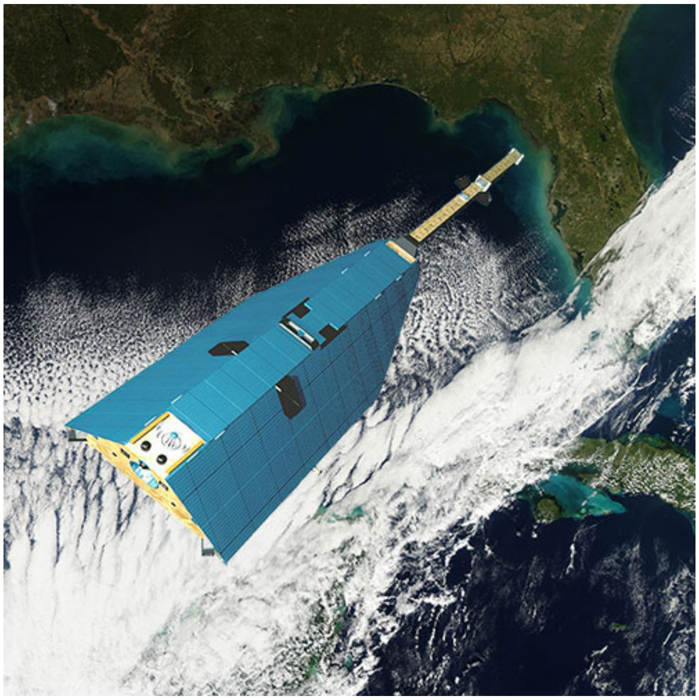

Figure 2. Artist's Impression of the CHAMP Satellite [139]

(inclination $\approx$ 89 deg) [141]. Note that because the pair of GRACE satellites orbited in formation, they experienced nearly the same dynamical forces and therefore results for GRACE-A and GRACE-B throughout this research should compare very closely to each other. An artist's impression of the GRACE satellites is shown in Figure 3.

The SOS payload was hosted onboard NASA's Green Propellant Infusion Mission (GPIM) satellite which launched into a circular low Earth orbit in June 2019 at an inclination of 24 deg and altitude of approximately 720 km [143]. An artist's impression of the GPIM satellite is shown in Figure 4.

Observe in Figures 2–4 that the CHAMP, GRACE, and GPIM satellites are shaped differently. Specifically, the GPIM satellite has solar arrays which extend outward from the main body while CHAMP and GRACE-A/B do not. With respect to how these differences might influence the effects of atmospheric drag, recall that the shape and orientation of a satellite is accounted for by the ballistic

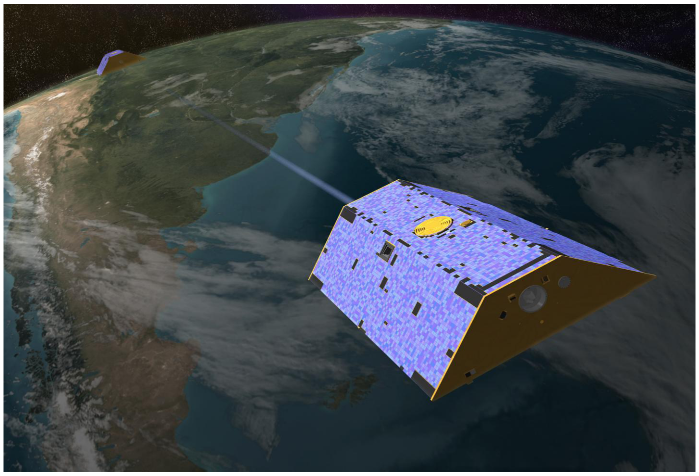

Figure 3. Artist's Impression of the GRACE-A/B Satellites [142]

coefficient B^* in Equation 2. Therefore, such differences did not affect prediction performance or uncertainty realism for the purposes of this research because B^* was estimated from observational data, however a larger area to mass ratio (if the solar arrays of GPIM were oriented perpendicular to the satellite's direction of travel, for example) may be expected to increase the uncertainty of a satellite prediction. This effect was not distinguishable in this research, however, as the positional accuracy of the SOS data is lower than that for CHAMP and GRACE-A/B and therefore effects of the area to mass ratio could not be observed.

TLEs were obtained for all four of these satellites from CFSCC's public catalog [126]. Catalog numbers for each satellite are listed in Table 4. The TLEs were used as initial conditions for the satellite predictions conducted using both SGP4 propagators as detailed in Chapter IV.

Table 4. CFSCC Catalog Numbers for Analyzed Satellites

Satellite	TLE Catalog Number
CHAMP	26405
GRACE-A	27391
GRACE-B	27392
GPIM (SOS)	44342

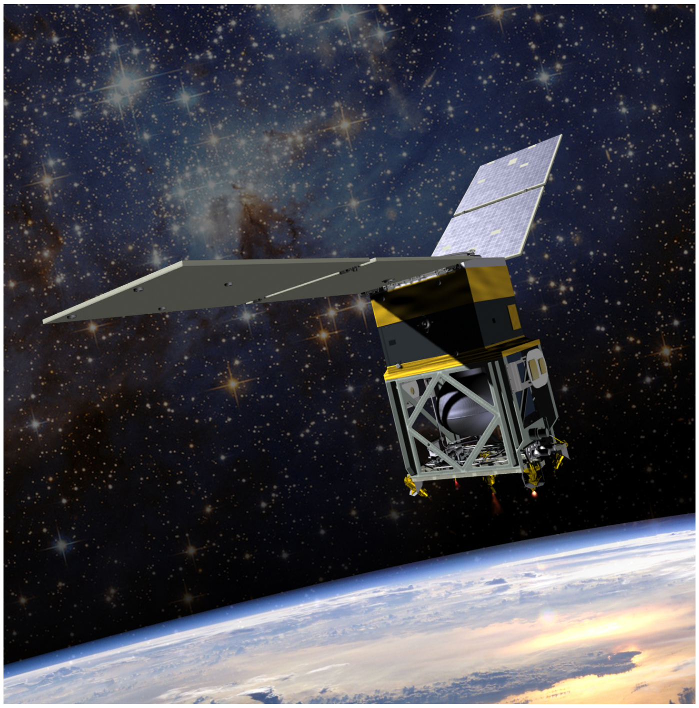

Figure 4. Artist's Impression of the GPIM Satellite [144]

The vector data for CHAMP, GRACE-A, and GRACE-B consists of the following at 30 second intervals: time in Terrestrial Time, post-processed position and velocity state vectors resolved in the Conventional Terrestrial System reference frame (an Earth-centered, Earth-fixed (ECEF) rotating frame), attitude angles (roll, pitch, and yaw), a maneuver flag to identify if a data element was effected by a maneuver, and other science mission data flags [145]. The position vectors are claimed to be accurate to approximately 5 cm [146]. This data was downloaded from GeoForschungsZentrum Potsdam's Information System and Data Center for CHAMP from 2000-2010 and for GRACE-A/B from 2004-2017 [147].

The vector data for SOS consists of position and velocity information from the on-board GPS receiver. Time codes are in GPS weeks and GPS seconds, and position and velocity data are in an ECEF reference frame. Positional data is provided with significant digits to 1 m, and velocity data contains significant digits to $1\,\mathrm{mm\,s^{-1}}$.

Unfortunately, the SOS data is not nearly as regular as that for CHAMP and GRACE-A/B, and has gaps of various time lengths throughout. Figure 5 demonstrates the prevalence of gaps within the SOS data, however the visualization is incomplete as shorter data gaps are not visible due to resolution limitations. Table 5 therefore lists all time spans of greater than four days within the available SOS data for which the maximum data gap was less than 900 seconds, of which there are four. The longest of these is just over six days in length and was used for the SOS analysis presented in this research. Four days was used as the minimum acceptable length of a data interval because the propagation time ΔT used throughout this research is three days, and some leading data must be available to permit estimation of initial conditions via non-linear least squares. Also, choosing 900 seconds as the maximum allowable data gap was a subjective selection and increasing this value may make additional data intervals available, however the number of intervals doesn't improve drastically (increasing the allowable data gap to 2 hours yields 7 good data intervals of at least 4 days, and none longer than 7 days) and 900 seconds already represents approximately 1/6 of an orbit period for SOS. The concern associated with increasing the size of the allowable data gap too much is that estimating the initial conditions and B^* time series as discussed in later chapters may become unreliable or infeasible. For example, estimates of B^* time-series in Chapters V and VI have a sample rate of one estimate every 10 minutes. Finally, note that the lack of available data for SOS precluded its inclusion in the empirical covariance analysis of Chapter IV, as there simply isn't enough consecutive data to permit the sampling of enough propagations to justify the use of the expectation operator in the covariance calculation of Equation 30.

For the stochastic prediction analysis of Chapter VI, the SOS data is used in its unaltered form when being used as observational data and in a smoothed form

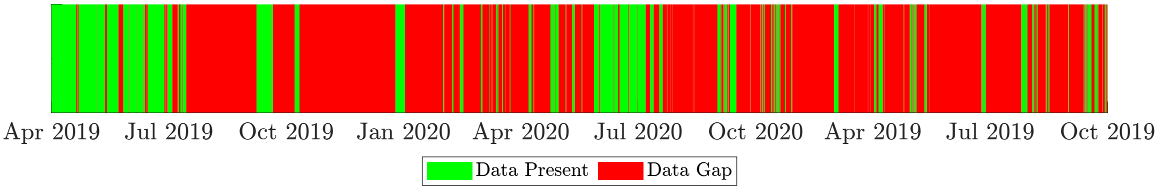

Figure 5. SOS Data Gap Visualization, $\leq 900\,\mathrm{s}$ Gap Permitted

Table 5. Available Intervals of SOS Data, $\leq 900\,\mathrm{s}$ Gaps Permitted

Interval Start (UTC)	Interval End (UTC)	Interval Length (d)
29-Jun-2019 21:32:58	04-Jul-2019 09:13:18	4.5
15-Jul-2019 15:59:10	19-Jul-2019 19:34:30	4.1
30-Jul-2019 16:46:59	05-Aug-2019 17:54:22	6.0
08-Sep-2019 15:59:24	13-Sep-2019 12:06:59	4.8

when being used as “truth” data. This smoothed “truth” data was obtained by performing rolling least squares estimates at evenly spaced (30 seconds to match the frequency of CHAMP and GRACE-A/B data) output points.

3.3 Propagation Scenarios

The analyses that constitute this research were performed using the aforementioned satellites at times selected from periods of high solar activity and periods of low solar activity (one of each for each satellite, except for SOS for which data is only available during times of low solar activity). “Low” and “high” solar activity refer to the solar flux incident upon the Earth at the 10.7 cm wavelength, commonly referred to as the F10.7 solar flux. This measurement is also used as input to many atmospheric models, including the NRLMSISE-00 model used in SP B. Solar flux data was obtained from a website maintained by the University of Colorado [148].

Two versions of each propagation scenario were used, a “long” version and a “short” version. The long versions were necessary for the empirical covariance analyses described in Chapter IV to permit the use of enough TLEs to justify the calculation of covariance matrices using the expectation operator. These long versions used six months of input data. The short versions were used for the analyses described in Chapters V and VI (including the empirical results presented in the latter). These consist of one month of input data, and were used to better represent a more realistic operational timescale and to ensure the applicability of the stationarity property of the B^* random processes described in Chapter V.

Figure 6 shows the observed F10.7 solar flux as well as the time periods used in this research, and Tables 6 and 7 list the details of each prediction scenario as used throughout this research. Note the data shown in Figure 6 has been smoothed by applying a 14-day moving average for the purposes of this visualization only (data used in the SP models was not smoothed). Also note that the "Date Range" columns in Tables 6 and 7 refers to the data window for random sampling of empirical covariance analysis propagations, while the "Date/Time" column in Table 7 refers to the initial time used for single stochastic predictions.

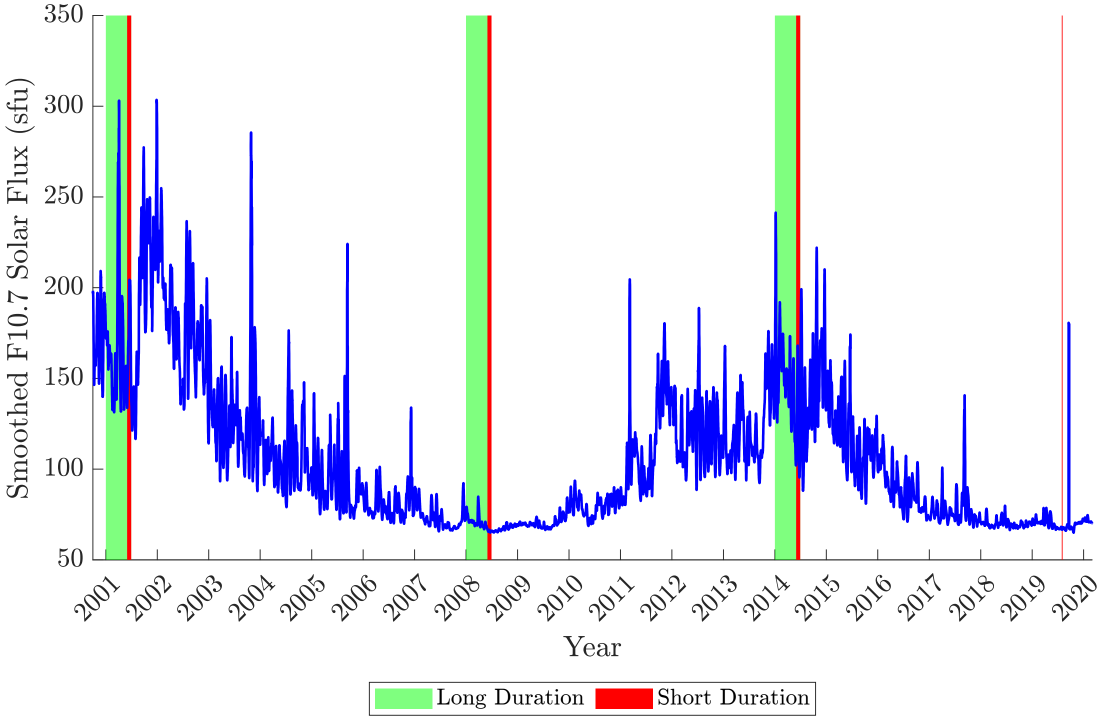

Figure 6. Smoothed Observed F10.7 Solar Flux with Scenario Regions Highlighted

Table 6. Details of Research Scenarios, Long Versions

Satellite	Solar Level	Year	Date Range	Average F10.7 (sfu)
CHAMP	Low	2008	1 Jan–30 Jun	70.4
CHAMP	High	2001	1 Jan–30 Jun	168.0
GRACE-A/B	Low	2008	1 Jan–30 Jun	70.4
GRACE-A/B	High	2014	1 Jan–30 Jun	146.4

Table 7. Details of Research Scenarios, Short Versions

Satellite	Solar Level	Year	Date Range	Average F10.7 (sfu)	Date/Time (UTC)	Daily F10.7 (sfu)
CHAMP	Low	2008	1–30 Jun	65.9	Jun 8, 10:00	64.9
CHAMP	High	2001	1–30 Jun	174.1	Jun 8, 10:00	178.7
GRACE-A/B	Low	2008	1–30 Jun	65.9	Jun 8, 10:00	64.9
GRACE-A/B	High	2014	1–30 Jun	122.4	Jun 8, 10:00	148.8
SOS	Low	2019	30 Jul–5 Aug	67.0	Aug 1, 20:00	67.2

Finally, geomagnetic activity indices are optional inputs to the NRLMSISE-00 atmospheric model which were used in SP B. Geomagnetic index data was obtained from GeoForschungsZentrum Potsdam's Information System and Data Center [149].

3.4 Coordinate Frames

The research described in the subsequent chapters involves the calculation of ensembles of prediction error vectors for each of the scenarios described in Tables 6 and 7. As mentioned in Section 2.5, the choice of coordinate frame that such error vectors are resolved in has a significant impact on their probabilistic distribution, specifically with respect to what degree the resulting ensembles resemble Gaussian random variables. Covariance matrices are used throughout this research to represent the uncertainty of the various model predictions, which implies a Gaussian assumption such that the mean of the ensemble and the covariance matrix completely describe the distribution. The validity of this assumption depends greatly on the choice of coordinate frame and on the propagation time of the prediction as the non-linear system dynamics tend to make the ensembles less Gaussian as propagation time increases (as Section 2.5 mentions). The use of a radial, transverse, normal (RTN) coordinate frame, centered on the satellite, for resolving error vectors is described later in this section, and had the benefit of maintaining "Gaussian-ness" much longer than the Cartesian coordinate frames used within the SP prediction models [63]. Additionally, a three-day propagation time was used for the predictions throughout this research and resultant error vector ensembles remained nearly Gaussian (this will be discussed in more detail in later chapters).

Another consideration regarding coordinate frames is that, as Chapter I introduces, the effects of air drag on prediction uncertainty manifest mainly along a satellite's orbit track. This is very difficult to visualize if covariance matrices are resolved in Cartesian coordinates [9, 89], but becomes very apparent if RTN coordinates are used. This is demonstrated in Figure 7, which shows an example prediction covariance matrix as it develops with propagation time Δt in both Cartesian and RTN coordinates, where P_{22} is the in-track element of the RTN covariance matrix.

The RTN coordinate frame is constructed given a Cartesian satellite state vector consisting of position and velocity by letting the radial direction be coincident with the satellite's position vector, the normal direction be perpendicular to the orbit plane defined by the satellite's position and velocity vectors, and the transverse direction as the normal direction crossed with the radial. The creation of the unit vectors of the RTN frame and conversion of position and velocity vectors from

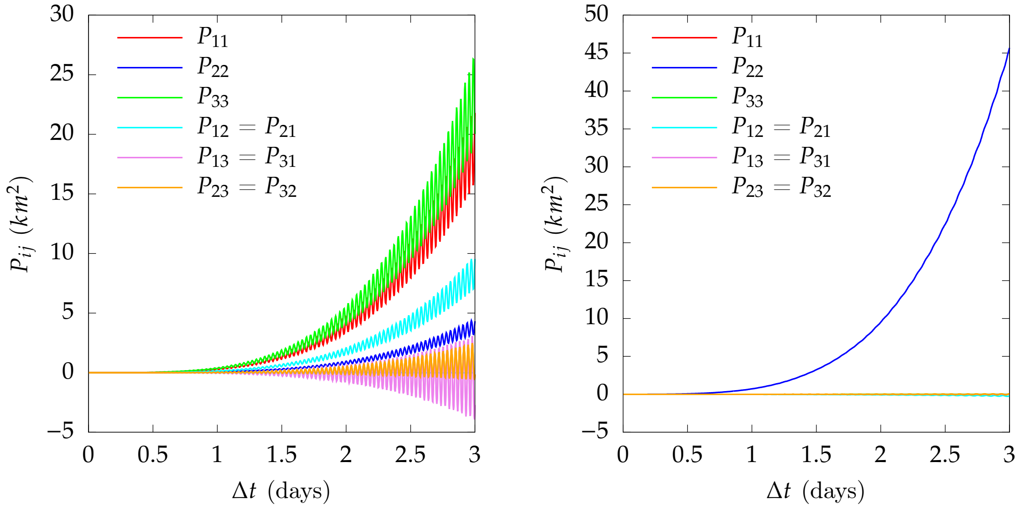

(a) Cartesian (b) RTN

Figure 7. Empirical Covariance Matrix Elements in Cartesian and RTN Coordinate Frames, CHAMP High Solar

Cartesian to RTN coordinates is detailed in Equations 12–17

$$\hat{\boldsymbol{R}} = \frac{\boldsymbol{r}_{\text{xyz}}}{||\boldsymbol{r}_{\text{xyz}}||} \tag{12}$$

$$\hat{\boldsymbol{N}} = \frac{\boldsymbol{r}_{\text{xyz}} \times \boldsymbol{v}_{\text{xyz}}}{||\boldsymbol{r}_{\text{xyz}} \times \boldsymbol{v}_{\text{xyz}}||} \tag{13}$$

$$\hat{\boldsymbol{T}} = \hat{\boldsymbol{N}} \times \hat{\boldsymbol{R}} \tag{14}$$

$$C = \left[\hat{\boldsymbol{R}} \mid \hat{\boldsymbol{T}} \mid \hat{\boldsymbol{N}} \right] \tag{15}$$

$$\boldsymbol{r}_{\text{xyz}} = C\,\boldsymbol{r}_{\text{RTN}} \qquad \boldsymbol{v}_{\text{xyz}} = C\,\boldsymbol{v}_{\text{RTN}} \tag{16}$$

$$\boldsymbol{r}_{\text{RTN}} = C^T\,\boldsymbol{r}_{\text{xyz}} \qquad \boldsymbol{v}_{\text{RTN}} = C^T\,\boldsymbol{v}_{\text{xyz}} \tag{17}$$

where $\boldsymbol{r}$ and $\boldsymbol{v}$ are the satellite's position and velocity vectors in the indicated coordinates, $\hat{\boldsymbol{R}}$, $\hat{\boldsymbol{T}}$, and $\hat{\boldsymbol{N}}$ are the unit vectors describing the RTN frame, and C is a rotation matrix formed from those unit vectors. Note that $C^{-1} = C^T$ because C is orthonormal.

Note that the "transverse" direction in RTN coordinates corresponds to the in-track direction for perfectly circular orbits, and is a close approximation to the in-track direction for very low eccentricity orbits such as those of CHAMP, GRACE-A/B, and SOS. Therefore, the remainder of this document refers to the transverse element in RTN coordinates as the "in-track" direction, utilizing this approximation. This is akin to assuming circular orbits and using polar coordinates as advocated by Rich et al. [9].

Additionally, and distinctly from the preceding conversation regarding coordinate frames, the various prediction models and data sources do not use the same reference frames or time systems. For example, the source data for CHAMP and GRACE-A/B is in terrestrial time and an ECEF reference frame, the source data for SOS is in GPS weeks and seconds and an ECEF reference frame, the output of SGP4 prediction models is in Universal Time Coordinated (UTC) time and a true equator, mean equinox Earth-centered inertial reference frame, and the SP prediction models utilize the J2000 Earth-centered inertial frame and barycentric dynamical time. The SP models were constructed in this way because inertial Cartesian coordinates are native to the equations of motion in Equation 8 and barycentric dynamical time is the standard time used by NASA's "SPICE" toolkit. SPICE is a publicly available set of astrodynamics programming libraries created by NASA's Navigation and Ancillary Information Facility [150, 151], and is used throughout the code underlying this research to handle conversions between various reference frames and time systems. Data displayed in figures and tables throughout this document are labeled with the associated time or reference system, unless they represent differences between quantities wherein only physical units are required.

IV. Effect of Air Drag on Model Prediction Uncertainty

It was asserted in Chapter I that the acceleration caused by air drag has the effect of increasing in-track prediction uncertainty for LEO satellites, that this effect is the predominant cause of model prediction uncertainty for LEO satellites, and that this can be confirmed via analysis of prediction covariance matrices calculated from empirical data.

This chapter details the methodology, results, and conclusions of an empirical covariance analysis, in which ensembles of prediction error vectors are calculated for the various prediction models described in Section 3.1 to facilitate the calculation of prediction error covariance matrices as functions of propagation time Δt. This analysis, described below, corresponds to Research Task 1.

4.1 Methodology

4.1.1 Theoretical Expectations

Beyond expecting that air drag increases model prediction uncertainty in the in-track direction, prior research suggests several growth rates that might be expected for the in-track prediction variance under the influence of air drag. Specifically, the work of Rich et al. suggests in-track variance grows with Δt^4 [9], while Emmert et al. suggest either Δt^3 or Δt^5 depending on the random process assigned to the atmospheric density error [12]. Understanding the expected behavior of the in-track variance for the prediction models to be tested in this research is helpful with regard to interpreting the results and the effect of air drag, therefore the expectations given by these two prior research efforts are explored below.

$$\boldsymbol{a}_D = -B^* \rho \boldsymbol{v}_{\mathrm{rel}} v_{\mathrm{rel}} \tag{2}$$

Beginning with Rich et al. [9] and adapting their development slightly by omitting the reference air density to correspond to Equation 2 (restated above), consider a basic dynamics model for a LEO satellite that begins with a time-derivative of the mean motion $n = n(t) = \sqrt{\mu/a^2}$

$$\ddot{M} = \dot{n} = -\tfrac{3}{2}\sqrt{\mu}a^{-\frac{5}{2}}\dot{a} \tag{18}$$

where $M = M(t)$ is the mean anomaly, μ is the Earth's gravitational parameter, and $a = a(t)$ is the semi-major axis. Similarly, taking a time-derivative of the relation for the semi-major axis and the specific energy $\mathcal{E} = \mathcal{E}(t)$ in Equation 19 gives Equation 20.

$$\begin{aligned} a &= -\frac{\mu}{2\mathcal{E}} \qquad (19)\\ \frac{d}{dt}a &= \frac{d}{dt}\left(-\frac{\mu}{2}\frac{1}{\mathcal{E}}\right) = \frac{\mu}{2}\frac{\dot{\mathcal{E}}}{\mathcal{E}^2}\\ \dot{a} &= \frac{2a^2}{\mu}\dot{\mathcal{E}} \qquad (20)\end{aligned}$$

If air drag is assumed to be the only non-conservative force acting on the satellite, then the orbit's specific energy $\mathcal{E}$ must be equal to the work rate of air drag, which leads to the result in Equation 21 (assuming for simplification that $\boldsymbol{v}_{\text{rel}} = \boldsymbol{v}$).

$$\dot{\mathcal{E}} = \boldsymbol{v} \cdot \boldsymbol{a}_D = \boldsymbol{v} \cdot (-B^*\rho v\boldsymbol{v}) = -B^*\rho v^3 \tag{21}$$

If the orbit is assumed circular then $v = \sqrt{\mu/a}$ and

$$\dot{\mathcal{E}} = -\left(\frac{\mu}{a}\right)^{\frac{3}{2}}\rho B^* \tag{22}$$

which can be substituted into Equation 20 to yield Equation 23.

$$\dot{a} = -2\sqrt{\mu a}\rho B^* \tag{23}$$

Substituting this into Equation 18 then gives Equation 24.

$$\ddot{M} = 3\frac{\mu}{a^2}\rho B^* \tag{24}$$

After integrating twice with respect to time from initial time t_0 to time t whilst using the perturbation theory approach of letting μ, a, and B^* be constants on the rights sides of the interposing equations gives Equation 25.

$$M(t) = M(t_0) + n_0(t - t_0) + \frac{3}{2}\frac{\mu}{a^2}\rho B^*(t - t_0)^2 \tag{25}$$

Equation 25 represents a simplified model for the mean anomaly of a circular orbit under the influence of air drag. When multiplied by the semi-major axis a the result is (for a circular orbit) an in-track distance. Then, considering that the problem may be stochastic, let the initial mean anomaly M_0, the initial mean motion n_0, and the ballistic coefficient B^* be statistically independent random variables (note that here the same assumption made in Chapter I applies—assume the probabilistic features of air drag can be captured by a single random variable, and let that random variable be B^*). Then, finally, the variance of this in-track distance is

$$P_{\text{in-track}} = \mathrm{E}\left[\left(aM(t_0) + an_0(t - t_0) + \frac{3}{2}\frac{\mu}{a}\rho B^*(t - t_0)^2\right)^2\right] \tag{26}$$

$$P_{\text{in-track}} = a^2\sigma_{M_0}^2 + a^2(t - t_0)^2\sigma_{n_0}^2 + \frac{9\mu^2}{4a^2}\rho^2(t - t_0)^4\sigma_{B^*}^2 \tag{27}$$

where cross terms featuring multiple random variables have an expectation of zero due to the assumption of statistical independence and $\sigma^2_{M_0}$, $\sigma^2_{n_0}$, and $\sigma^2_{B^*}$ are the variances of M_0, n_0, and B^*. In this equation the random variable B^* represents uncertainty caused by air drag, while the initial mean anomaly M_0 and initial mean motion n_0 represent the initial uncertainty present in the position and velocity of an orbiting satellite in the two-body problem.

Note that under this simplified model, which considers B^* to be the random constituent variable of air drag, the in-track variance is expected to growth with Δt^4. This result of Rich et al. appears to contrast with the results of Emmert et al., however this is not the case. It is important to note that the variety of anticipated in-track variance growth rates (Δt^3, Δt^4, and Δt^5) arise from different theoretical developments. The development of Rich et al. in Equations 18–27 chooses B^* as the random constituent variable of air drag, and assumes that other modeling errors are consumed by estimations of B^* or ignores them completely, assigning no assumptions or random processes to any errors in the atmospheric density ρ. Emmert et al. take a different approach—their development arises from assigning either white noise or Brownian motion random processes to the relative atmospheric density error. It's important to remember that the expected growth rate of Δt^4 produced by the method of Rich et al. and the growth rates of Δt^3 or Δt^5 produced by Emmert et al. are the expected growth rate of the variance of the *model* prediction error, based on the model used in the construction of the dynamical system. In other words, different expected growth rates arise from different formulations of the system stochastics.

Thus, it is entirely expected that the different theoretical formulations yield different expectations for the growth of in-track variance. The key similarity is that if air drag is stochastic, then the growth rate of the in-track variance is greatly increased beyond the Δt^2 that is expected for deterministic dynamics (if $\sigma^2_{B^*} = 0$ in

Equation 27).

4.1.2 Calculating Empirical Prediction Covariance Matrices

Analyzing the growth rate of prediction covariance matrices required the calculation of ensembles of true prediction error vectors according to

$$\boldsymbol{e}_{\text{true}} = \boldsymbol{X}_{\text{true}} - \boldsymbol{X}_{\text{pred}} \tag{28}$$

where $\boldsymbol{e}_{\text{true}}$ is the true prediction error, $\boldsymbol{X}_{\text{true}}$ is a representation of the true state of the satellite (though it cannot be perfectly known and thus cannot be precisely "true", see Section 3.2 for a discussion on sources of "truth data"), and $\boldsymbol{X}_{\text{pred}}$ is the state predicted via one of the prediction models discussed in Section 3.1.

For each scenario listed in Table 6, a number N of three-day predictions were made using each of the four prediction models, and error vectors were calculated at n evenly spaced output points between each prediction's initial time t_0 and final time t_f. This resulted in the creation of a collection of N propagation error functions $\boldsymbol{e}(\Delta t_i)$ for each scenario and prediction model combination, where Δt_i is defined by Equation 29.

$$\Delta t_i = \frac{(t_f - t_0)i}{n} \qquad\qquad i = \{0, \ldots, n\} \tag{29}$$

The initial time of each propagation within a collection was uniformly sampled from a given time window of interest (again see Table 6). In the case of the SGP4 models which use TLEs as input data, the initial time for each prediction was the closest TLE epoch time to the sampled t_0. This uniform sampling of initial propagation times removes any selection bias and buoys confidence that these empirical covariance matrices accurately reflect the true model prediction uncertainty for each model and scenario.

The method by which initial conditions were obtained for each prediction depended on the prediction model used. Initial conditions for SGP4 predictions were TLEs, which contain the necessary the epoch, position, velocity, and drag (B^*) data in a defined format. For SP predictions, the initial position, initial velocity, and B^* (which for deterministic uses is a constant for each prediction) were estimated from observational data using the non-linear least squares algorithm detailed in Appendix B.

After the predictions were carried out and ensembles of error vectors at discrete propagation times $\boldsymbol{e}(\Delta t_i)$ were available, the model prediction covariance matrix for each scenario/model pair was calculated as a function of propagation time according to Equation 30 [115, pg. 170].

$$P(\Delta t_i) = \mathrm{E}\left[\boldsymbol{e}(\Delta t_i)\boldsymbol{e}(\Delta t_i)^T\right] - \mathrm{E}\left[\boldsymbol{e}(\Delta t_i)\right]\mathrm{E}\left[\boldsymbol{e}(\Delta t_i)^T\right] \tag{30}$$

Covariance matrices (the central moment) were used because the mean error is not necessarily zero (even for large N), particularly in the in-track direction where imperfect estimates of the ballistic coefficient B^* may eventually lead to mis-modeled air drag.

4.1.3 Comparing Sources of Model Uncertainty

An assessment of the predominant source of the uncertainty observed in the empirical covariance matrices was also conducted for each SP scenario (SGP4 scenarios lack the necessary data for such an analysis, such as the average atmospheric density $\overline{\rho}$ in Equation 32). To accomplish this, a curve fit of the form of Equation 31 and in the likeness of Equation 27 was applied to the in-track prediction variance element ($P_{22} = P_{\text{in-track}}$) of each empirical prediction covariance matrix.

$$P_{22}(\Delta t) \approx \gamma + \beta\, \Delta t^2 + \alpha\, \Delta t^4 \tag{31}$$

Equation 27 was used as the basis of the curve fits (in lieu of those developed by Emmert et al. [12], for example) because the underlying development most closely matches the SP dynamics models and the relevant research hypotheses investigated in this document—wherein B^* is the representative random variable in air drag and no assumption regarding the air density error process is required (indeed density errors are assumed to be entirely absorbed by estimates of B^*). Note that the purpose of applying these curve fits was not to compare the validity of the expected growth rates or select an appropriate model. Rather, Rich et al.'s model was assumed to be a viable candidate based on the similarities between their development and this research's central paradigm. The purpose, then, of applying these curve fits was to compare the contributions of the various random variables to the overall prediction uncertainty, and specifically to test the hypothesis that air drag is the principal contributor.

The coefficients α, β, and γ from the polynomial curve-fits (Equation 31) where used to determine the dominant source of the observed in-track prediction uncertainty. Comparing these coefficients with the terms of Equation 27 and calculating average values of the semi-major axis ($\overline{a}$) and atmospheric density ($\overline{\rho}$) for each scenario allowed approximations of the variances $\sigma^2_{M_0}$, $\sigma^2_{n_0}$, and $\sigma^2_{B^*}$ to be calculated via Equation 32.

$$\sigma^2_{M_0} \approx \frac{\gamma}{\overline{a}^2} \qquad \sigma^2_{n_0} \approx \frac{\beta}{\overline{a}^2} \qquad \sigma^2_{B^*} \approx \frac{4\alpha\overline{a}^2}{9\mu^2\overline{\rho}^2} \tag{32}$$

The relative standard deviations ($\overline{\sigma}$) were then calculated according to

$$\overline{\sigma}_{M_0} = \frac{\sigma_{M_0}}{\overline{M}} \qquad \overline{\sigma}_{n_0} = \frac{\sigma_{n_0}}{\overline{n}} \qquad \overline{\sigma}_{B^*} = \frac{\sigma_{B^*}}{\overline{B^*}} \tag{33}$$

where $\overline{M}$, $\overline{n}$, and $\overline{B^*}$ are the average values of the mean anomaly, mean motion, and ballistic coefficient (note that M is a cyclical quantity, and as such the half-range value π was selected as the average as only the order of magnitude is of interest). The relative standard deviation is used here as a method of comparing the relative uncertainties of M_0, n_0, and B^* against each other.

4.2 Results

Prediction covariance matrices were calculated for each of the scenarios in Table 6 for each of the four prediction methods described in Section 3.1 using $N = 1000$ predictions for the SP models and $N = 20000$ predictions for the SGP4 models. (As an aside, 20000 predictions were calculated for the SGP4 models despite the limited number of possible TLE epochs to utilize the same underlying code as SP predictions, which randomly samples initial times. Using a large number of predictions ensured that each of the available TLEs within the scenario interval was selected about the same number of times to avoid biasing.) Figure 8a shows example results for the GRACE-A Low Solar scenario for SP A, for the purposes of demonstrating that only the in-track element (P_{22}) of the covariance matrix is distinguishable from zero. Figure 8b depicts example results for the same scenario for the SGP4 A propagator, and shows that other covariance elements do in fact deviate perceptibly from zero, however the in-track variance remains orders of magnitude larger. All tested scenarios exhibited similar behavior and, based on the dominance of the in-track covariance matrix element, plots of the remaining results depict the in-track variance only for visual clarity. These are Figures 9–11, which show the in-track variance for all scenarios of each satellite along with the polynomial curve fits described in the preceding section. Note that care should be taken in comparing results from different scenarios against one another (for example the high and low solar pair of scenarios for a particular satellite), as the scenarios are separated by several years and various properties of the orbit (the semi-major axis, for example) had likely changed. The purpose of including high and low solar scenarios in this research was to obtain results for a range of environments to help validate the wide applicability of any conclusions to LEO orbits, not delve into the causal relationship of the solar environment to in-track uncertainty (though that may be of interest for future research).

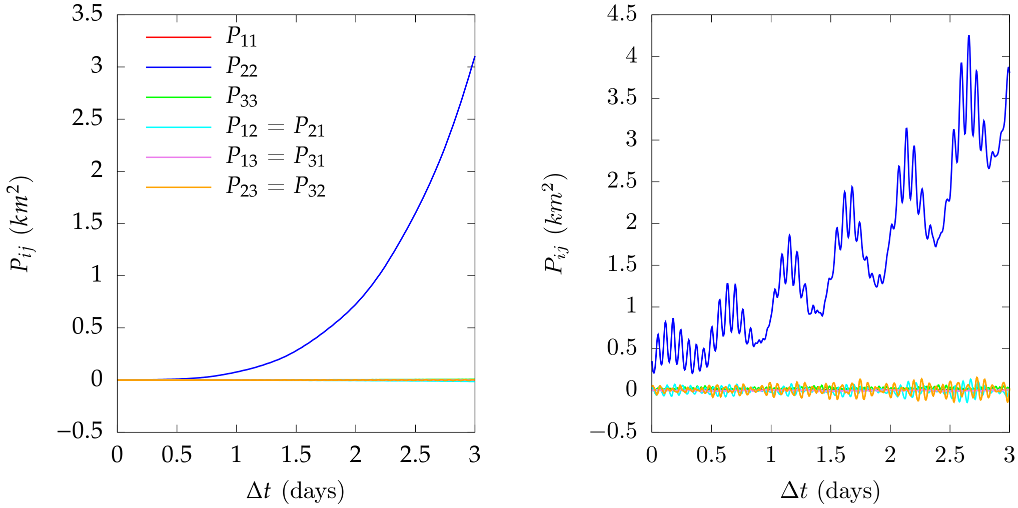

(a) SP A

(b) SGP4 A

Figure 8. Example Full Empirical Covariance Matrices

The results in Figures 9–11 demonstrate several things. For one, note that the results of SGP4 A and SGP4 B match very closely (so much so that they tend to overlap causing one to not be visible), which indicates that for this purpose the Vallado and DoD implementations of SGP4 produce nearly identical results.

Additionally, the growth curves of the in-track prediction variance for the two SP propagators are very similar, despite the two models using disparate atmospheric models. This agreement between the two SP models gives at least some indication that using B^* as the only random variable reasonably captures the in-

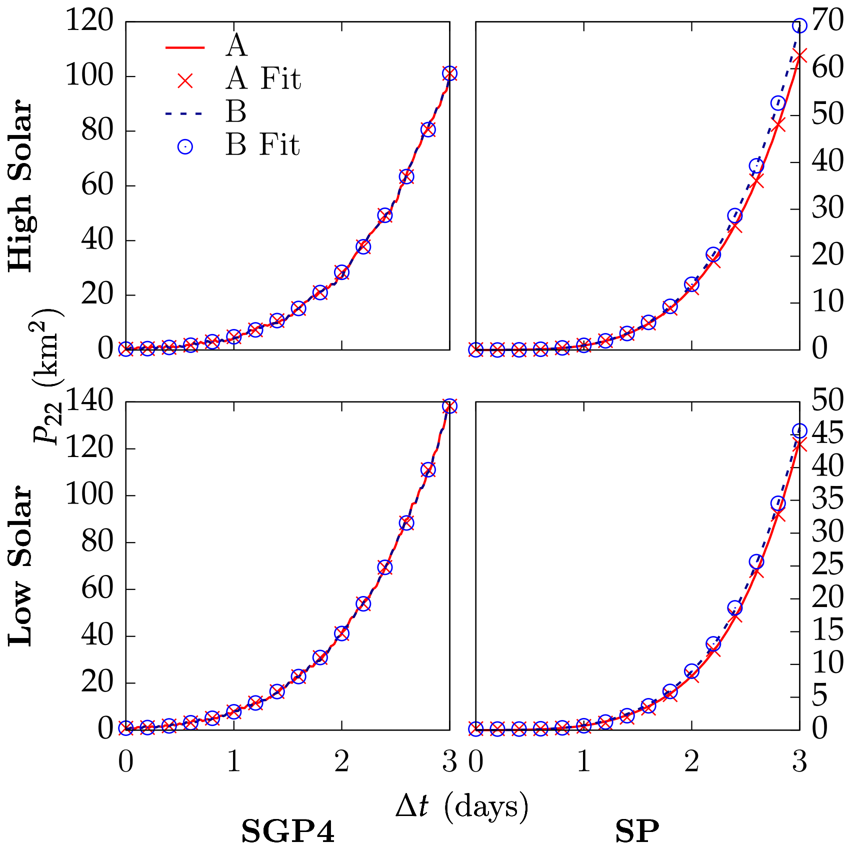

Figure 9. Empirical In-track Variance, CHAMP

track uncertainty without constraining the choice of atmospheric density model. This is possible even though the two atmospheric models give quite different values for the air density because B^* is estimated from observational data for each model, such that the differences between the atmospheric models tend to be cancelled out as modeling errors are absorbed by the estimation.

Differences between the fidelity of the SP and SGP4 prediction models become apparent in Figures 9–11 as well. For example, the SGP4 prediction variances oscillate considerably while those of the SP models do not. This is attributable to SGP4 being an analytical approximation with sinusoidal terms in it, a fact which becomes particularly evident when the in-track prediction variance becomes small enough that the scaling of the y-axes reduces and the oscillations become pro-

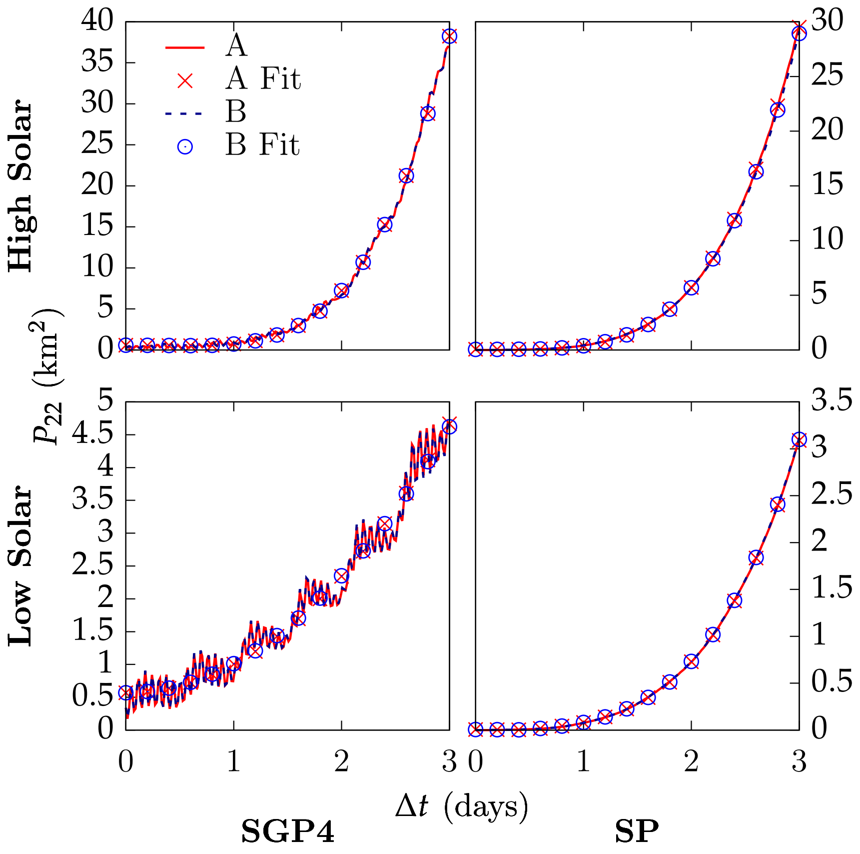

Figure 10. Empirical In-track Variance, GRACE-A

found, as in Figures 10 and 11.

Figures 10 and 11 also reveal that the initial prediction variance when using SGP4 is larger than when using SP, which is due to the use of TLEs as input data for the SGP4 models. The SP models do not exhibit this behavior as their initial conditions are estimated from the representative data, resulting in very small initial errors (generally less than a meter).

Results of the polynomial coefficient analysis described in Section 4.1.3 are tabulated in Table 8, which also lists the values for the average semi-major axis and average atmospheric density. These results represent the SP B prediction model, as gathering the requisite data (specifically the atmospheric density) is impossible for the SGP4 propagators and covariance growth results of SP A are duplicative.

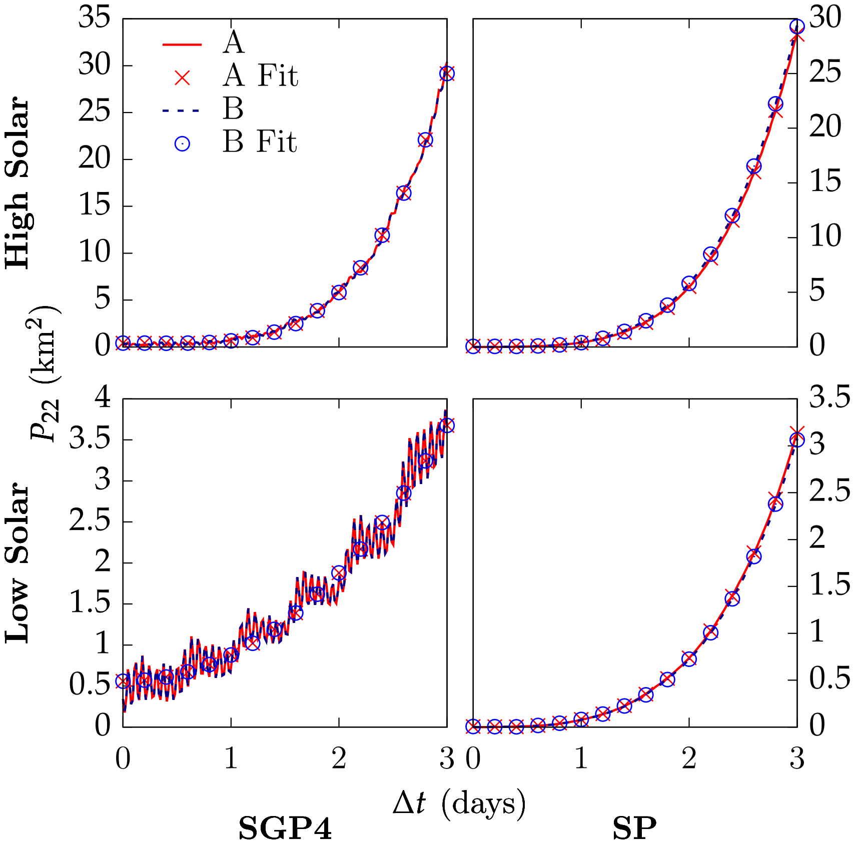

Figure 11. Empirical In-track Variance, GRACE-B

As is the case for Figures 9–11, care should be taken if comparing rows of Table 8 to one another, for the same reasons.

These results indicate that $\overline{\sigma}_{B^*}$ is much larger than either $\overline{\sigma}_{M_0}$ or $\overline{\sigma}_{n_0}$ for each scenario, confirming that the uncertainty due to air drag is the dominant source of in-track prediction uncertainty for LEO satellites (at least when compared to uncertainties in the mean anomaly and mean motion). This is true for both high and low levels of solar activity for all scenarios. These results also demonstrate that the growth-rate of in-track variance is primarily with Δt^4, indicating that B^* is acting as a random variable and that air drag is a stochastic effect.

Finally, though this research is concerned primarily with prediction uncertainty, this is a good opportunity to discuss the accuracy of each prediction

Table 8. Relative Standard Deviations of Mean Anomaly, Mean Motion, and Ballistic Coefficient

Satellite	Solar Activity	$\overline{\rho}$ ($\mathrm{kg\,km^{-3}}$)	$\overline{a}$ (km)	$\overline{\sigma}_{M_0}$ (%)	$\overline{\sigma}_{n_0}$ (%)	$\overline{\sigma}_{B^*}$ (%)
CHAMP	Low	1.99×10^{-3}	6705.8	< 0.01	< 0.01	22
CHAMP	High	1.85×10^{-3}	6808.5	< 0.01	< 0.01	24
GRACE A	Low	1.06×10^{-4}	6839.8	< 0.01	< 0.01	63
GRACE A	High	1.61×10^{-3}	6797.5	< 0.01	< 0.01	13
GRACE B	Low	1.06×10^{-4}	6839.7	< 0.01	< 0.01	64
GRACE B	High	1.62×10^{-3}	6797.9	< 0.01	< 0.01	13

model. It was mentioned briefly in Section 3.1 that the SP models in particular are sensitive to various input parameters and Figure 1 gives some indication of the average modeling error, however the ensembles of error vectors used to calculate the covariance matrices discussed above are useful for visualizing model accuracy in greater detail. Therefore, the respective accuracy of each model, using the parameters given in Table 1, is shown for the CHAMP High Solar scenario in Figure 12.

Note that the SGP4 prediction models have a significantly larger average error magnitude at $\Delta t = 0$, which reflects some disagreement between the CFSCC TLEs used for SGP4 and the more precise vector data. Other scenarios showed similar error variance between the average TLE and the precise vector data at the epoch time, which is unsurprising given that SGP4 is an analytical approximation.

Also note that the SGP4 prediction models here are comparable in accuracy to the SP models as parameterized. If increased accuracy is desired the SP models can be made significantly more accurate by increasing both the order and degree of the geopotential and N_{LS}. This is demonstrated in Figure 13 for a geopotential degree/order of 35 and $N_{\mathrm{LS}} = 1080$, calculated using 100 propagations. As mentioned in Chapter III, refining the accuracy of the SP models this way increases computation time significantly, and therefore the original parameters of Table 1

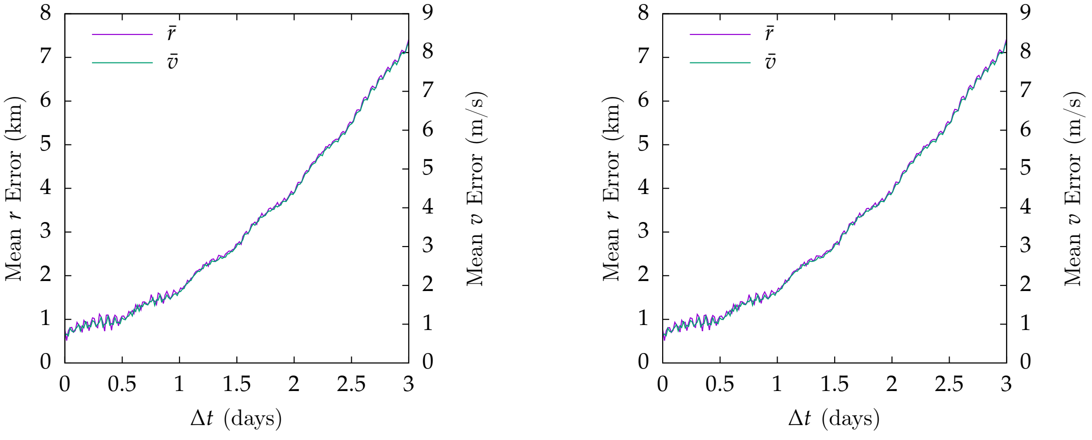

(a) SGP4 A

(b) SGP4 B

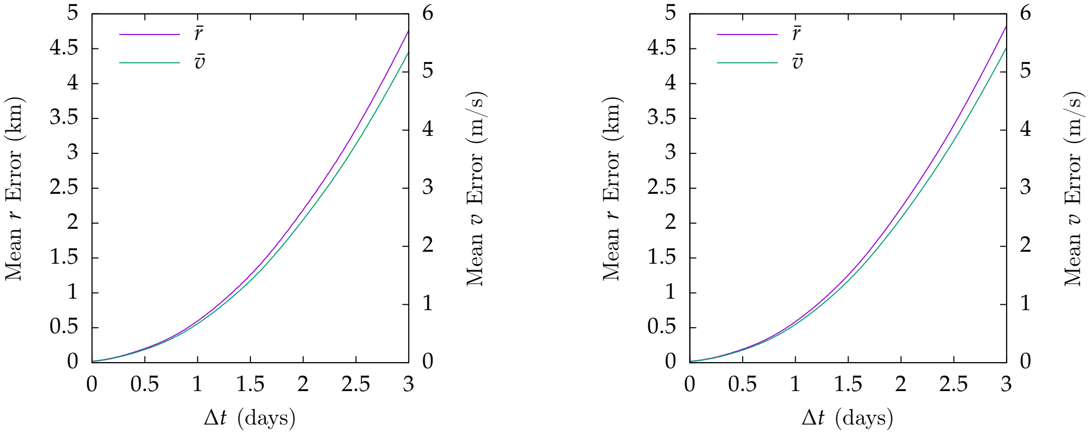

(c) SP A

(d) SP B

Figure 12. Average Magnitude of Empirical Position and Velocity Errors, CHAMP High Solar

were used throughout this research as the uncertainty of the model predictions and the uncertainty's realism are of the greatest interest in this research.

4.3 Conclusions

The results of the preceding section confirm that the air drag on LEO satellites dramatically increases in-track model prediction uncertainty. Further, the relative uncertainty analyses via polynomial fit coefficients confirm that air drag is the principal source of in-track model prediction uncertainty, as hypothesized in

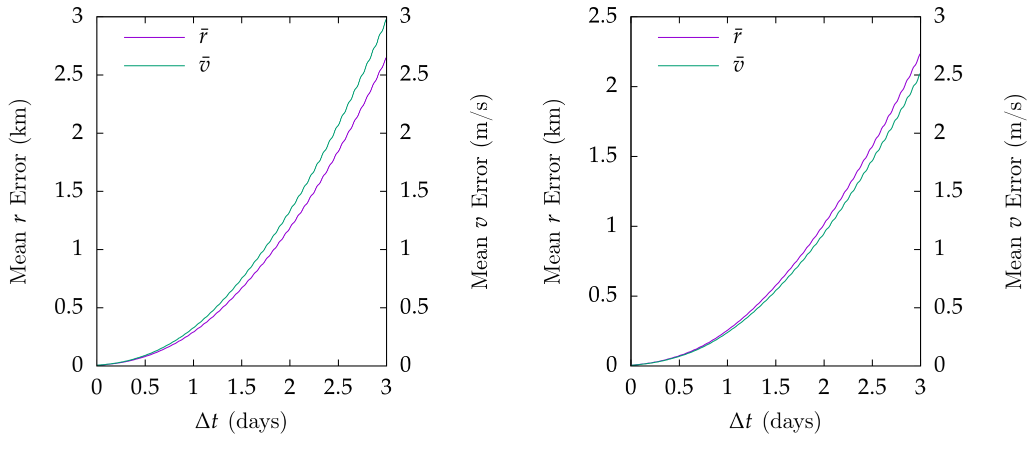

(a) SP A

(b) SP B

Figure 13. Average Magnitude of Empirical Position and Velocity Errors, CHAMP High Solar, High Fidelity Special Perturbations Models

Research Hypothesis 1. This confirms the expectation of the theoretical developments presented above, and also satisfies our intuition given the difficulty associated with predicting the behavior of the atmosphere.

Also, the fact that the two SP models with dissimilar atmospheric models calculated very similar empirical covariance matrices via estimation of B^* implies that there is some validity to the hypothesis that a single random variable in the air drag equation can capture model prediction uncertainty without restricting the atmospheric model used.

A key implication of these results is that air drag is a stochastic effect. This, along with known difficulties in predicting various uncertain drag factors (such as the behavior of the upper atmosphere), implies that the dynamics of a LEO satellite may be stochastic and therefore that some dynamical variables may really be random processes. This leads to the next chapter, wherein the ballistic coefficient B^* is modeled and analyzed as a random process to test this hypothesis.

V. B^* As a Random Process

The preceding chapter concluded that air drag dramatically increases in-track model prediction uncertainty for LEO satellites and hypothesized that air drag may be dynamically stochastic. This would mean that at least one dynamical variable within the system is really a random process. Results of Chapter IV also began to substantiate the hypothesis that a single random variable within air drag can capture model prediction uncertainty.

Chapter I introduced the notion that if a single random variable is to be used in the air drag equation, then choosing the ballistic coefficient B^* has potential benefits. This was also reinforced in the preceding chapter as the SP models were able to produce similar characterizations of uncertainty by estimating initial states and B^* from observational data.

This chapter examines B^* as a random process, with the aim of incorporating it into a stochastic dynamics model for the prediction of LEO satellites in the following chapter. This analysis corresponds to Research Tasks 2 and 3.

5.1 Methodology

5.1.1 Characterizing Random Processes

Before considering B^* as a random process, first consider the definition of a random process in general. Let T denote a time of interest and Ω be a sample space of relevant function arguments, including potential random variables. Then, for the purposes of this research, consider a "random process" $\boldsymbol{x}$ to be a T and Ω-dependent function, such that for any fixed time instant $t \in T$ the value of the function $\boldsymbol{x}(t, \cdot)$ is a random variable [116, pg. 133]. Additionally, for each realization of variables $\omega \in \Omega$, the time-function $\boldsymbol{x}(\cdot, \omega)$ is a "realization" of the random process [116, pg. 134].

Strictly speaking, a random process can only be fully characterized by the complete probability density function (PDF) formed from the set of random variables as functions of time, which may not exist or may be very difficult to calculate. As such, stochastic processes are often described by moments of the PDFs, and if the random variables within a process are Gaussian then the first two moments contain enough information to completely characterize the process [116, pg. 135].

It will be useful to define several properties of random processes, including the first two central moments referenced above, as shown in Equations 34–38 (obtained from Maybeck [116, pgs. 136–137]). The first two moments of a random process $\boldsymbol{x}(t)$ are given by the mean value function (Equation 34)

$$\boldsymbol{m}_x(t) \triangleq \mathrm{E}\{\boldsymbol{x}(t)\} \tag{34}$$

and the covariance matrix (second central moment, Equation 35).

$$\boldsymbol{P}_{xx}(t) \triangleq \mathrm{E}\left\{[\boldsymbol{x}(t) - \boldsymbol{m}_x(t)][\boldsymbol{x}(t) - \boldsymbol{m}_x(t)]^T\right\} \tag{35}$$

The covariance matrix can be generalized to include time-dependent behavior of $\boldsymbol{x}(t)$ by defining the covariance kernel, given by Equation 36.

$$\boldsymbol{P}_{xx}(t_1, t_2) \triangleq \mathrm{E}\left\{[\boldsymbol{x}(t_1) - \boldsymbol{m}_x(t_1)][\boldsymbol{x}(t_2) - \boldsymbol{m}_x(t_2)]^T\right\} \tag{36}$$

Finally, the correlation matrix (second non-central moment, Equation 37) is

$$\Psi_{xx}(t) \triangleq \mathrm{E}\left\{\boldsymbol{x}(t)\boldsymbol{x}(t)^T\right\} \tag{37}$$

and can be similarly generalized to the correlation kernel in Equation 38.

$$\Psi_{xx}(t_1, t_2) \triangleq \mathrm{E}\left\{\boldsymbol{x}(t_1)\boldsymbol{x}(t_2)^T\right\} \tag{38}$$

These relationships are useful both for categorizing random processes and for assessing stationarity and ergodicity.

The stationarity of the B^* random process was of interest in this research because establishing or assuming stationarity permits the calculation of the process autocorrelation function as a function of a time difference $\tau = t_1 - t_2$ only, indicating that the process does not depend on the absolute time, but only the relative time within the process. There are two types of stationarity, strict and wide-sense stationarity. As wide-sense stationarity is generally easier to establish, the B^* random process was tested for wide-sense stationarity using the following criteria [116, pg. 140].

1. The correlation matrix (Equation 37) is finite.
2. The mean value function (Equation 34) is constant.
3. The covariance and correlation matrices (Equations 35 and 37) are constant.

If the B^* random process proves to be stationary within a time frame of interest, it implies that it is a constant mean process for which the covariance and correlation have no dependence on absolute time within that time frame.

Another property of random processes that was investigated with respect to the B^* random process is ergodicity. Ergodicity is, formally, a property only of strictly stationary processes. Strict stationarity was not established for the B^* random process, however as the B^* random process was assessed regarding wide-sense stationarity making an ergodic assumption was partially justified by comparing statistics calculated from many realizations of the B^* random process with statistics calculated from a single realization. If such statistics of a random process prove comparable, the process is more likely to be ergodic [116, pg. 144]. Asserting ergodicity remains an assumption and fully justifying it would require strict stationarity and an infinitely long realization of the process, but by performing this test the assumption was at least provided some justification.

Whether or not the B^* random process is ergodic informs if the process can be characterized by analyzing a single realization. This is important because a single time-series of B^* estimates is exactly what is calculated from observational data of satellites' positions and velocities in this chapter, and could potentially be calculated autonomously on-board on a satellite if data was available.

Another purpose of assessing the stationarity and ergodicity of the B^* random process was to inform the calculation of the autocorrelation function. The autocorrelation function is a method of characterizing a random process, and in the case of a stationary process is dependent only on the time lag variable τ. The autocorrelation function was calculated by modifying Equation 38 for the correlation kernel such that the result is dependent only on τ, as in Equation 39 [116, pg. 140].

$$\Psi_{xx}(t, t+\tau) \rightarrow \Psi_{xx}(\tau) = \mathrm{E}\left\{\boldsymbol{x}(t)\boldsymbol{x}(t+\tau)^T\right\} \tag{39}$$

5.1.2 Calculating B^* Time Series

Before discussing how B^* random processes were analyzed, first consider what is meant by the phrase "B^* random process". Strictly speaking, a B^* random process exists for the entire orbital life of a satellite, but a LEO satellite experiences potentially drastic changes in its environment over this lifespan (due to the 11-year solar cycle and its effect on the atmosphere, orbital maneuvers or decay, etc.). As such, a satellite's B^* random process is likely not stationary when considered over the lifespan of the satellite. Therefore, references to a B^* random process are meant as references to a section of a satellite's overall B^* random process on some time interval within which it remains stationary as defined above.

Time series of B^* values that span the time intervals listed in Table 7 were obtained by estimating individual values of B^* from each satellite's position and velocity observational data using non-linear least squares with the SP prediction models. These B^* values were estimated at evenly spaced output points. Two types of B^* time series were calculated: single realizations and ensembles. In the single realization case, a single time series was calculated for the entire interval. In the ensemble case, a number of initial times were randomly sampled from within the time interval of interest and B^* time series of a chosen length were estimated from each sampled initial time. Note that ensembles constructed in this manner are not precisely ensembles of the same random process, as the initial time and hence the satellite's environment are different for each ensemble member. However, this is the best method available for calculating ensembles of B^* time series given the available data, and it is assumed that ensemble members calculated from a window in which the B^* random process is relatively stationary are similar enough in their properties to be considered members of the same random process.

It is these time series which were then analyzed as realizations of empirical B^* random processes, with the ensemble cases being used primarily to assess random process properties such as stationarity and ergodicity and the single realizations being primarily used for parameterization (though this can be conducted with either type) and in the stochastic prediction models of Chapter VI.

There were also many parameters which could be tuned during the process of generating these B^* time series, such as the spacing of the output points (which corresponds to the sampling rate of B^* points), how long each time series should be, how many time series to generate in the ensemble case (with initial times randomly sampled from within the interval), and how much data to use as input to the least squares algorithm for each B^* estimate. Values used for these parameters are included with relevant results in the next section.

5.1.3 Gauss-Markov Random Processes

Several researchers have applied Gauss-Markov (or Ornstein-Uhlenbeck) processes to the stochastic behavior of satellite air drag [6, 9, 14–16, 94]. For a process to be a Gauss-Markov process, it must first be a Gaussian random process [116, pg. 146]. A random process $\boldsymbol{x}(t)$ is Gaussian if the joint PDF for any finite collection of process random variables $\{\boldsymbol{x}(t_1), \boldsymbol{x}(t_2), \dots\}$ is Gaussian [116, pg. 139].

A Markov process is any random process for which the PDF at the current time step conditioned on *all* previous time steps is equivalent to the PDF conditioned on only the previous time step [116, pg. 146]. In other words a Markov process is fully characterized by the information available from the preceding time step, without need of information prior to that. Maybeck puts it like this: "the Markov property for stochastic processes is conceptually analogous to the ability to define a system state for deterministic processes" [116, pg. 146].

With respect to the B^* random process considered in this research, recall that B^* is the only variable of satellite air drag to be modeled stochastically, and that values of B^* are estimated from observational data using the implementations of special perturbations in the SP prediction models. As such, while B^* remains related to physical properties of the satellite, its stochastic behavior is expected to accumulate effects of other variables which are stochastic in reality but modeled deterministically in these models. Therefore, it was assumed that this B^* process will prove to be Gaussian due to the accumulating effect of several error sources.

Additionally, the history of B^* values prior to the "current" value has no intuitive bearing on the fluctuation of B^* in the future—the previous time history does not inform the predicted deviation of the next value from the mean (though it does give an idea of the expected future mean)—and the B^* random process was therefore assumed to satisfy the Markov property. Therefore, it will be assumed for the remainder of this document that B^* random processes, in this context, are Gauss-Markov processes.

Finally, note that the B^* random process for a satellite will not be zero-mean (if B^* were zero mean it would mean that the average effect of drag would be that there was none at all). Therefore, consider instead the following representation of B^*

$$B^* = B_0^* + B_e^* \tag{40}$$

in which B_0^* is the mean of the B^* time series and B_e^* is a zero-mean Gauss-Markov process which represents the stochastic deviation of B^* from its expected mean value B_0^*.

5.1.4 Parameterizing and Simulating B^* Random Processes

Creating a stochastic prediction method that leverages calculated B^* random processes required obtaining the parameters of the B^* random process from the time series. This was accomplished via calculation of process statistics and the autocorrelation function. An example autocorrelation function from a one-day long B^* time series from the CHAMP High Solar scenario is shown in Figure 14. Considering that B^* was assumed to be a Gauss-Markov process and noticing the dampened oscillatory nature of the autocorrelation, modeling B^* random processes as second-order Gauss-Markov (SOGM) processes was a logical choice. This isn't the only plausible choice of random process model—a first-order Gauss Markov process could be sufficient to approximate the system stochastics, for example. However, the SOGM process model was selected to allow simulated B_e^* random processes to match their empirical counterparts as closely as possible.

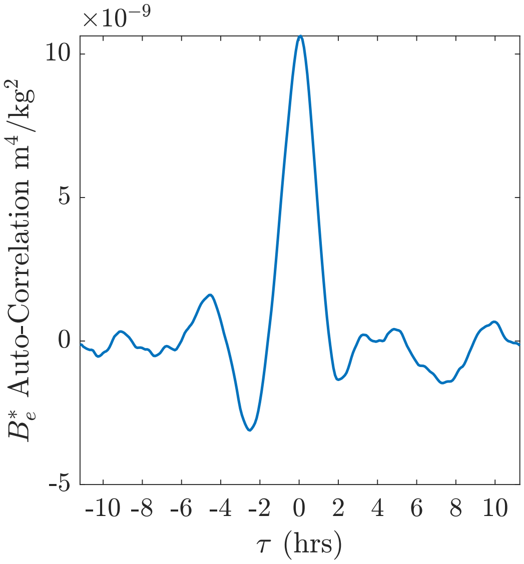

Figure 14. Example Empirical B_e^* Autocorrelation Function, CHAMP High Solar

The general autocorrelation function for a SOGM process is given in Equation 41

$$\Psi(\tau) = \frac{\sigma^2}{\cos(\eta)} \exp\left(-\xi\omega_n|\tau|\right) \cos\left(\sqrt{1-\xi^2}\,\omega_n\tau - \eta\right) \tag{41}$$

where σ^2, η, ξ, and ω_n are the four parameters which define the behavior of the process. It is these parameters which needed to be extracted from an empirical autocorrelation such as the one in Figure 14.

The variance of the B_e^* random process σ^2 was readily available either via direction calculation from the values or as the peak value of the empirical autocorrelation when $\tau = 0$. Then, by examining the second cosine term in Equation 41 the frequency of the oscillations is given by $f = \sqrt{1-\xi^2}\omega_n$. The period of the oscillation can be read from the autocorrelation and is related to the frequency according to $f = 2\pi/P$. Combining these gives Equation 42.

$$\omega_n = \frac{2\pi}{P\sqrt{1-\xi^2}} \tag{42}$$

Obtaining the oscillation period P from the autocorrelation was simplified by assuming that the time-lag of the first valley to the right of the y-axis τ_m was equal to half the period, which is akin to assuming that the slope of the autocorrelation function at the peak is zero. An example location of τ_m and the corresponding value of the autocorrelation $\Psi_m = \Psi(\tau_m)$ is illustrated in Figure 15. The derivative of the autocorrelation with respect to τ is (for the half of the domain to the right of and including $\tau = 0$)

$$\begin{aligned}\Psi'(\tau) = \frac{\sigma^2\omega_n}{\cos(\eta)} \exp\left(-\xi\omega_n\tau\right) \Bigg[& \sqrt{1-\xi^2}\ \sin\left(\eta - \omega_n\sqrt{1-\xi^2}\ \tau\right) \\ & - \xi\cos\left(\eta - \omega_n\sqrt{1-\xi^2}\ \tau\right)\Bigg], \quad \tau \geq 0\end{aligned} \tag{43}$$

and employing the assumption that the slope is zero at the peak ($\Psi'(0) = 0$) gives

$$0 = \frac{\sigma^2\omega_n}{\cos(\eta)} \left(\sqrt{1-\xi^2}\sin\left(\eta\right)\right) - \xi\cos\left(\eta\right) \tag{44}$$

which simplifies to Equation 45.

$$\tan\eta = \frac{\xi}{\sqrt{1-\xi^2}} \tag{45}$$

Thus Equations 42 and 45 give expressions for η and ω_n in terms of only ξ and known period P.

To estimate ξ, consider the exponential decay term $\exp\left(-\xi\omega_n|\tau|\right)$ which dampens the oscillations of the autocorrelation. At τ_m, the time-lag of the first valley, the

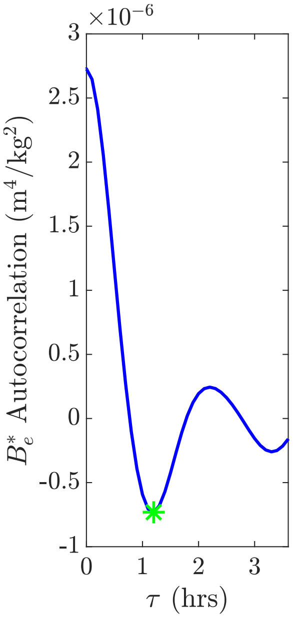

Figure 15. Location of the Point (τ_m, Ψ_m) on Example B_e^* Autocorrelation

oscillation is at its minimum. Given the behavior of the cosine function, this implies that $\sqrt{1-\xi^2}\omega_n\tau_m = \pi$ (this can be equivalently obtained using Equation 42 and recalling that $P = 2\tau_m$). Substituting this relationship into Equation 41 and removing the absolute value as only the $\tau_m > 0$ half of the autocorrelation is being considered gives Equation 46.

$$\begin{aligned}\Psi_m &= \frac{\sigma^2}{\cos(\eta)} \exp\left(-\xi\omega_n\tau_m\right) \cos\left(\pi - \eta\right) \\ \Psi_m &= \frac{\sigma^2}{\cos(\eta)} \exp\left(-\xi\omega_n\tau_m\right) \left(-\cos\left(\eta\right)\right) \\ \Psi_m &= -\sigma^2 \exp\left(-\xi\omega_n\tau_m\right) \qquad (46)\end{aligned}$$

Solving Equation 46 for ω_n yields

$$\omega_n = \frac{-1}{\xi\tau_m} \ln\left(\frac{-\Psi_m}{\sigma^2}\right) \qquad (47)$$

which, letting $\gamma = \ln(-\Psi_m/\sigma^2)$ and substituting $\tau_m = P/2$ in the denominator gives Equation 48.

$$\omega_n = \frac{-2\gamma}{\xi P} \tag{48}$$

Finally, equating Equations 48 and 42 gives the relationship

$$\frac{-2\gamma}{\xi P} = \frac{2\pi}{P\sqrt{1-\xi^2}} \tag{49}$$

which simplifies to give the result in Equation 50.

$$\xi^2 = \frac{1}{\left(\frac{\pi}{\gamma}\right)^2 + 1}, \quad \text{where} \quad \gamma = \ln\left(\frac{-\Psi_m}{\sigma^2}\right) \tag{50}$$

Therefore, given σ^2 and a single point from the autocorrelation $(\tau_m\,,\,\Psi_m)$, the three other parameters of the SOGM process model could be quickly approximated using Equations 50, 42,and 45. While this parameterization was easy to implement programmatically and yielded good results considering that the SOGM process is an approximate model for the B_e^* random processes, it is not the only way to divine the random process (RP) parameters from the estimated time series. Least squares estimation could have been applied to problem, for example, but the above method was developed and used for its simplicity and speed.

These parameters have multiple uses in upcoming chapters, one of which includes generating realizations of B_e^* random processes for use in Monte Carlo simulation. In order to do this, the shaping filter given in Equation 51 was used [116, pg. 183].

$$\begin{bmatrix} \dot{x}_1(t) \\ \dot{x}_2(t) \end{bmatrix} = \begin{bmatrix} 0 & 1 \\ -\omega_n^2 & -2\xi\omega_n \end{bmatrix} \begin{bmatrix} x_1(t) \\ x_2(t) \end{bmatrix} + \begin{bmatrix} a \\ c \end{bmatrix} w(t) \tag{51}$$

$$\alpha = \arctan(\xi / \sqrt{1-\xi^2}) = \eta \tag{52}$$

$$a = \sqrt{(2\sigma^2 / \cos(\eta))\omega_n \sin(\alpha - \eta)} = 0 \tag{53}$$

$$b = \sqrt{(2\sigma^2 / \cos(\eta))\omega_n^3 \sin(\alpha + \eta)} \tag{54}$$

$$c = b - 2a\xi\omega_n \tag{55}$$

In this two-state linear shaping filter state x_1 is the B_e^* random process realization and $w(t)$ is scalar white Gaussian noise. Note that $\eta = \alpha$ and $a = 0$ are mathematical consequences of the assumptions made above that $P = 2\tau_m$ and $\Psi'(0) = 0$. This stochastic system of equations was simulated using random draws from the standard normal distribution for $w(t)$ via numerical integration.

To illustrate the calculation, parameterization, and generation of B_e^* random processes the SOGM model, Figure 16 presents autocorrelations of three example B_e^* random processes—one empirically calculated, one plotted using Equation 41 and parameters obtained using the above parameterization method, and one generated via Equation 51 using those same parameters and 500 realizations.

Note from the figure both that the approximate parameterization and subsequent generated results closely match the empirical result through at least the first valley, but less well after that. This is to be expected when working with autocorrelations calculated from real-world observational data, as the SOGM process model is a mathematical ideal that is rarely exactly realized in reality. All told, the SOGM process model was determined to be a sensible approximation of empirical B_e^* random processes, and was used through the remainder of this research.

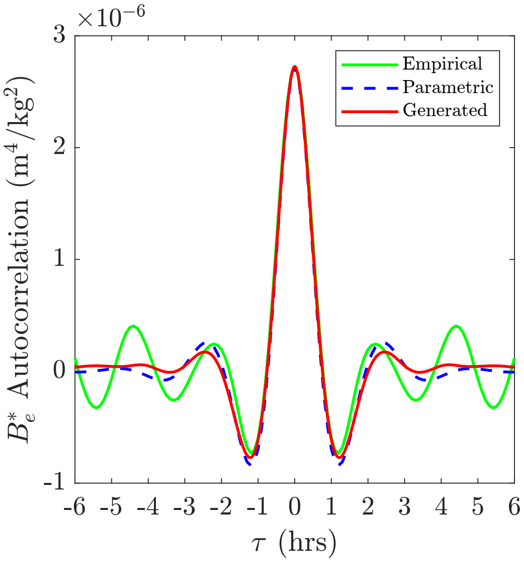

Figure 16. Example Empirical, Parameterized, and Generated B_e^* Autocorrelation Functions

5.2 Results

The methodology above was used to calculate ensembles and single realizations of B_e^* time series for the CHAMP satellite. Ensembles consisted of 300 half-day long realizations from 1–30 Jun 2001 and single realizations were for the 7-day time period preceding Jun 8, 2001 10:00:00 UTC (the date-time group for stochastic propagations given in Table 7). Additional satellites and time scenarios are not referenced in this chapter for the sake of brevity, however the method described above applies to all tested scenarios and was used to obtain the results of the next chapter. Figure 17 shows the ensemble time series, calculated using the SP B propagator (results from the SP A propagator were very similar and are covered in more detail in the next chapter).

These time-series were created for two values of N_{LS}, the number of data points given to the least squares algorithm for the estimate of each B^* value. Various parameters affect the calculation of these time series as discussed in Section 3.1.2, but N_{LS} has an additional effect relating to the frequency the B_e^* random process

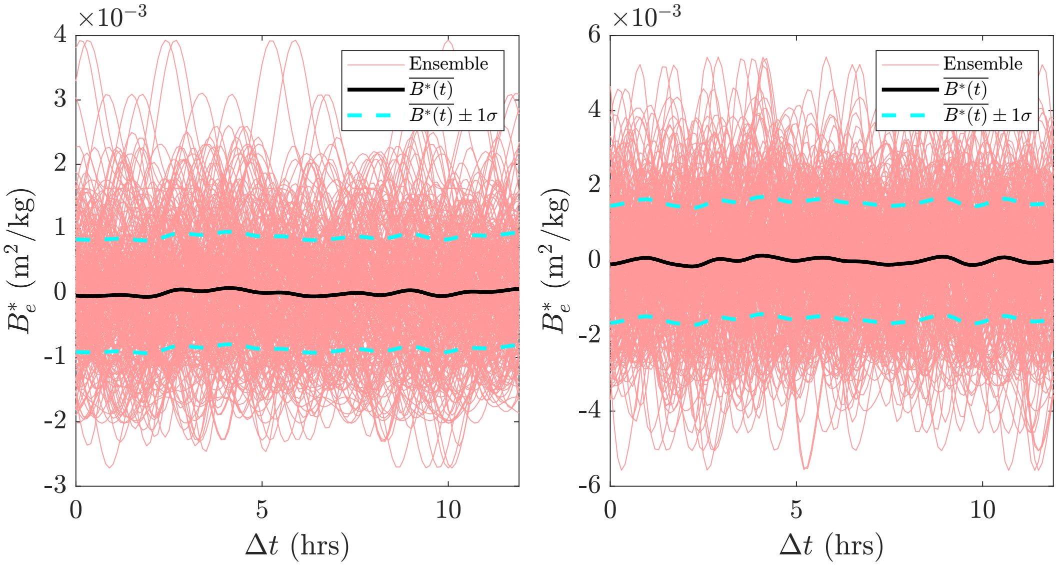

(a) $N_{\text{LS}} = 540$ (b) $N_{\text{LS}} = 360$

Figure 17. Ensembles of Estimated B_e^* Time Series

oscillations.

The effect is visible in Figure 17, but is more obvious in Figure 20, which shows two-dimensional autocorrelation functions of both types of time series (ensemble and single realization) for both values of N_{LS} calculated according to Equation 39. The output spacing of input data for these analyses is 30 seconds, which means that an N_{LS} value of 360 is equivalent to 180 minutes or 3 hours of data being used as input for the least squares algorithm, while $N_{\text{LS}} = 540$ corresponds to 270 minutes/4.5 hours. Couple this information with the fact that least squares estimates for B^* are returned from the middle of the supplied data and the effect of N_{LS} becomes clear: N_{LS} directly effects when the calculated B^* time series de-correlates with itself (at what time shift τ the first valleys appear in the autocorrelation on either side of $\tau = 0$). Note that when $N_{\text{LS}} = 540$ (4.5 hours) the autocorrelation in Figure 20a bottoms out at about 2.25 hours either side of $\tau = 0$, while for $N_{\text{LS}} = 360$ (3 hours) the valleys in Figure 20b are at approximately $\tau = \pm 1.5$ hours. This was a sensible discovery to make, as the estimate of B^* returned for a given time in the time series was based only on the data provided to the least squares algorithm, and the next point was based on the same amount of data but that data had been shifted down the timeline of the time-series. Further, it is not surprising that altering N_{LS} effects the character of the calculated B^* process, for the same reasons that were discussed in Section 3.1.2.

For the purposes of assessing stationarity, first note that in Figure 17 the mean value functions of the ensembles are relatively constant (a requirement of wide-sense stationarity) and also stay quite nearly zero (which is what the B_e^* construction of Equation 40 ensures). Additionally, Figure 18 shows the three-dimensional autocorrelation surface of the B_e^* ensembles, calculated according to Equation 38. Note that the "ridge" or "peak" of this surface, which occurs when $\Delta t_1 = \Delta t_2$, is fairly constant and doesn't tend to increase or decrease steadily. (Note Δt_1 and Δt_2 are used instead of t_1 and t_2 because the ensembles are from different times within the time window and are instead aligned via the time elapsed since t_0.) That the peak of the correlation is relatively constant indicates that the process variance is roughly constant with Δt, a requirement of wide-sense stationarity. Further, Figure 19 shows the correlation surface rotated to look flattened as a two-dimensional autocorrelation dependent only on time-lag would look. Indeed, a "slice" of the surface taken across either Figure 18a or 18b from equal points on the two base axes represents an autocorrelation of the random sample of the ensembles at a given $\Delta t_1 = \Delta t_2$. Noticing from Figure 19 that these autocorrelations are relatively constant indicates that the autocorrelation is dependent on the time lag $\tau = \Delta t_1 - \Delta t_2$ only (another requirement of wide sense stationarity), and can be represented by a two-dimensional autocorrelation calculated via Equation 39.

The preceding figures provide evidence for assuming that the B_e^* random process is wide-sense stationary, at least on the time scales investigated, based on

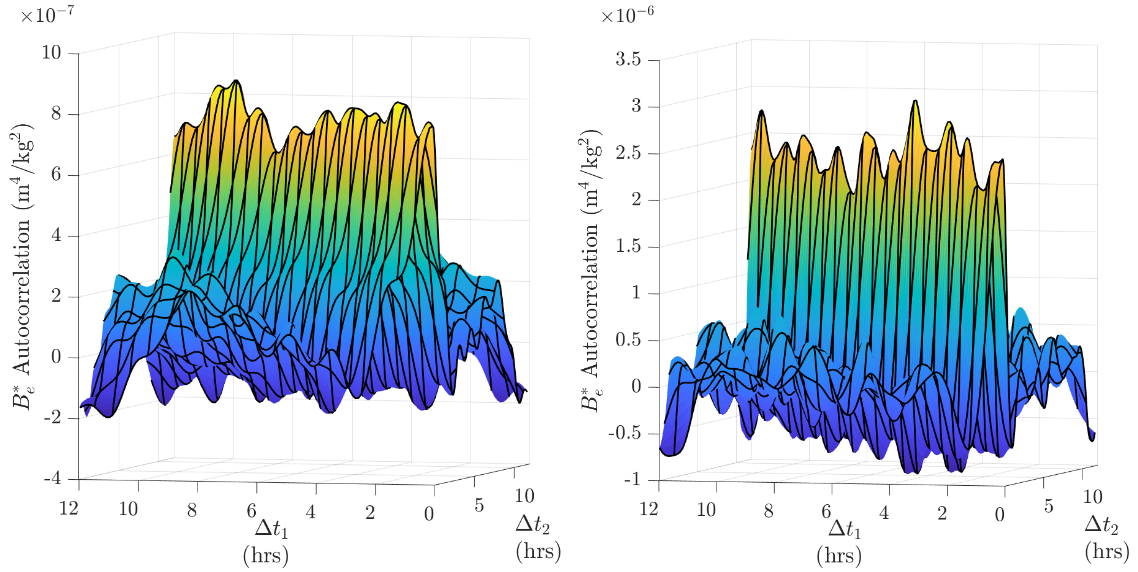

(a) $N_{\text{LS}} = 540$ (b) $N_{\text{LS}} = 360$

Figure 18. Three-Dimensional Correlation Surface of Estimated B_e^* Time Series

meeting the three criteria of a constant mean value function, finite correlation surface, and relatively constant correlation and covariance matrices.

With wide-sense stationarity established, ergodicity was then assessed. A practical way of assessing whether or not a process is ergodic is to see if a single realization of the process replicates the statistics of an ensemble. Figure 20 demonstrates this comparison for the B_e^* example processes by plotting the two-dimensional (possible for the ensemble due to the stationarity assertion justified above) autocorrelations together. Note the general, however imperfect, agreement between the two.

This agreement between the autocorrelation calculated from the ensemble and that calculated from the single realization can be improved by lengthening the duration of the single realization. In fact, ergodicity is only possible theoretically for an infinitely long, strict-sense stationary process [116, pg. 144]. This is obviously impossible in the real world, but it informs why a longer single realization strengthens the agreement between the two autocorrelation functions. Figure 21

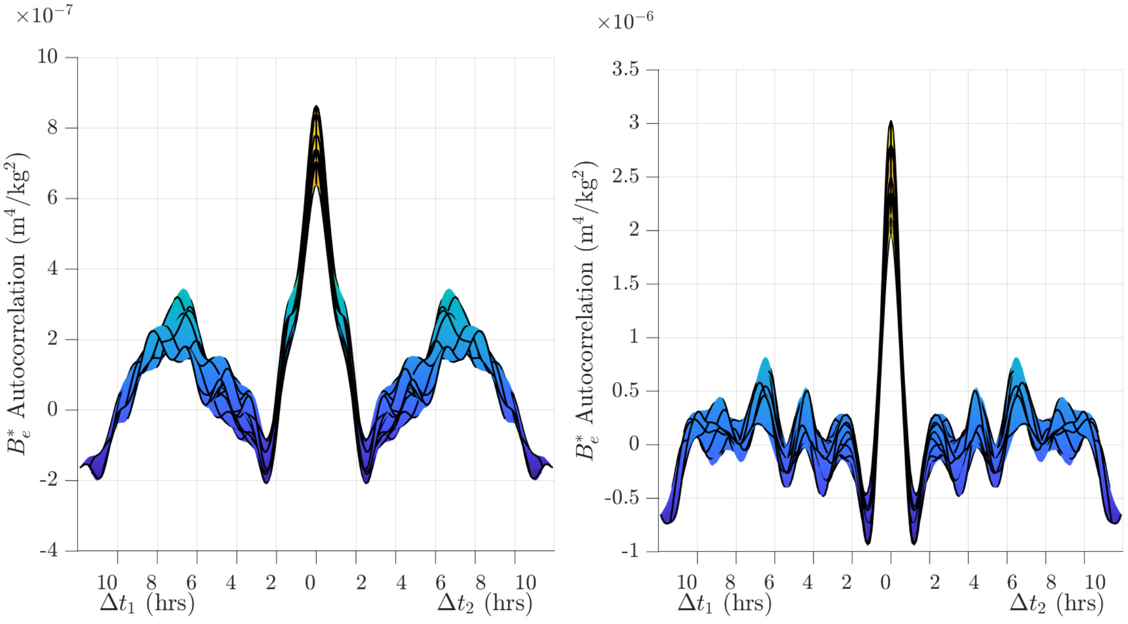

(a) $N_{\text{LS}} = 540$ (b) $N_{\text{LS}} = 360$

Figure 19. Three-Dimensional Correlation Surface of Estimated B_e^* Time Series, Rotated

demonstrates this effect by depicting ensembles calculated from within the interval of 1 Jun–31 Aug 2001 against single realizations calculated over that entire time period (which are much longer than the 7-day single realizations used above).

Assessing the ergodicity of the B_e^* time series, as much as practical, was key because a single realization is the type of data that is readily calculable from observational data, particularly on-board a satellite. Single realizations of B^* values were also used to characterize the random processes used in the stochastic propagation methods of the next chapter.

The results detailed above demonstrate that there was evidence for justifying an ergodic assumption for the B_e^* random processes, and that longer single realizations make this assumption more robust. However, the 7-day long realizations did show general agreement with the ensemble case, are likely more applicable to potential real-world implementations of the methods here discussed, and are more computationally efficient. Therefore, 7-day long realizations were used through-

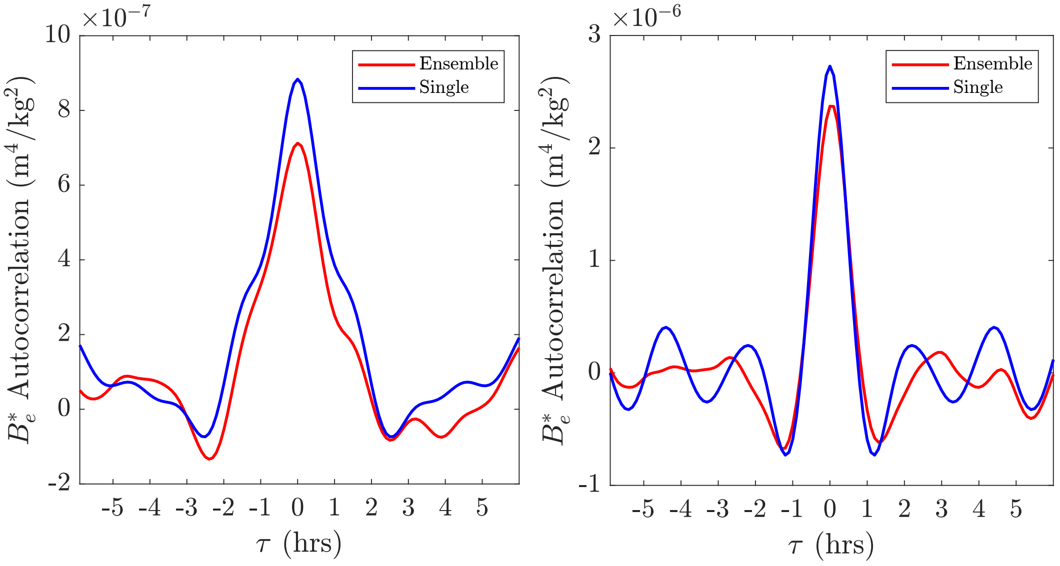

(a) $N_{\text{LS}} = 540$ (b) $N_{\text{LS}} = 360$

Figure 20. Two-Dimensional Autocorrelation Function of Estimated B_e^* Time Series, Ensemble and Single Realization

out the remainder of this research.

There is another way to consider the ensembles of B_e^* being here discussed. Up to now the ensembles have been considered as time series—as random processes. They can instead be considered as a collection of random variables where each random variable consists of the estimated values of B_e^* at a specific Δt. In this case, each random variable consists of 300 samples and can be subjected to probabilistic tests to determine its nature, specifically whether or not it is a Gaussian random variable to assess the applicability of Gaussian process models.

Figure 22 is a quantile-quantile plot of a B_e^* random variable against an appropriately scaled and shifted normal distribution. If B_e^* ensembles were exactly distributed as a Gaussian random variable, the blue markers would perfectly align with the red reference line. Such perfect agreement is not seen in Figure 22, however the fit is quite close, particularly in the middle quantiles (most of the deviation appears to be in the tails of the distribution). Figure 23 shows the ensemble of nor-

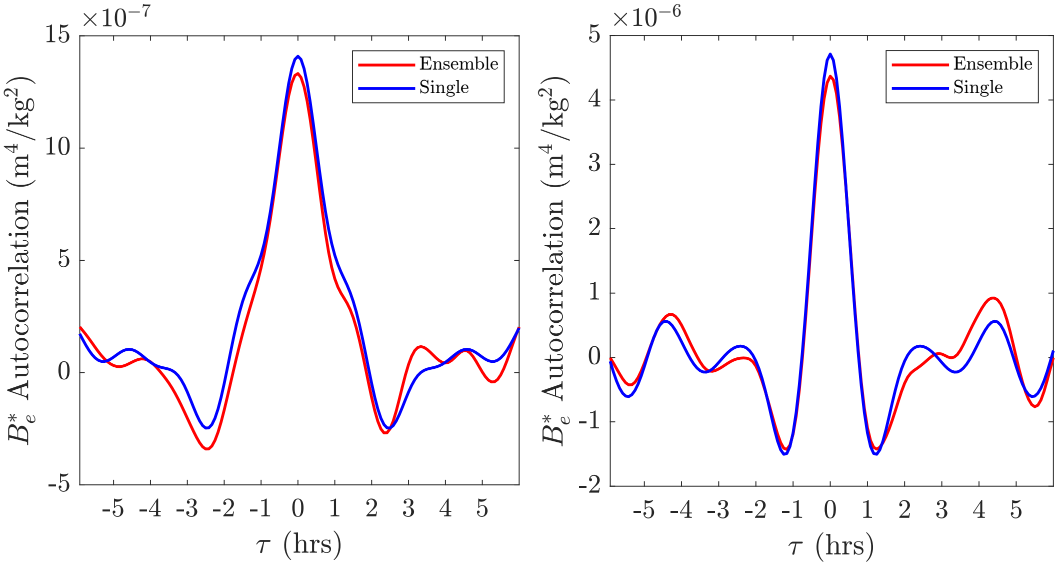

(a) $N_{\mathrm{LS}} = 540$ (b) $N_{\mathrm{LS}} = 360$

Figure 21. Two-Dimensional Autocorrelation Function of Estimated B_e^* Time Series, Ensemble and Long Single Realization

malized B_e^* random variables' cumulative density functions (CDFs) plotted against the standard normal distribution. Once again the alignment is not perfect, however in both the quantile-quantile plot and CDF comparisons the B_e^* ensembles appear to be roughly normal. While certainly subjective, this analysis provides some justification for assuming that B^* random variables are Gaussian, and that assumption was made for this research.

The final two steps required in this analysis of B^* as a random process were parameterization via Equations 50, 42, and 45 and the generation of realizations via Equation 51. A demonstration of the success of both techniques, applied to the random process calculated above, is shown in Figure 24 which depicts the calculated empirical autocorrelation of the B_e^* time series along with the parameterization and the autocorrelation of a generated ensemble. The relatively close agreement, particularly through the first cycle either side of $\tau = 0$ demonstrates that the B_e^* time series can be *approximated* as a SOGM random process and that samples of a

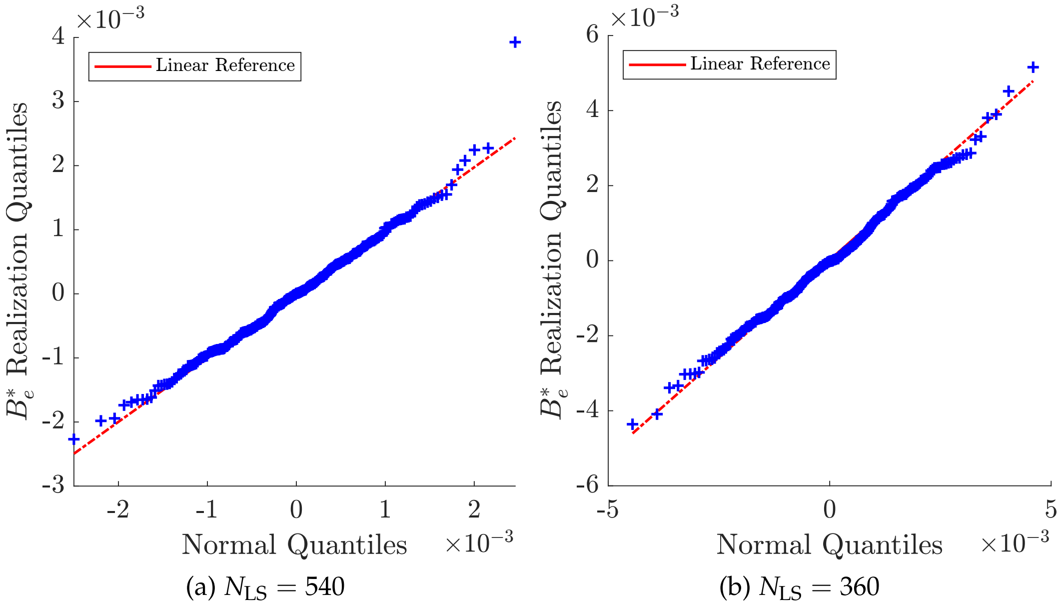

(a) $N_{\text{LS}} = 540$ (b) $N_{\text{LS}} = 360$

Figure 22. Quantile-Quantile Plots of B_e^* Random Variables and a Scaled and Shifted Normal Distribution

like random process can be generated for use in later Monte Carlo analysis. Also note that the agreement between the mathematical SOGM model and the empirical autocorrelation is better for $N_{\text{LS}} = 360$ than for $N_{\text{LS}} = 540$. It was noted that, in general, as N_{LS} increases the autocorrelation functions resemble the SOGM model less and less, indicating that for larger choices of N_{LS} an alternative random process model may be required. However, at $N_{\text{LS}} = 540$ (as used in this research), the SOGM model remained useful and capable of producing the results of the next chapter.

Finally, it should be re-emphasized that applying any mathematical process model to empirical data is an approximation. Noting that, the SOGM process model used here is a fit for the portion of the B_e^* autocorrelation functions which correspond to the time window of available estimation data, and was chosen as the best option available for parameterizing and generating realizations of the process for the stochastic prediction methods discussed in the next chapter.

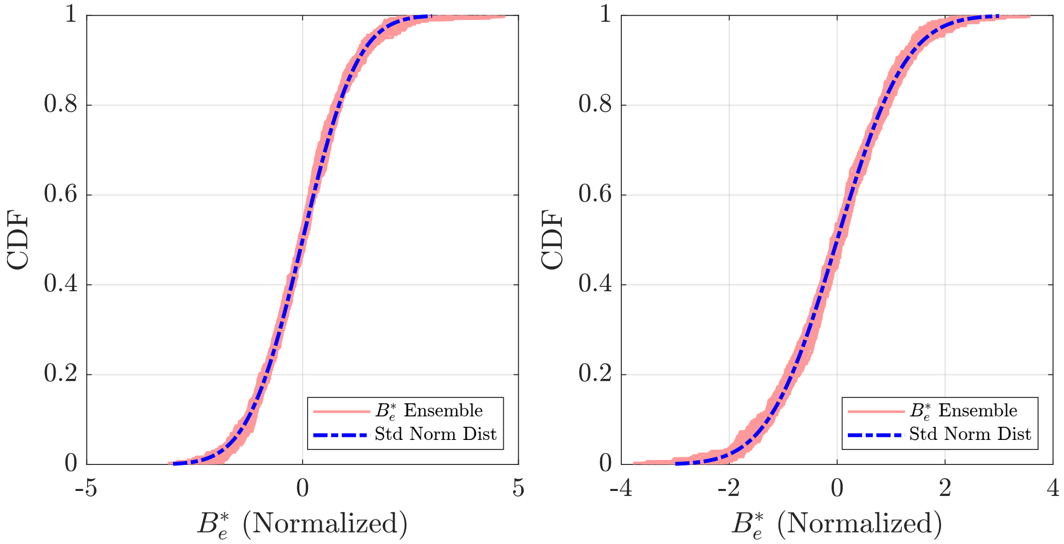

(a) $N_{\mathrm{LS}} = 540$ (b) $N_{\mathrm{LS}} = 360$

Figure 23. Cumulative Distribution Functions of Normalized B_e^* Random Variables and the Standard Normal Distribution

5.3 Conclusions

The results above demonstrate, chiefly, that time series of B^* estimates can be modeled and parameterized as a random process. While the analysis is not without the usual caveats and assumptions that accompany the analysis of empirical data, the B_e^* random processes analyzed were found to be both stationary and ergodic. Additionally, the B_e^* ensembles were found to be roughly distributed as Gaussian random variables. Coupled with a Markov assumption and the noted oscillations in calculated autocorrelation functions, this Gaussian property suggested modeling the B_e^* random processes as second-order Gauss-Markov processes.

Results further demonstrated that the parameters of the modeled random process could be used to generate realizations of B_e^* random processes which mimic their empirical counterparts. It was therefore shown to be possible that, from observational data only, the B_e^* random process can be calculated empirically, parameterized, and generated, confirming Research Hypothesis 2.

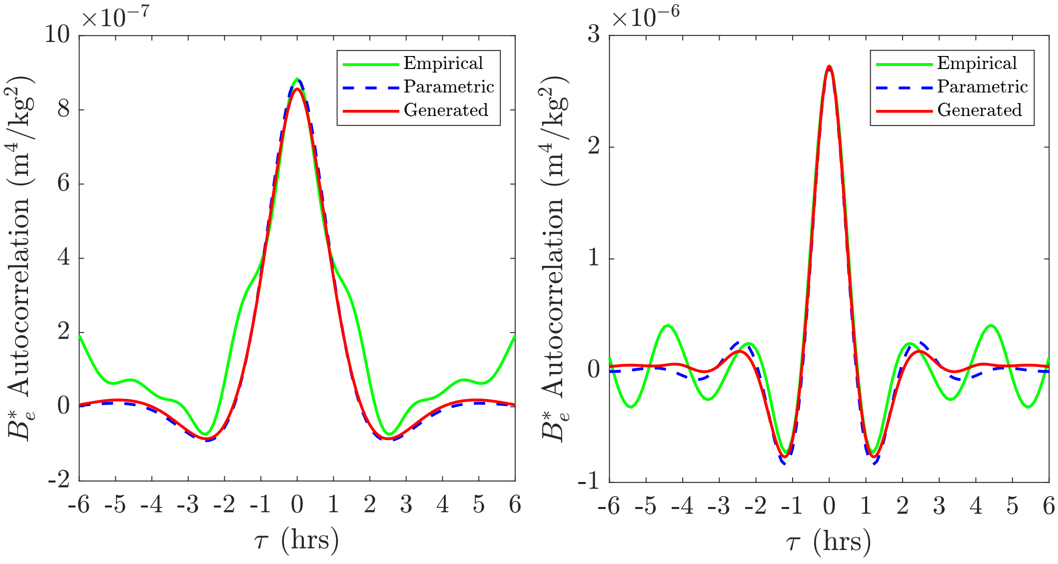

(a) $N_{\mathrm{LS}} = 540$ (b) $N_{\mathrm{LS}} = 360$

Figure 24. Autocorrelation Functions of Empirical, Parameterized, and Generated B_e^* Random Processes

VI. Stochastic Orbit Prediction

The culminating hypothesis of this research is that modeling the prediction uncertainty caused by air drag using B^* as the only random air drag variable can serve as the basis of a stochastic prediction method, and that the method will be capable of realistically characterizing its modeling uncertainty without restricting the choice of atmospheric density model or the dynamics formulation (Research Hypothesis 3).

This chapter presents research addressing this hypothesis using new developments and the results of the previous two chapters. The next section discusses the stochastic prediction of LEO satellite orbits using Monte Carlo (MC) simulation, and the following section presents the results of using Unscented Transform prediction (essentially the propagate steps of an Unscented Kalman Filter (UKF)) to achieve a stochastic prediction model capable of realistic uncertainty characterizations. These two sections represent the accomplishment of Research Tasks 4 and 5. The chapter concludes with brief sections on other potential methods of stochastic propagation and the potential applicability of this paradigm to on-board stochastic prediction.

6.1 Monte Carlo Simulation

The principal utility of MC simulation is that fully non-linear, stochastic dynamics (such as those under consideration in this research) can be effectively modeled. Each realization of a MC simulation ensemble is a single realization of the system's stochastic dynamics, and the distribution formed from a collection of N_{MC} realizations approaches the true distribution as N_{MC} becomes large via the Law of Large Numbers [115, pg. 233]. An additional benefit is that no simplifying assumptions need to be applied to the dynamical system to use MC simulation—as longs as the system can be dynamically propagated and any embedded random processes can be generated, MC simulation can be used. Specifically, MC simulation was used in this research for two purposes.

The first was to validate the stochastic representation of B^* and B_e^* discussed in the preceding chapter—namely to verify that the uncertainty of stochastic predictions made using the SOGM characterization of B^* agreed with the empirical uncertainty for a similar prediction model. The comparison of empirical uncertainty to uncertainty characterizations derived from MC simulation isn't a perfect one, which will be discussed later in further detail, however it was useful evidence that the MC model's uncertainty (and therefore the underlying stochastics of the B_e^* random process) coincided with the best available depiction of the prediction model's true uncertainty.

The second purpose was that once the MC simulation had been validated via comparison to the empirical results, MC simulation then served as a validation model for other stochastic propagation methods. This is leveraged later in this chapter when MC simulation is compared to the results of stochastic prediction via the Unscented Transform. Note, however, that MC is not generally suitable as a stochastic prediction method itself for the purposes of this research, as the desire is for a stochastic prediction method that does not require the large number of realizations that MC simulation does, chiefly for reasons of speed.

6.1.1 Methodology

Monte Carlo simulation began with a mean initial conditions vector $\overline{\boldsymbol{X}}(t_0)$ and the associated uncertainty of those initial conditions, in this case a covariance matrix $P_{\boldsymbol{X}}(t_0)$ as the initial uncertainty distribution was assumed to be Gaussian as discussed previously. Then, for each realization $i \in \{1, \ldots, N_{\text{MC}}\}$ perturbed initial conditions were obtained via random sampling of a multi-variate normal distribution using Equation 56

$$\boldsymbol{X}_i(t_0) = \overline{\boldsymbol{X}}(t_0) + \text{mvn}\left(0, P_{\boldsymbol{X}}(t_0)\right) = \overline{\boldsymbol{X}}(t_0) + \boldsymbol{X}_{\text{pert},i} \tag{56}$$

where $\text{mvn}\left(\boldsymbol{m}, P\right)$ is a function which draws a single $N_{\text{MC}} \times 1$ sample vector from the multi-variate normal distribution with mean vector $\boldsymbol{m}$ and covariance matrix P (the definition of the intermediate perturbation vector $\boldsymbol{X}_{\text{pert},i} = \text{mvn}\left(0, P_{\boldsymbol{X}}(t_0)\right)$ will be useful below). As N_{MC} becomes large, the MC ensemble's initial conditions will tend to be distributed according to the supplied initial mean and covariance, per Equation 57.

$$\boldsymbol{X}(t_0) \sim N(\overline{\boldsymbol{X}}(t_0), P_{\boldsymbol{X}}(t_0)) \tag{57}$$

Each realization's initial conditions were then propagated through the system's full, non-linear, stochastic dynamics (discussed below), and the resultant ensemble of final points was then a random variable whose distribution converged to the model's true prediction uncertainty distribution (if N_{MC} is large).

Obtaining estimates of the initial mean position and velocity and their associated covariance matrix for MC simulation required a combination of least squares estimation and B_e^* time series analyses as described in the previous chapter. Least-squares estimation was performed for each MC realization using the deterministic dynamics models detailed in Section 3.1, which yielded estimates of the mean position and velocity and their covariance. However, instead of the usual estimate covariance calculated using the algorithm in Appendix B, the position and velocity covariance returned by the least squares algorithm was modified for MC to be the covariance of the position and velocity *residuals* of the final propagation run within the least squares algorithm.

The conceptual reason for doing this is that the initial covariance of the MC ensemble should represent the uncertainty of the MC initial conditions with respect to the "truth" because this is the best available representation of initial prediction uncertainty, and in this case the "truth" is represented by the observational data. Since the residuals calculated within the least squares algorithm are an ensemble of error vectors between the model's expected state and the state given by observational data, it was assumed that the distribution of these residuals was a decent approximation of the distribution of the true error at t_0, and hence of $P_{\mathbf{X}}(t_0)$. However, the covariance normally returned by the least squares algorithm as described in Appendix B is not at all dependent on the residuals [2, pg. 73], and thus the covariance of the residuals was used instead. Practically, the original covariance returned by the original least squares algorithm turned out to be orders of magnitude too small, and using the covariance of the residuals resulted in much closer agreement between the initial MC covariance and the initial empirical covariance calculated using the methodology of Chapter IV. Using the covariance of the residuals in this manner is a simplified solution to the notoriously difficult problem of estimating true covariance matrices from observational data, and Vanli and Taylor [152] note that this method generally underestimates the covariances. While there is a wide body of research into alternative methods of estimating this type of covariance, a survey of which is provided by Duník et al. [153], the method of using the covariance of the residuals was used in this research.

The coordinate frame in which the residuals were resolved was critical to the effectiveness of this procedure. Because the residuals were calculated at various points in the satellite's orbit during least squares estimation, leaving the residuals in the inertial $\{x, y, z\}$ representation made little sense as these directions are not consistent throughout the least squares algorithm. Instead, residuals were resolved in the RTN coordinate frame (which is satellite-centric), and the resulting covariance was therefore also based in RTN coordinates.

The initial mean value of the ballistic coefficient and its variance were obtained for each MC simulation using the random process analysis method described in the previous chapter. This random process analysis also yielded the parameters of the B_e^* random process necessary to simulation realizations for use in the Monte Carlo simulation (in Monte Carlo simulation the deterministic B^* of the SP A and SP B models is replaced by simulated realizations of B^* random processes, which is discussed in more detail below).

Ultimately, the state of the MC initial conditions after the least squares estimation is given by

$$\overline{\boldsymbol{X}}(t_0) = \begin{bmatrix} \boldsymbol{r}_{\text{est}} \\ \boldsymbol{v}_{\text{est}} \\ \overline{B^*} \end{bmatrix} \tag{58}$$

$$P_{\boldsymbol{X}}(t_0) = \begin{bmatrix} P_{\text{resid,RTN}} & \mathbf{0}\ (6 \times 1) \\ \mathbf{0}\ (1 \times 6) & \sigma_{B^*}^2 \end{bmatrix} \tag{59}$$

where $\boldsymbol{r}_{\text{est}}$ and $\boldsymbol{v}_{\text{est}}$ are the position and velocity estimates returned by least squares in inertial coordinates, $P_{\text{resid,RTN}}$ is the 6×6 covariance matrix of the least squares residuals resolved in the RTN frame, and $\overline{B^*}$ and $\sigma_{B^*}^2$ are the mean and variance of the calculated B_e^* SOGM process. Note that this method necessarily removes any statistical dependence between B^* and the position and velocity (the final row and column of $P_{\boldsymbol{X}}(t_0)$ are zeros except for the diagonal element) because the residuals contain position and velocity information only. The B_e^* random process analysis of the previous chapter was used to obtain the values relating to B^*, meaning that a

B^* time series was calculated and analyzed as a SOGM RP. Then $\overline{B^*}$ was set to the mean of the calculated B^* time series and $\sigma^2_{B^*}$ was set to the variance of the SOGM process (which coincides with the variance of the time series).

Note that because the residuals covariance matrices were in the RTN frame, an intermediate step was required when computing $\boldsymbol{X}_{\text{pert},i}$ in Equation 56. The perturbing vector was first sampled using the covariance matrix in RTN coordinates, and the position and velocity components were then converted back to inertial coordinates before being applied to the mean. Since the construction of $P_{\boldsymbol{X}}(t_0)$ removed any cross-correlation between B^* and the position or velocity, this procedure did not affect the B^* perturbation, which was carried through unchanged.

Additionally, note that full-state (position and velocity) measurements were used for least squares estimation in this research because the data was available, both in the post-processed CHAMP and GRACE-A/B science orbits and in the SOS data. Position-only measurements (or another type of measurement altogether, such as radar or optical) could also readily be used by modifying the H matrix in Equation 117 in Appendix B. Throughout this research results were found to be much more sensitive to changes in positional data than to velocity, which implies that the velocity data did not contribute much to the least squares estimates and gives confidence that the methods herein would remain effective if position-only data was used.

The dynamics for MC simulation were the same as the deterministic dynamics described in Section 3.1, except that for each MC realization a SOGM process realization based on the parameterized B^*_e analysis and with an initial B^*_0 value as perturbed from the random sampling described above was propagated in parallel to the MC realization. The SOGM process was propagated using a fourth-order Runge-Kutta propagator and Equation 51, where w was sampled from the standard normal distribution and scaled by dividing by the square root of the SOGM Δt. The B^* value in use by the MC was updated at each SOGM time step to reflect to the current value of the SOGM realization. Trial and error revealed that a SOGM time step of $\Delta t_{\text{SOGM}} = 5\,\text{min}$ was quite effective for this method of generating realizations.

Each realization of the MC simulation was propagated from its unique perturbed initial condition using this hybrid method. The benefit of applying the B_e^* SOGM in parallel with an otherwise deterministic prediction was that the MC simulation could utilize the exact same dynamics formulation (and even code) as the deterministic propagation used for empirical analysis. This was both convenient and ensured comparability of empirical and MC results, at least from a dynamics perspective. A visual representation of this MC simulation method is given in Figure 25.

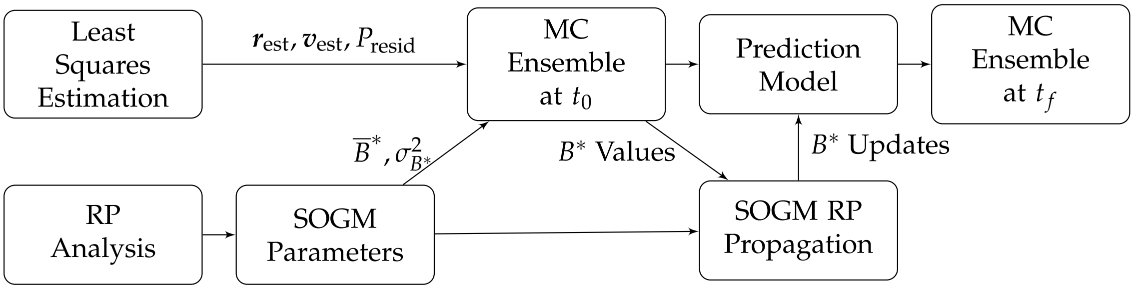

Figure 25. Monte Carlo Simulation Process Overview

6.1.2 Results

The first purpose of MC simulation stated above was to verify that the uncertainty characterizations of a stochastic prediction founded on the SOGM characterization of B^* agreed with the empirically calculated covariance matrices. Before discussing the results of this comparison, it is important to note that comparisons between empirical covariance matrices calculated using the method described in

Chapter IV and the MC simulation described above are not direct comparisons, as the two methods are fundamentally different. The empirical covariance analyses generated ensembles of prediction errors by randomly sampling initial times from a time interval and performing a single prediction for each one. Therefore, the empirical ensembles are ensembles of *unique* predictions and the covariance matrices calculated from them represent the empirical modeling uncertainty in and around that time interval. In contrast, the ensembles generated by MC simulation represent a large number of realizations of the *same* prediction from a single initial time, and the resultant mean of the MC ensemble is akin to what would be a single realization within the empirical ensemble. The covariance of the MC simulation (a single prediction) is not directly comparable to the empirical covariance which is based on many predictions—they are different things.

However, because the MC simulations were calculated with the same prediction models as the empirical covariance analyses (SP A and SP B) and the empirical prediction covariance matrices represent the models' prediction uncertainty, the resultant MC covariance matrices should be close to the empirical results because the MC results converge to the true model uncertainty for large N_{MC}. In other words, general agreement between the results of the empirical covariance analyses and MC simulation *is* expected (provided the results are for the same scenario and prediction model)—but this is not because the two types of results represent precisely the same thing.

Comparison between covariance matrices obtained via empirical analysis (EA) and MC simulation results for two example scenarios from Table 7 is first provided in Figure 26, which shows the growth of the in-track standard deviation ($\sigma_{22}(\Delta t) = +\sqrt{P_{22}(\Delta t)}$). Standard deviations are shown in Figure 26 instead of variances to provide unit agreement between the various types of figures in this chapter, and also because the curve fit analysis of Chapter IV (which was carried out in terms of the variance) was not necessary here.

Note the close agreement between the growth of the in-track standard deviation for EA and MC in Figure 26. This agreement indicates that the MC simulation as formulated per the preceding section results in realistic uncertainty in the in-track direction when compared to the empirical results.

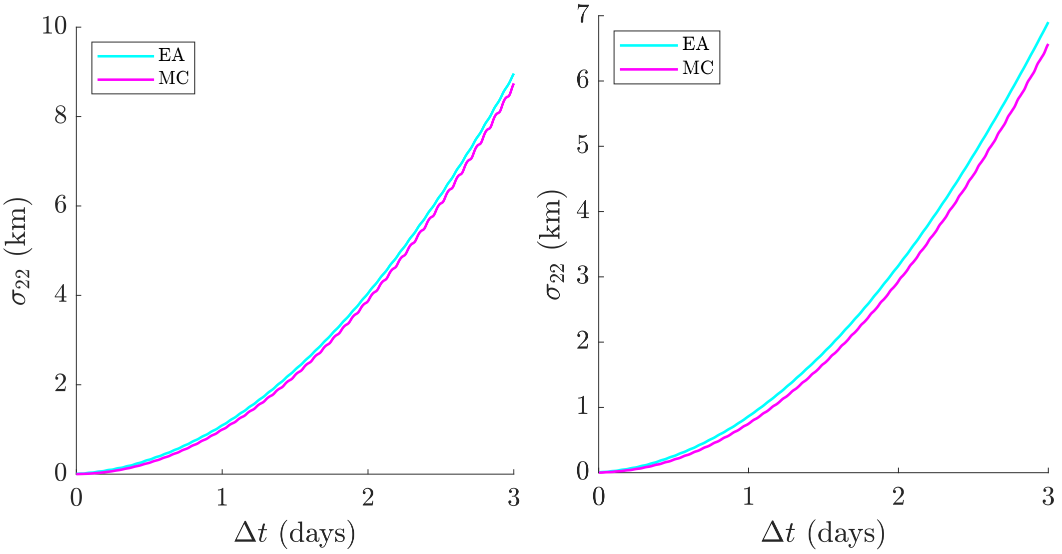

(a) CHAMP High Solar, SP A (b) GRACE-A Low Solar, SP B

Figure 26. In-track Uncertainty Growth for Empirical Analysis and Monte Carlo Simulation

The growth of the in-track uncertainty only considers one direction in the RTN coordinate frame, of course, and Figure 27 shows a more complete comparison by depicting the final ensembles and 1σ Gaussian error ellipses for the same example EA and MC scenarios for all two-dimensional combinations of the RTN principal directions.

The figures demonstrate that MC simulation results agree quite well with the EA results in both the radial and in-track directions, however there is an obvious disparity between the two in the normal direction. In the normal direction the MC uncertainty is at least an order of magnitude smaller than the EA results.

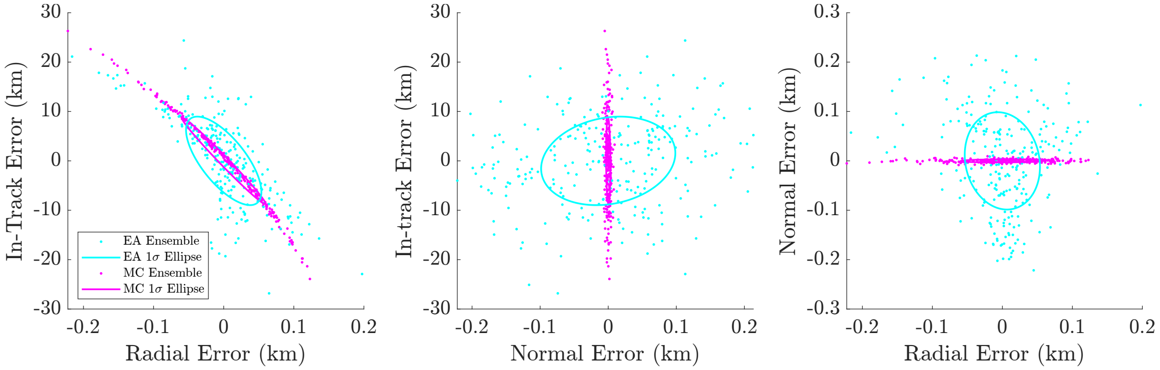

(a) CHAMP High Solar, SP A

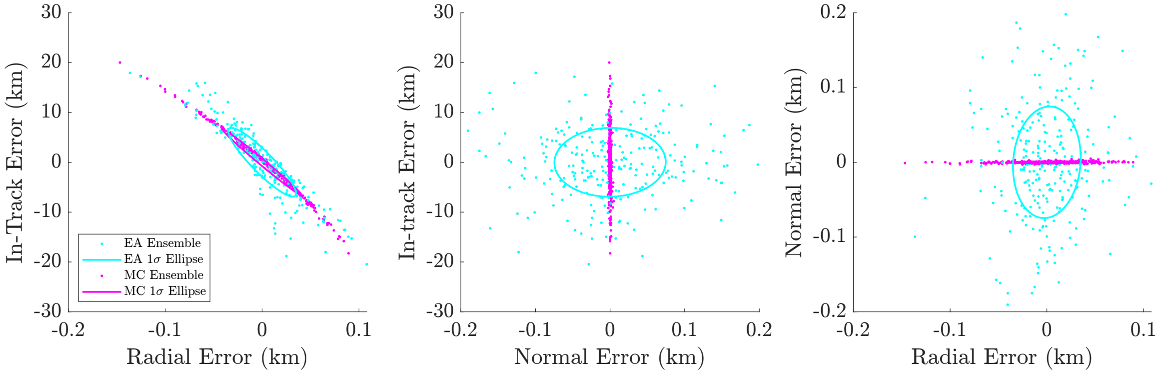

(b) GRACE-A Low Solar, SP B

Figure 27. Empirical Analysis and Monte Carlo Simulation Prediction Error Ensembles at t_f

One possible reason for this disparity is related to the fundamental difference between EA and MC discussed above and the fact that all satellites for which the EA analysis is available inhabited highly inclined orbits. Recalling that empirical analyses were computed from ensembles of predictions from within a time interval of an entire month (see Table 7), recognize that the Moon will have completed roughly an entire orbit around the Earth in that time span. Therefore, the predictions which make up the EA ensemble commit *unique* errors by omitting the Moon's gravitation because the Moon is in a variety of positions. Contrast this with the MC analyses which represent a single prediction such that every realization within the MC ensemble commits essentially the *same* error by ignoring the Moon's gravitation.

For the purpose of demonstration, consider the simplified case of a circular, polar satellite orbit around a spherical Earth with the Moon's orbit co-planar with the Earth's equator, as depicted in Figure 28 where $\boldsymbol{r}_{\text{moon}}$ is the vector from the Earth to the Moon, and $\{\hat{\boldsymbol{R}}_A, \hat{\boldsymbol{T}}_A, \hat{\boldsymbol{N}}_A\}$ and $\{\hat{\boldsymbol{R}}_B, \hat{\boldsymbol{T}}_B, \hat{\boldsymbol{N}}_B\}$ are RTN position vectors to example satellite locations A and B. Notice that in cases where the satellite's orbit plane is more perpendicular to $\boldsymbol{r}_{\text{moon}}$, the normal direction of the RTN frame doesn't change its orientation with respect to $\boldsymbol{r}_{\text{moon}}$ much as the satellite completes its orbit. Also note that in this perpendicular case the radial and in-track directions are perpendicular to $\boldsymbol{r}_{\text{moon}}$. These observations imply that when the orbit plane is more perpendicular to the moon vector the effect of the Moon's gravity is predominantly in the normal direction while its effect on the radial and transverse directions tends to zero. In the parallel case, however, it is the normal direction for which the effect of the Moon's gravity tends to zero, and the radial and transverse directions will notice oscillatory effects of the Moon's gravity as the satellite completes each orbit. This implies that in the parallel case the effect of the moon tends to cancel out in the radial and transverse direction over many orbits.

Considering both cases together, the normal direction is the direction of the RTN frame which experiences the most bias due to the effect of the Moon's gravity, meaning that as the orbit plane becomes more perpendicular to the moon direction the gravitational effect in the normal direction doesn't tend to cancel out due to oscillations or tend to zero. This demonstration is an oversimplification, as of course the angle between the orbit plane and the moon direction "rotates" in a sense through all available angles, however this illustrates a potential reason why the uncertainty of the EA analyses is so much greater in the normal direction specifically than the MC simulations.

The reasoning above implies that the increased uncertainty shown in the nor-

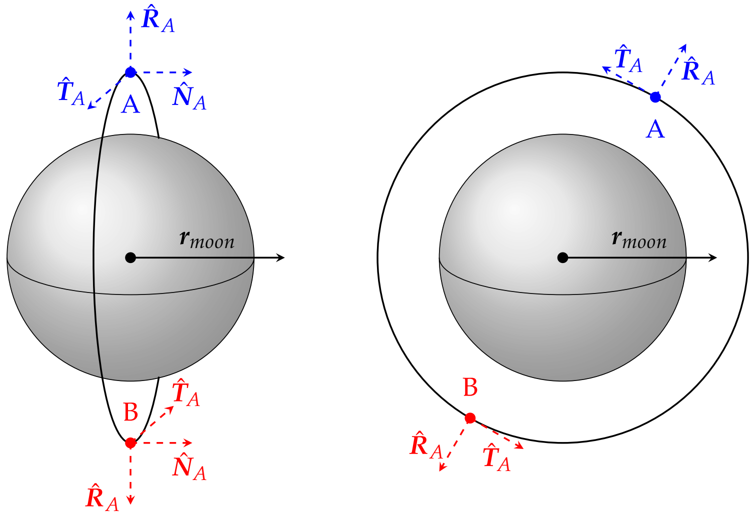

Perpendicular **Parallel**

Figure 28. Simplified Demonstration of Orbit Plane and Moon Vector Alignments

mal direction for EA may be an artifact of the method by which EA covariance matrices are calculated. The empirical analyses use ensembles with a variety of initial times as that is the only way of obtaining sufficient numbers of different propagations to enable calculation of a covariance matrix, however this method means that each prediction takes place in a unique dynamical environment. This is not true in the case of MC simulation. Controlling for this change in environment can be accomplished by including the effect of lunar gravity within the SP dynamics models (see Appendix C for details on how third-body gravitational perturbations were incorporated into the dynamics formulated in Section 3.1).

The effect of including lunar gravity is demonstrated in Figure 29a. Note that the uncertainty of the EA results in the normal direction was nearly halved by controlling for lunar gravity, indicating that the effect described above does cause some erroneous uncertainty in the normal direction if lunar gravity is not accounted for in the dynamics model. Incorporating solar gravity into the dynamics model along with lunar gravity results in an additional decrease in EA normal direction uncertainty, as shown in Figure 29b, for the same reasons as discussed above.

Final values for the radial, transverse, and normal 1σ uncertainty of the three configurations are Tabulated in Table 9. Note that including third body gravity perturbations has no perceptible effect on the MC analysis because every ensemble of the MC analysis experiences essentially the same dynamical environment with respect to the location of the moon and sun across the realizations—the differences between the MC realizations are tiny compared to the movement of the moon and sun throughout a time span of empirical analysis. Finally, these results demonstrate that the effect of third body gravity perturbations effect the normal direction for EA almost exclusively, as asserted above.

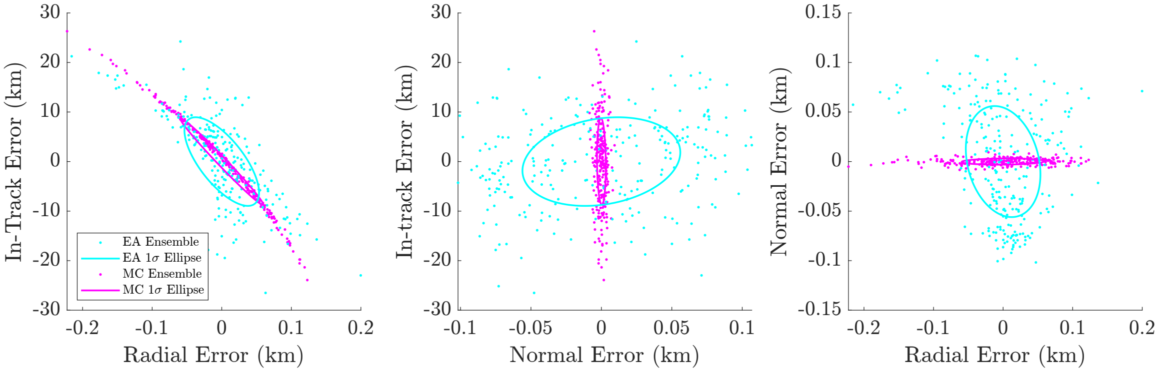

(a) Lunar Gravity Considered

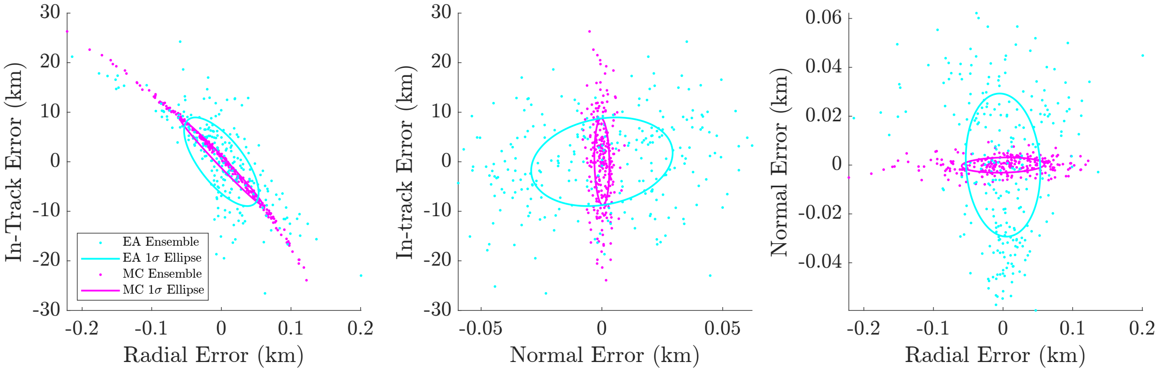

(b) Lunar and Solar Gravity Considered

Figure 29. Effect of Lunar and Solar Gravity on Empirical Analysis and Monte Carlo Results at t_f, CHAMP High Solar

Table 9. Uncertainty of Empirical Analysis and Monte Carlo Predictions for Various Third-Body Gravitational Perturbations

Gravity Modeled	σ_R (m) EA	σ_R (m) MC	σ_T (m) EA	σ_T (m) MC	σ_N (m) EA	σ_N (m) MC
Earth Only	53.8	59.6	8964	8743	98.6	3.12
Earth, Moon	53.6	59.6	8944	8743	56.0	3.12
Earth, Moon, Sun	53.5	59.4	8944	8743	29.3	3.12

Though controlling for the effect of third body gravity perturbations does help, the disparity in the normal direction between EA and MC results remains evident, indicating that there are additional error artifacts caused by the method of EA analysis or that there is some physical phenomenon at work in the normal direction which is ignored by the SP models (solar radiation pressure or an effect related to the relative velocity of the satellite with respect to the atmosphere, potentially). Importantly, the uncertainty in the normal direction is generally the smallest component, and the in-track direction is of more concern to this research as it is the direction impacted most by air drag and the motivation of this research. This agreement between MC simulation results and empirical results is a significant indicator of the uncertainty realism achieved by the stochastic formulation.

While the above results demonstrate the agreement of the MC and EA models in the radial and, more importantly, the in-track direction—it does not confirm the efficacy of the B_e^* random process model. To do that, a comparison was made between the predictions of MC simulation both with and without the effects of the B_e^* random process to ensure that the resultant covariance matrices are not simply the result of high-fidelity propagation of the initial uncertainty.

The results of this comparison are shown in Figures 30 and 31 for a single example scenario (CHAMP High Solar) and tabulated for all scenarios in Table 10. Figure 30a shows the covariance growth of MC simulation when initial values for B^* were perturbed using the variance of the B_e^* random process, but the random process was not applied dynamically ($\dot{B}^* = 0$ as in the deterministic case and no SOGM RP was used or propagated). Figure 30b demonstrates the fully stochastic case where initial values were perturbed *and* full realizations of the B_e^* random process were generated for MC simulation as in the above discussion. Figure 30c demonstrates the results of MC simulation if no B^* time series were available and initial B^* values were perturbed using the covariance matrix returned by the nominal least squares algorithm during the estimation of initial conditions. As an aside, note that these covariance matrices exhibit the same behaviors as those for the EA analysis—an overwhelming predominance of uncertainty growth occurs in the in-track direction. Lastly, the B^* ensembles generated for the two scenarios are included for demonstration as Figure 31, to illustrate the difference between the behavior of B^* when it was modeled deterministically ($\dot{B}^* = 0$) versus as a random process.

There are two key takeaways from Figure 30. First, calculating a time-series of B^* estimates is absolutely vital for the success of MC simulation, as the variance of that time series is necessary for perturbing the Monte Carlo initial conditions—simply using the covariance of the least squares estimate for B^* results in in-track uncertainty that is underestimated by at least two orders of magnitude. Second, the application of the dynamical SOGM random process has a significant effect on the resulting prediction, contributing approximately 15–20% of the in-track uncertainty as tabulated in Table 10. The table lists the final in-track variance $P_{22}(t_f)$ for all scenarios along with the percentage difference between the RP on and RP off cases. The significance of this is that applying the stochastics of B^* to the prediction model *dynamically* is key to achieving uncertainty realism.

Altogether, these results indicate that the uncertainty characterization provided by MC simulation which uses the B^* random process analysis as its stochastic

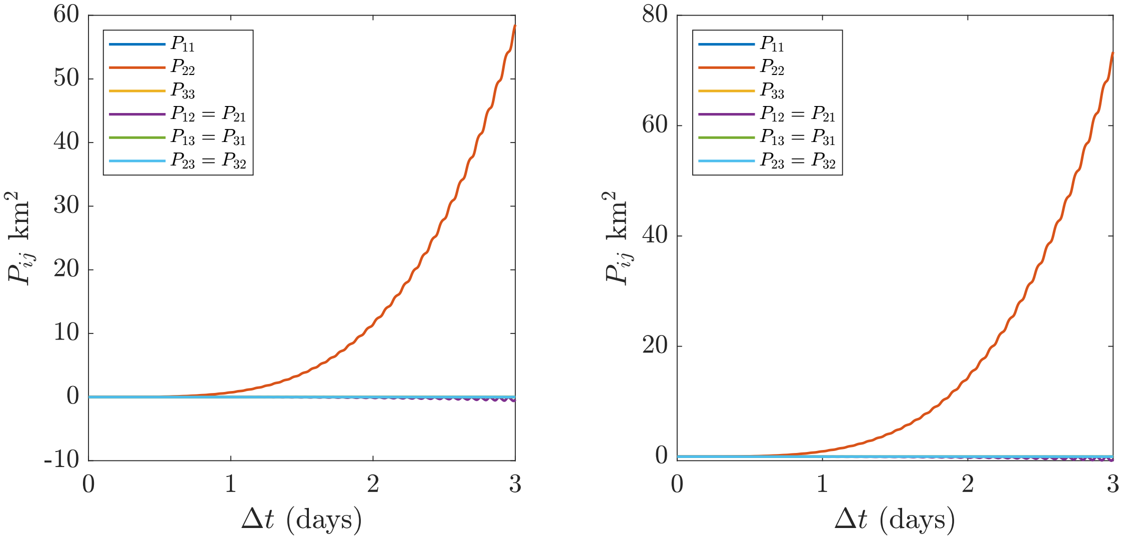

(a) RP Variance Used for Initial Perturbation, RP Not Applied

(b) RP Variance Used for Initial Perturbation, , RP Applied

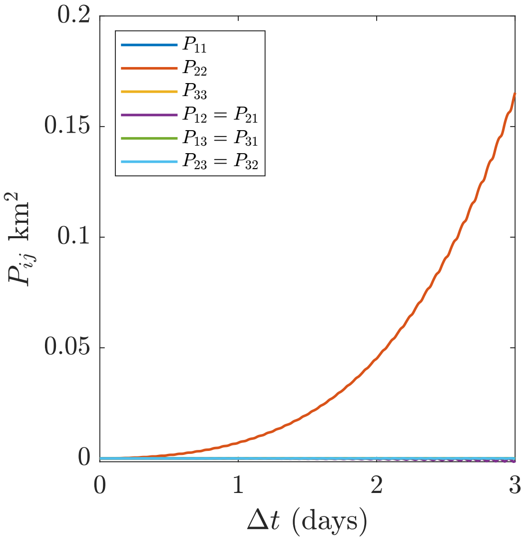

(c) Least Squares Variance Used for Initial Perturbation, RP Not Applied

Figure 30. Prediction Covariance Matrices for Three Configurations of the B_e^* Random Process, CHAMP High Solar

foundation agrees with empirical prediction uncertainty characterizations for the same model. In other words, the MC simulation achieves uncertainty realism using the best method of comparison available. This indicates that the paradigm investigated by this research (using B^* as the only random variable in a stochas-

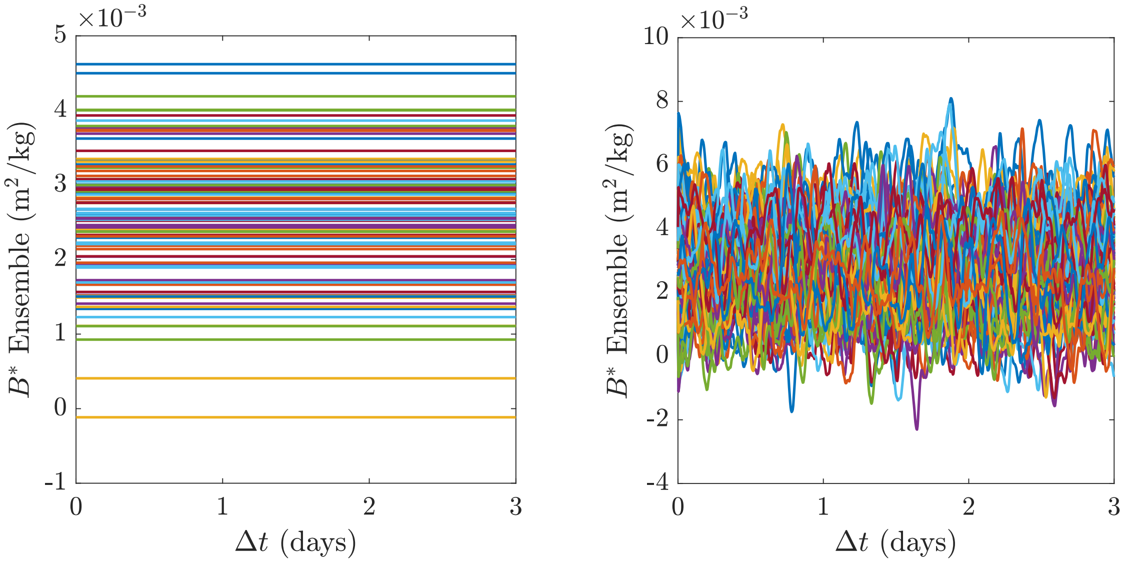

(a) RP Variance Used for Initial Perturbation, RP Not Applied

(b) RP Variance Used for Initial Perturbation, RP Applied

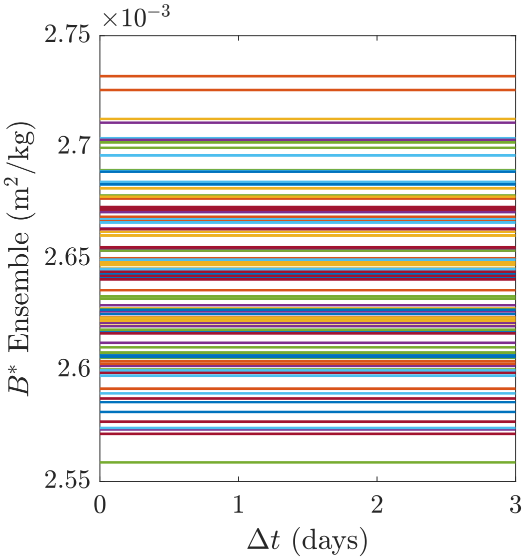

(c) Least Squares Variance Used for Initial Perturbation, RP Not Applied

Figure 31. $B_e^*(t)$ **Ensembles for Three Configurations of the** B_e^* **Random Process, CHAMP High Solar**

tic orbit predictor) is viable and confirms a key research hypothesis—that modeling B^* as a random process results in a stochastic orbit prediction method which achieves uncertainty realism.

Finally, note that the accuracy performance of the stochastic model obtained

Table 10. Comparison of B_e^* Random Process Implementations

Scenario	$P_{22}(t_f)$ (km^2) No RP	RP	Percent Difference (%)
CHAMP High Solar	58.5	73.4	20.3
CHAMP Low Solar	133	164	18.9
GRACE-A High Solar	92.3	111	16.8
GRACE-A Low Solar	35.6	42.6	16.4
GRACE-B High Solar	92.1	111	17.0
GRACE-B Low Solar	35.7	42.6	16.2
SOS Low Solar	356	422	15.6

via MC simulation is very similar to the accuracy of the deterministic model used for empirical covariance analysis. To demonstrate this, the average magnitude of the position and velocity error of the CHAMP High Solar is scenario is shown in Figure 32a for MC simulation and in Figure 32b for empirical analysis. This comparison demonstrates that adding the B^* stochastics to the model formulation does not significantly impact prediction accuracy. Therefore, the MC-based stochastic prediction not only achieves uncertainty realism, but also maintains prediction accuracy of the underlying dynamics model.

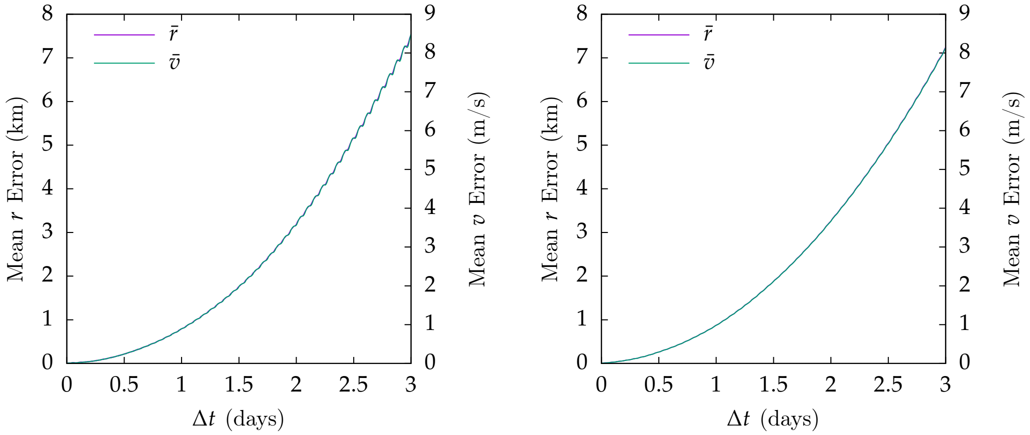

(a) MC Simulation (b) Empirical Analysis

Figure 32. Average Magnitude of Position r and Velocity v Errors, CHAMP High Solar, SP A

6.2 Stochastic Prediction Via the Unscented Transform

While the Monte Carlo simulation described in the preceding section is a stochastic prediction method utilizing the B_e^* SOGM formulation, the aim of this research is to produce such a model that does not require the large number of realizations required for MC simulation. This stochastic prediction model must also produce realistic characterizations of its own prediction uncertainty, which is the main thrust of this research.

This section details the development and performance of such a stochastic prediction model using the Unscented Transform (UT)—essentially the propagate steps of an Unscented Kalman Filter. The benefits of this method are that it is generally faster than MC simulation, does not require evaluation of the system Jacobian (the A matrix), and is generally capable of performing predictions for non-linear dynamics such as those of an orbiting satellite. The main drawback when compared with MC simulation is the necessity of assuming all random variables are Gaussian, but that was an assumption already made with regard to this research and ways of avoiding it are discussed later in the chapter.

6.2.1 Methodology

The premise of using the Unscented Transform (UT) for the prediction of non-linear systems, as stated eloquently by Julier et al. in their seminal paper [71], is that "it should be easier to approximate a Gaussian distribution than it is to approximate an arbitrary nonlinear function". In the case of this research, the distribution of the model prediction error was assumed to be Gaussian, therefore rather than trying to approximate the satellite's very non-linear dynamics (as must be done in an Extended Kalman Filter, for example) the method used the non-linear dynamics and relied on the Unscented Transform (UT) to obtain the statistics of the Gaussian distribution after propagation through the non-linear dynamics.

In a stochastic prediction model, the system state vector at some time step k is actually a random variable $\boldsymbol{X}(k)$ (assumed to be Gaussian) with mean $\overline{\boldsymbol{X}}(k)$ and covariance $P_{\mathbf{X}}(k)$. The propagation of this initial random variable through the non-linear satellite dynamics to the next time-step $k+1$ represents a non-linear transformation to the posterior random variable $\boldsymbol{X}(k+1)$ with mean $\overline{\boldsymbol{X}}(k+1)$ and covariance $P_{\mathbf{X}}(k+1)$. To utilize the Unscented Transform (UT) and determine the statistics of the distribution at $k+1$, a selected set χ of $2n+1$ points was constructed that had the same mean and covariance as $\boldsymbol{X}(k)$, where n is the number of states in the system (7 in this case). (Note that this development used a discrete time formulation, hence time step indices like k rather than the continuous time variable t. Continuous time formulations are also available, such as that of Särkkä [154], however a discrete formulation was used here for reasons discussed below.)

The samples that make up this set χ are usually called "sigma points", and were selected according to Equations 60–64 [72]

$$\chi_0(k) = \overline{\mathbf{X}}(k) \tag{60}$$

$$\chi_i(k) = \overline{\mathbf{X}}(k) + \left(\sqrt{(n+\kappa)P_{\mathbf{X}}(k)}\right)_i \tag{61}$$

$$\chi_{i+n}(k) = \overline{\mathbf{X}}(k) - \left(\sqrt{(n+\kappa)P_{\mathbf{X}}(k)}\right)_i \tag{62}$$

$$W_0 = \frac{\kappa}{n+\kappa} \tag{63}$$

$$W_i = W_{i+n} = \frac{1}{2(n+\kappa)} \tag{64}$$

for $i = \{1, \ldots, n\}$ and where κ is a tuning parameter which controls the spread of the sigma points, $\sqrt{(n+\kappa)P_{\mathbf{X}}(k)}_i$ is the i-th column of the covariance matrix multiplied element-wise by $\sqrt{n+\kappa}$, and each W represents the weight of each respective sigma point which was used in weighted averaging schemes presented below. This method of selecting sigma points ensured that the set χ had the same mean, covariance, and odd-number higher moments as the random variable $\boldsymbol{X}(k)$ [72] and represented the mean and covariance "accurately to the 3rd order (Taylor series expansion) for *any* nonlinearity" [155].

After propagation through the system's dynamics, the mean and covariance of the transformed random variable $\boldsymbol{X}(k+1)$ were nominally obtained via the weighted sums in Equations 65 and 66.

$$\overline{\boldsymbol{X}}(k+1) = \sum_{i=0}^{2n} W_i \, \chi_i(k+1) \tag{65}$$

$$P_{\boldsymbol{X}}(k+1) = \sum_{i=0}^{2n} W_i \left[\left(\chi_i(k+1) - \overline{\boldsymbol{X}}(k+1) \right) \left(\chi_i(k+1) - \overline{\boldsymbol{X}}(k+1) \right) \right] \tag{66}$$

However, one common drawback of UKFs and prediction using the UT is numerical instability, particularly the possibility of the covariance matrix becoming non-positive, semidefinite at some point during the prediction. This is a common issue when approximating higher orders of probability distributions [72], and there are two main ways of remediating this. First, Julier notes that replacing the mean $\overline{\boldsymbol{X}}(k+1)$ in Equation 66 with χ_0 guarantees a positive definite covariance matrix [72]. Additionally, "square-root" versions of the UKF exist in which the square-root of the covariance matrix is only computed once at the initial step, not at every time step, therefore removing the necessity of a positive-definite covariance matrix [156]. The first method was used in this research, and the mean and covariance of the transformed random variable $\boldsymbol{X}(k+1)$ were actually obtained via Equations 67 and 68.

$$\overline{\mathbf{X}}(k+1) = \sum_{i=0}^{2n} W_i \, \chi_i(k+1) \tag{67}$$

$$P_{\mathbf{X}}(k+1) = \sum_{i=0}^{2n} W_i \left[\left(\chi_i(k+1) - \chi_0(k+1) \right) \left(\chi_i(k+1) - \chi_0(k+1) \right) \right] \tag{68}$$

To calculate each orbit prediction using the UT method, a B^* random process was calculated and parameterized and the initial mean and covariance were obtained using Equations 58 and 59. Then, initial sigma points $\chi(0)$ and constant weights W_i were calculated from the initial mean and covariance. Example initial sigma points are shown in Figure 33, which depicts the MC analysis initial ensemble and a 1σ Gaussian error ellipse, initial sigma points and a 1σ Gaussian error ellipse, and a 1σ Gaussian error ellipse constructed from the initial covariance matrix for the GRACE-A Low Solar scenario as an example (other scenarios had similar results). Note that both the MC and UKF 1σ ellipses match that of the initial covariance so well that they overlap almost perfectly, indicating that both stochastic models approximated the estimated initial uncertainty very well. The spread of the sigma points in the figure was controlled by the tuning parameter, which for this research was set to $\kappa = -6$. As $n = 7$ in this case, this means that the sigma points generated by Equations 61 and 62 were scaled by $\sqrt{n+\kappa} = 1$ standard deviation in each "direction". Choosing this value for κ was done via trial and error, seeking a value which produced reliable results without causing stability issues.

Each sigma point χ_i was then propagated through the system's dynamics, yielding the set of transformed sigma points at the next time-step $\chi(k+1)$. This propagation was accomplished by numerically integrating each sigma point from the time at time step k to the time at time step $k+1$, using the deterministic

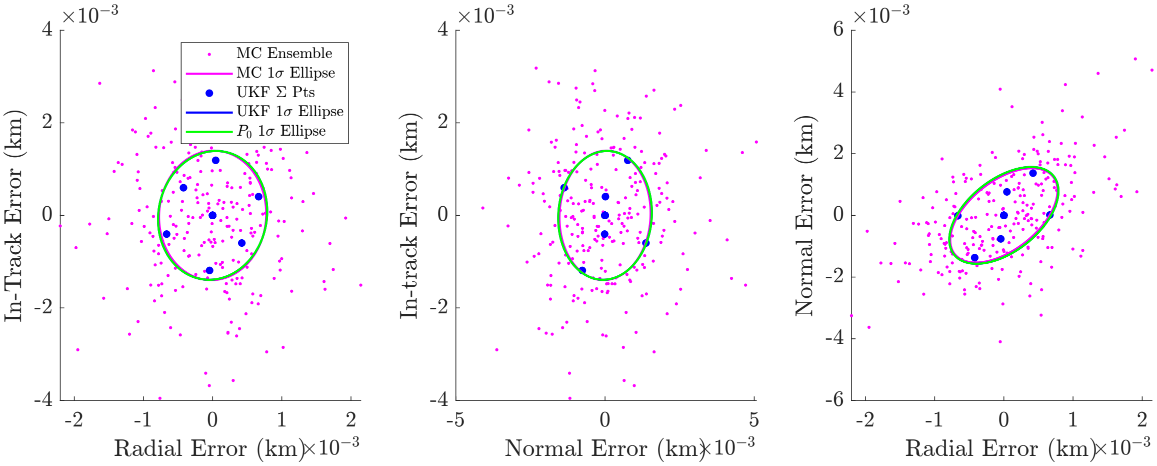

Figure 33. Initial Monte Carlo Ensemble and Unscented Transform Sigma Points Versus Initial Covariance, GRACE-A Low Solar

dynamics formulation developed in Chapter III (how this UT became stochastic is addressed below). High-fidelity numerical integration was used to avoid potential dynamical discretization errors.

Once the new sigma points $\chi(k+1)$ were available, the mean $\overline{\mathbf{X}}(k+1)$ and covariance $P_{\mathbf{X}}(k+1)$ were calculated per Equations 67 and 68. Then the effect of the B^* SOGM RP was added via a discretized process noise matrix Q_d, which was calculated using the parameters of the SOGM, the SOGM shaping filter in Equation 51, and a numerical calculation method developed by Van Loan [157][158, pg. 104]. The benefit of this method of incorporating the RP is that because the parameters of the SOGM shaping filter are time-invariant the resultant discretized noise Q_d is constant for equally spaced time steps and only needed to be computed once prior to executing the prediction. The incorporation of this process noise was accomplished simply by adding the value of Q_d to the last diagonal element of $P_{\mathbf{X}}(k+1)$, representing the additional uncertainty of B^* due to the RP.

While this method of incorporating the uncertainty caused by the B^* RP was a simplification in some sense, it proved sufficient to produce the results of the next section. A model utilizing a fully stochastic dynamics formulation wherein the two states of the B_e^* random process are elements of the state matrix may be an avenue of future research, however. Additionally, a later discussion will reveal that other stochastic propagation methods may better serve the cause of uncertainty realism, so this simplified yet effective method is presented here as demonstration of the viability of the overall research paradigm—that modeling B^* as a random process informed by observational data is an effective method of achieving uncertainty realism. The overall UT prediction algorithm is given in Algorithm 1, where N_k is the number of time steps to propagate.

Algorithm 1: Stochastic Prediction Using the Unscented Transform

```
Data: Initial mean $\overline{\mathbf{X}}(k=0)$, initial covariance $P_{\mathbf{X}}(k=0)$, tuning
      parameter $\kappa$, and $B^*$ SOGM parameters
Result: Mean and covariance of posterior distribution at discrete time steps
Calculate $W$s and $Q_d$
for $k$=0 to $N_k$ do
    Calculate $\chi(k)$ using $\overline{\mathbf{X}}(k)$ and $P_{\mathbf{X}}(k)$
    Propagate $\chi(k) \to \chi(k+1)$
    Calculate and store mean $\overline{\mathbf{X}}(k+1)$
    Calculate and store covariance $P_{\mathbf{X}}(k+1)$
    Add $Q_d$ to the last diagonal element ($B^*$) of $P_{\mathbf{X}}(k+1)$
end
Write outputs
```

6.2.2 Results

Stochastic predictions using the UT prediction method described in the preceding section were performed for all scenarios listed in Table 7. Example results showing the full covariance matrix growth produced by MC analysis and UT prediction for the CHAMP High Solar scenario are shown in Figure 34. Note that almost all uncertainty growth takes place in the in-track direction (P_{22}) for both MC and UT prediction, and also that the two results are nearly identical.

As in the MC simulation case in the preceding section, however, viewing re-

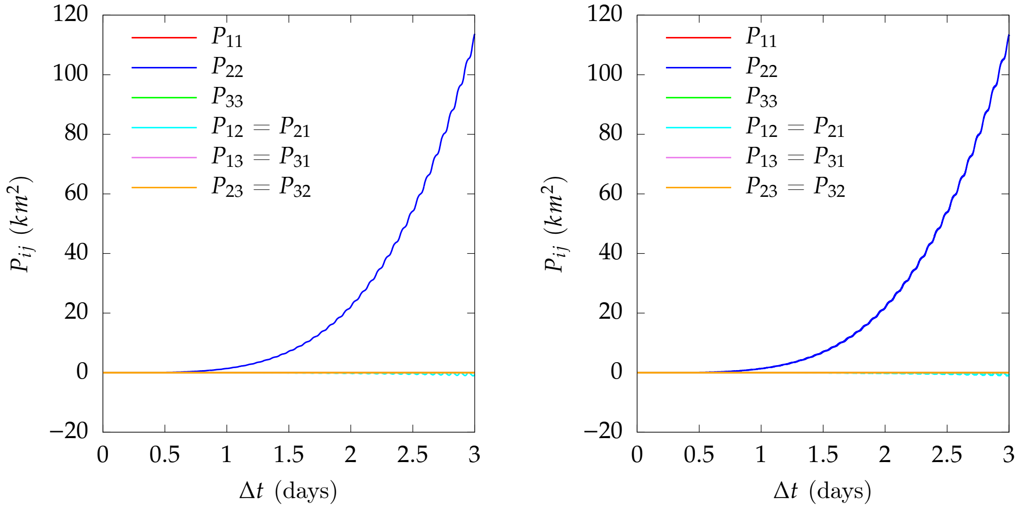

(a) Monte Carlo (b) UT Prediction

Figure 34. Monte Carlo and Unscented Transform Prediction Covariance Growth, CHAMP High Solar

sults in this format leaves out some information. For that reason results of the UT predictions and MC simulations are shown in Figures 35–41, wherein distribution point clouds (representing ensembles of realizations in the MC case and sigma points in the UT case) and 1σ Gaussian error ellipses are plotted at the final time for all two-dimensional combinations of the RTN principal directions for all scenarios and both SP prediction models.

Note the very close agreement between the results of MC simulation and UT prediction, which implies two things. Chiefly, the agreement validates the UT prediction scheme in terms of its uncertainty realism, as the MC model was already validated against the empirical results in a preceding section. Secondly, the agreement reaffirms the validity of letting B^* be the representative random variable within the air drag equation, as two stochastic prediction methods (MC simulation and UT prediction) which achieve uncertainty realism were developed using this paradigm.

The foundation of this approach is, of course, the calculation of the B^* time se-

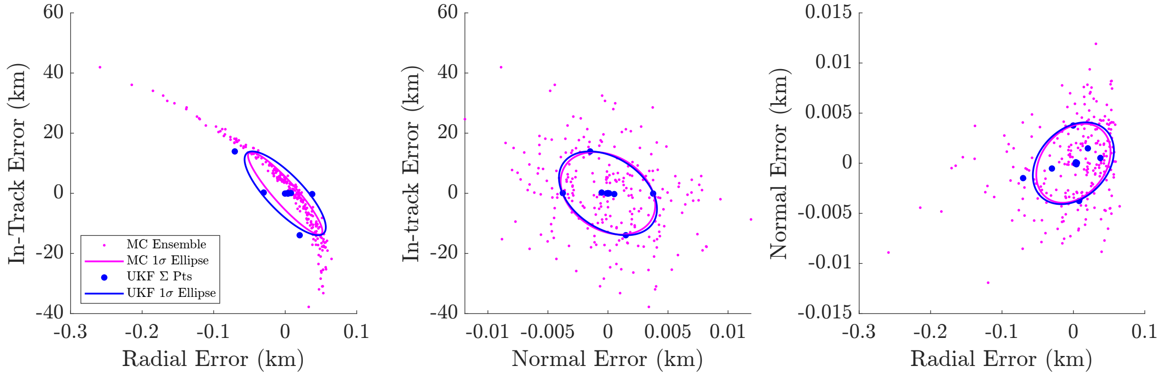

(a) SP A

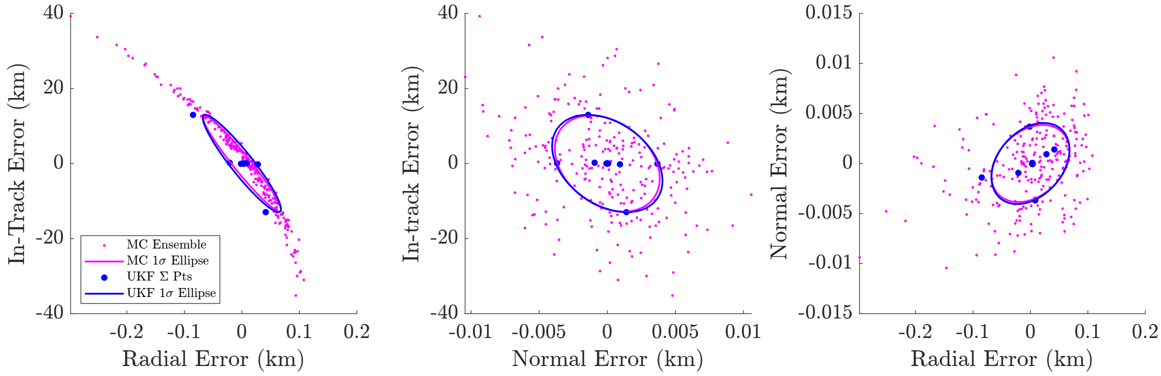

(b) SP B

Figure 35. Monte Carlo and Unscented Transform Prediction Final Covariance, CHAMP Low Solar

ries from observational data using estimation theory—a process which allows B^* to account for the overall prediction uncertainty of the underlying model. In this way B^* and the resulting time series contains more information than the physical definition of B^* in Equation 2, meaning B^* also acts as a correction variable which adjusts the model to the observational data. That this is true is also demonstrated quite clearly by the fact that the parameters of the B^* random process are very different depending on which SP model is being used (generally differing by an order of magnitude or more), which reflects the paradigm's ability to adapt to different atmospheric models. For example, reference the tabulated values of the B^* time series' mean and variance for the various scenarios for the two different SP models in Table 11. If B^* were still acting as simply the physical quantity represented by

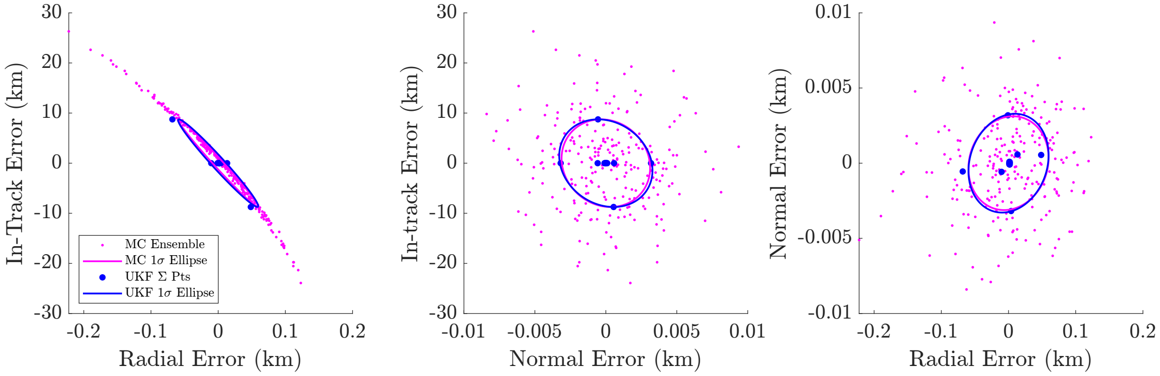

(a) SP A

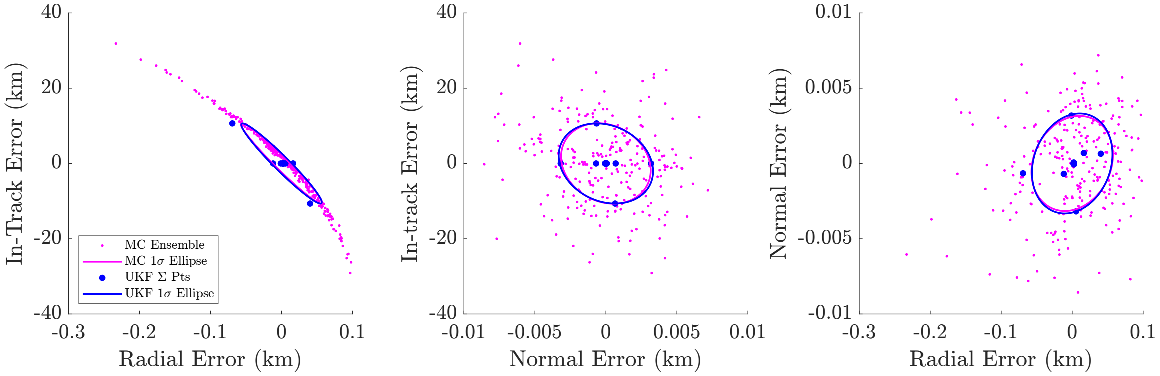

(b) SP B

Figure 36. Monte Carlo and Unscented Transform Prediction Final Covariance, CHAMP High Solar

$B^* = (1/2)C_D A/m$ as in Equation 2, then this would not be observed. Instead, it is demonstrated that B^* becomes the desired correction variable and absorbs the overall modeling uncertainty when modeled as a random variable and estimated from observational data. Note that this means the values in Table 11 no longer represent the physical definition of B^*, despite the units which are shown for consistency with Equation 2. (This also explains why B^* is sometimes less than zero when estimated or propagated as a SOGM RP, even though it physically should never be so.)

Additionally, note the very close agreement between UT results computed with the SP A prediction model and those computed with SP B. Again the results are nearly identical, which indicates that the UT stochastic prediction method can pro-

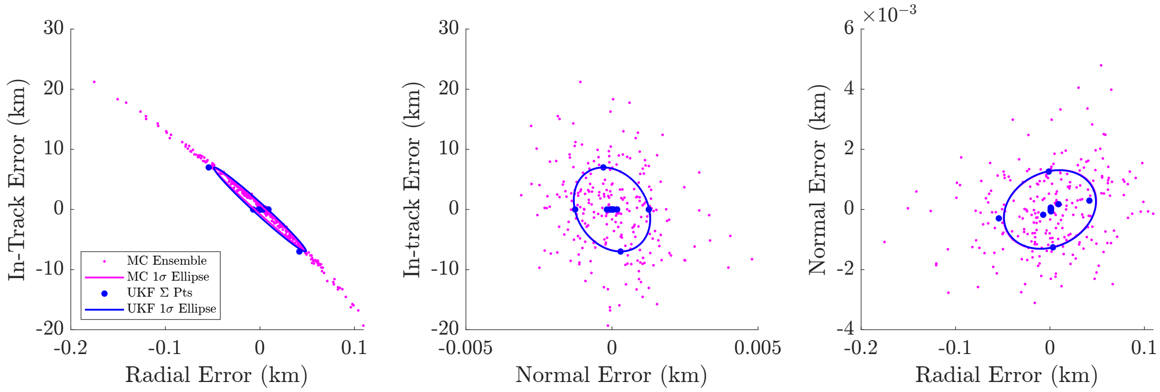

(a) SP A

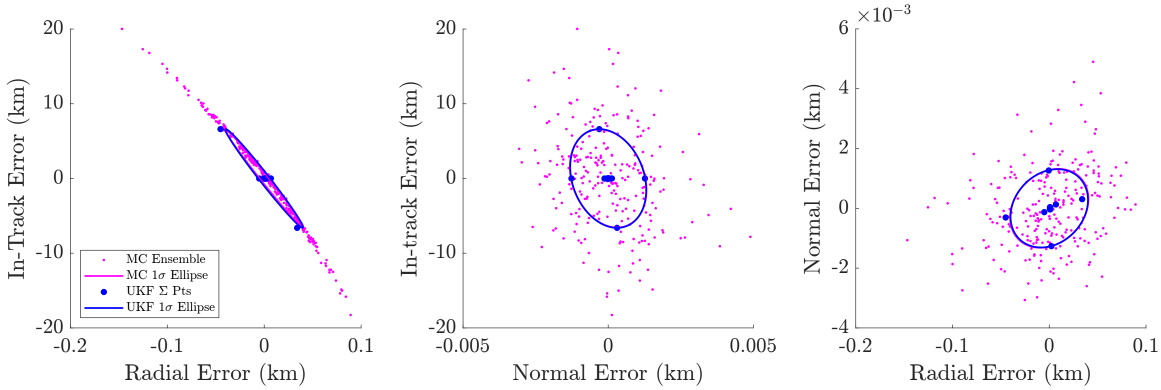

(b) SP B

Figure 37. Monte Carlo and Unscented Transform Prediction Final Covariance, GRACE-A Low Solar

Table 11. Mean and Variance of Calculated B^* Time Series for Each SP Prediction Model

	Solar	$\overline{B^*}$ (m^2/kg)		$\sigma^2_{B^*}$ (m^4/kg^2)	
Satellite	Level	SP A	SP B	SP A	SP B
CHAMP	Low	7.94×10^{-5}	1.96×10^{-3}	2.28×10^{-9}	1.35×10^{-6}
CHAMP	High	3.22×10^{-4}	2.77×10^{-3}	1.12×10^{-8}	8.96×10^{-7}
GRACE-A	Low	2.73×10^{-5}	3.35×10^{-3}	1.47×10^{-8}	2.14×10^{-4}
GRACE-A	High	2.62×10^{-4}	3.66×10^{-3}	1.20×10^{-8}	2.01×10^{-6}
GRACE-B	Low	2.68×10^{-5}	3.32×10^{-3}	1.45×10^{-8}	2.14×10^{-4}
GRACE-B	High	2.61×10^{-4}	3.65×10^{-3}	1.19×10^{-8}	2.01×10^{-6}
SOS	Low	1.41×10^{-6}	5.57×10^{-3}	1.16×10^{-7}	4.08×10^{-2}

duce realistic characterizations of uncertainty whilst being indifferent to the choice of atmospheric model. This provides additional evidence of the effectiveness of the B^* paradigm discussed in the preceding paragraph, and is also a potential benefit

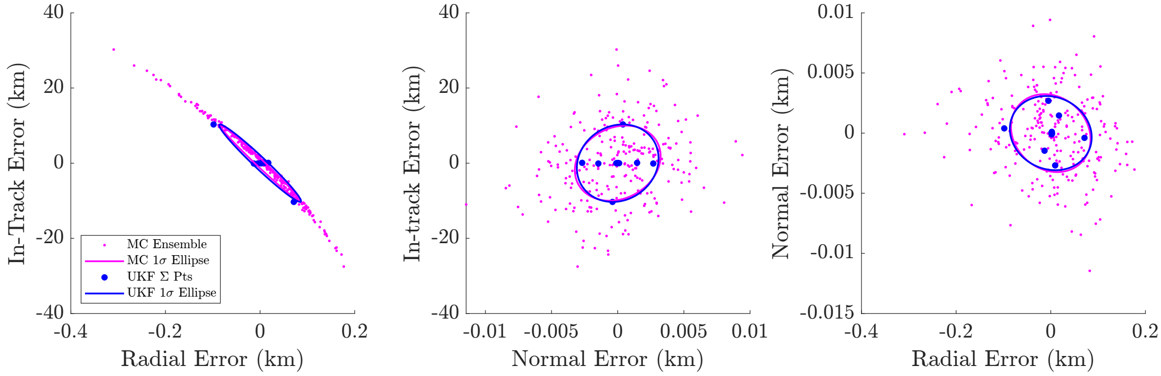

(a) SP A

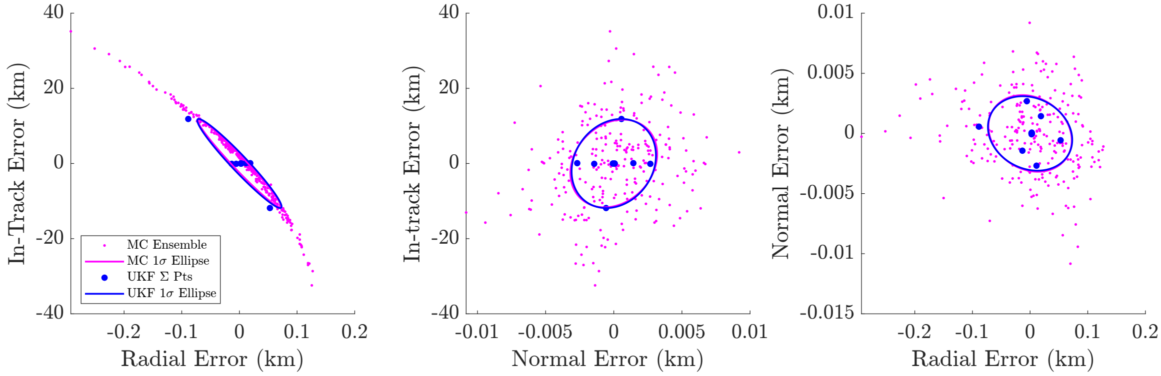

(b) SP B

Figure 38. Monte Carlo and Unscented Transform Prediction Final Covariance, GRACE-A High Solar

over stochastic methods which model the atmospheric density, the density error, or the solar flux inputs to an atmospheric model as random variables. The reason for this is the atmospheric model can be changed entirely in this development, and the realism of the uncertainty characterizations remains unchanged without needing to make any other updates to the formulation.

It is also important to recognize that these are the first results which contain the SOS scenario (again because SOS data was not robust enough to support empirical analysis). Examining Figure 41, note that the same agreement is present between MC simulation and UT prediction and between the results of SP A and SP B for the SOS scenario. This demonstrates that neither the viability of the stochastic prediction models nor the validity of the underlying paradigm are pred-

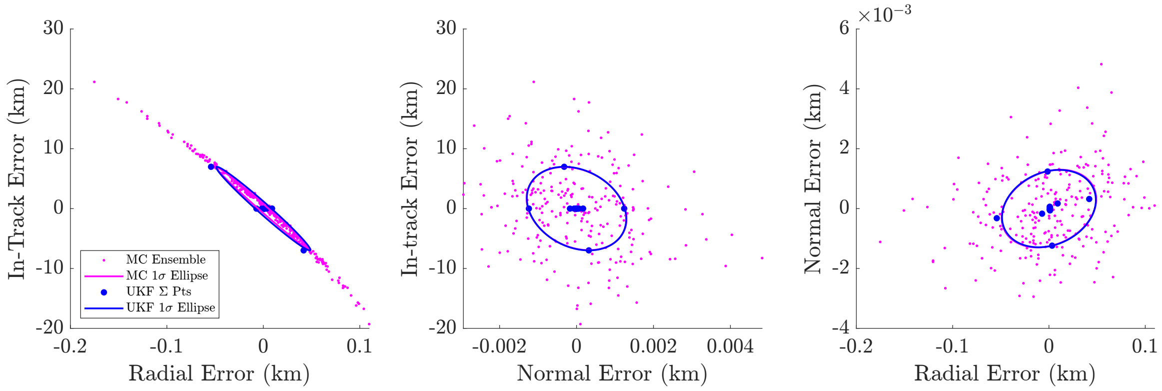

(a) SP A

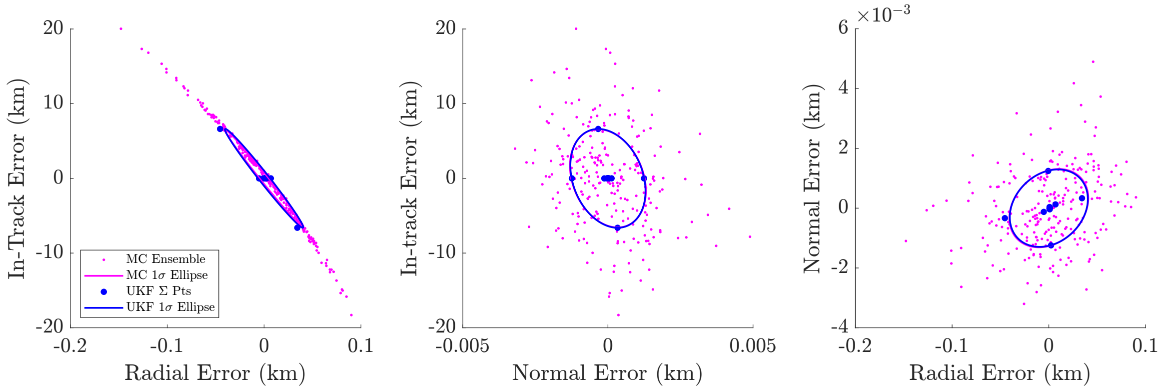

(b) SP B

Figure 39. Monte Carlo and Unscented Transform Prediction Final Covariance, GRACE-B Low Solar

icated on extremely precise observational data such as was used for CHAMP and GRACE-A/B, but that the models and paradigm are also effective when used with the type of position and velocity data received from a GPS receiver.

Finally, consider that the 1σ error ellipses depicted in Figures 36–41 assume that the joint distribution formed by the two coordinates in each sub-figure is a two-dimensional Gaussian random variable. Subjectively this seems to be a very reasonable assumption for all scenarios when considering the in-track/normal and the radial/normal pairs of coordinates, however the 1σ error ellipses seem less effective at depicting the true uncertainty distribution for the in-track/radial coordinate pair. In the case of the in-track/radial coordinate pair the cloud of er-

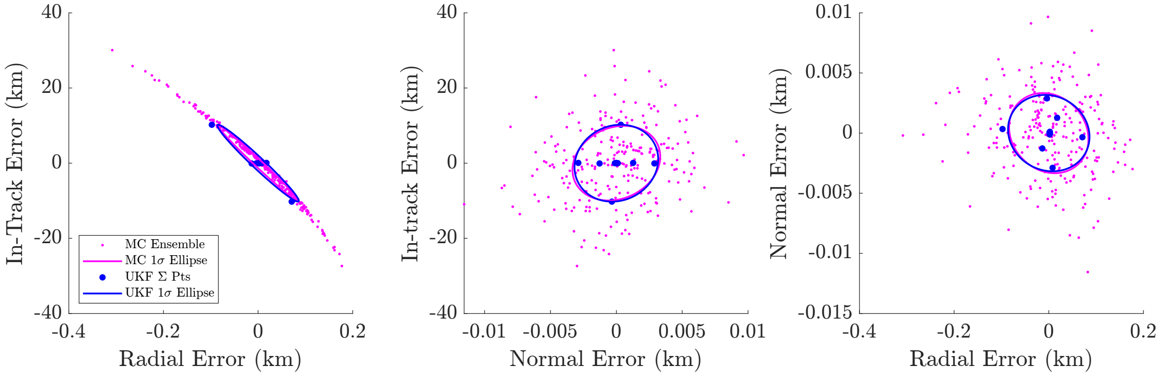

(a) SP A

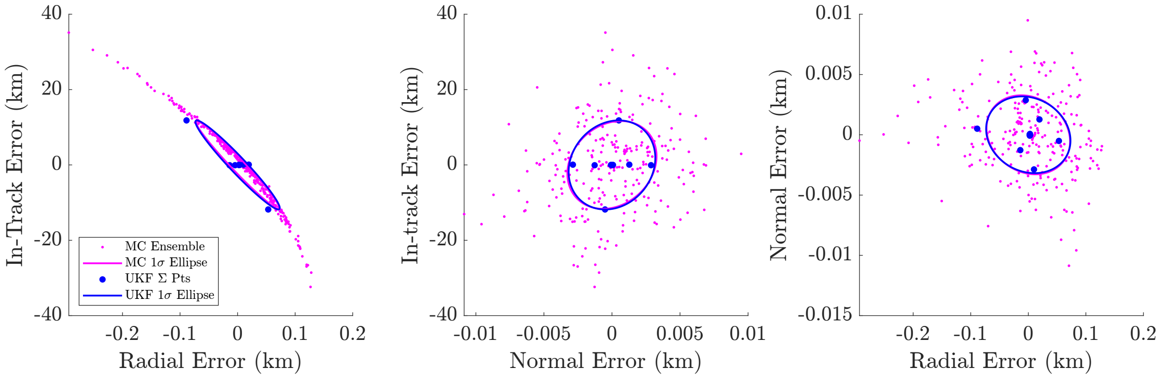

(b) SP B

Figure 40. Monte Carlo and Unscented Transform Prediction Final Covariance, GRACE-B High Solar

ror points seems to “bend” in a way that Gaussian error ellipses cannot precisely represent. This is indicative of what has been mentioned above—that non-linear satellite dynamics quickly cause the distributions of an orbit prediction to become non-Gaussian.

The use of the RTN coordinates helps but does not altogether eliminate this problem, however there are other actions that can be taken to enhance the realism of the uncertainty characterizations with respect to “Gaussian-ness”. The first option is to simply make the propagation time Δt shorter, as the non-Gaussian nature of the resulting probability distribution grows with time. This research used a Δt of 3 days, but in some applications this may be a longer prediction than is needed. A second option would be to reformulate the dynamics or transform the result

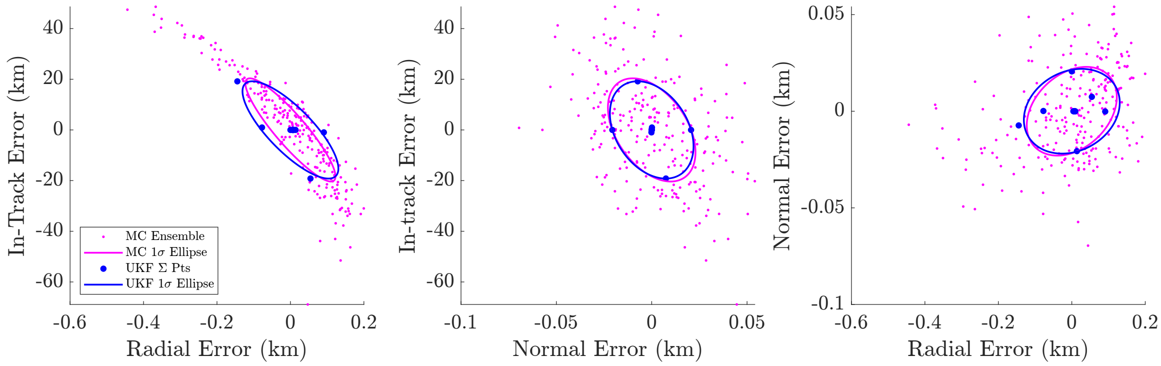

(a) SP A

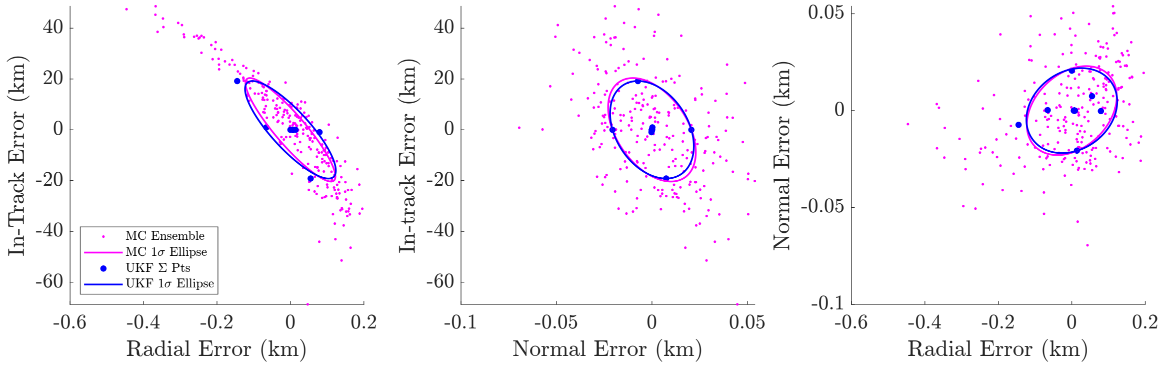

(b) SP B

Figure 41. Monte Carlo and Unscented Transform Prediction Final Covariance, SOS Low Solar

into a coordinate system that maintains Gaussian characteristics even longer than the RTN frame used here, such as equinoctial elements [63] or curvilinear coordinates [106]. Finally, a third option is to use a different stochastic prediction method, abandoning or modifying the UT method in favor of one that either doesn't require the random variables to be Gaussian or lessens this restriction. One example class of methods are those that use Gaussian mixture models wherein a non-Gaussian distribution is approximated as a weighted sum of Gaussian distributions [66]. Gaussian mixture models can be used with UT methods and can capture non-Gaussian posterior distributions with high fidelity [68]. Other types of stochastic propagation exist as well, some of which were reviewed in Chapter II.

Ultimately, the mismatch between the Gaussian assumption inherent in UT prediction and the results above is not extreme, and the results presented above were deemed useful for analysis and the drawing of conclusions with the acknowledgment that Gaussian error ellipses are imperfect representations of some of the resulting distributions.

Finally, recall that one of the aims of the stochastic prediction model was that it not require a large number of realizations as MC simulation does. This is motivated by the computational expense of MC simulation and the desire that the stochastic model be faster than MC simulation for practical use purposes. To that point, the UT prediction method described above is considerably faster than MC simulation ($N_{\mathrm{MC}} = 250$), particularly for the simpler atmosphere used in SP A. Example computation times on a personal laptop computer for MC simulation and UT prediction are given for a single example scenario in Table 12 as a demonstration of this.

Table 12. Computation Times for Monte Carlo Analysis and Unscented Transform Prediction, CHAMP Low Solar

Prediction Method	Computation Time (min) SP A	SP B
MC Simulation	7.3	15.2
UT Prediction	2.0	7.4

6.3 On-board Stochastic Orbit Prediction and Real-Time Filtering

While not the main thrust of this research, it is interesting to consider that the stochastic prediction methods presented herein may be viable for use on-board a satellite equipped with a GPS receiver. The results of stochastic propagations for the SOS scenario demonstrate this most readily as they are based on just the type of data that may be available on-board a satellite.

The feature of this research which makes this feasible is the method's adaptability with respect to the atmospheric density used in the dynamics, which is directly enabled by allowing B^* to be the representative random variable for air drag. For example, the Regan and Anandakrishnan density model used in SP A does not require any external data whatsoever—all results above which used the SP A prediction model needed only position (and velocity, optionally) observation data. Therefore, the only limiting factors for a satellite to perform stochastic orbit predictions on-board (and even autonomously) via this method is the availability of position data and enough computing power to calculate and analyze the B^* time-series and then perform the stochastic prediction.

In general, calculating a 7-day B^* time series as used in the stochastic prediction methods above took an average time of approximately 4 minutes on a laptop computer, however an on-board computer could drastically reduce this by storing the estimated B^* values in a rolling buffer and calculating only one new B^* value when observational data is available (which on the same laptop took approximately 1–2 seconds) and then calculating the new autocorrelation and SOGM parameters (which took fractions of a second). Estimating the latest B^* value can also return the estimated state vector given the most updated observational data as well, meaning the only remaining task would be to execute the stochastic prediction. This took an average of 2 minutes (again on a laptop computer), however the underlying computer code has not been optimized for speed and other, more efficient UKF formulations than the method used above are likely possible.

Though the preceding discussion is not an in-depth study and the computational power on-board a satellite is likely to be significant less than that of a laptop computer, it is evident that on-board use of the stochastic prediction methods presented here is possible. Such a capability could help with a variety of autonomous satellite missions. Additionally, it's worth noting that the computer code used for this research was written in C++, a compiled language which is generally straightforward to adapt for use on microcontrollers or microcomputers, if it isn't supported natively.

A final consideration regarding stochastic prediction is that of real-time filtering. The focus of this research has been on stochastic *prediction*, that is estimating the state of the satellite at some time in the future beyond available observational data. Calculating the initial conditions for predictions has been accomplished via non-linear least squares, which is a batch estimation method. It should also be possible, if desired, to use a filtering scheme to update a satellite's state and uncertainty in real time as observational data becomes available. In its simplest form, such a scheme would be an alternative method of obtaining the initial conditions from which to initiate a stochastic prediction, however it may also be possible to estimate B^* and possibly even the values and/or nature of the B^* random process in a real-time filtering scheme. This is mentioned here as a possible avenue of further research and is not investigated further.

6.4 Conclusions

The results presented in this chapter demonstrate the effectiveness of the research's central paradigm: that a stochastic prediction method which models the uncertainty caused by air drag with a single random variable B^* can produce predictions with realistic characterizations of uncertainty. This was chiefly demonstrated by the agreement between the results of Monte Carlo simulation and empirical covariance matrix analysis which links the stochastic model with the physical reality, and agreement of the Unscented Transform stochastic prediction model with MC simulation which validated the uncertainty realism produced by Unscented Transform model. Additionally, the fact that omitting the B^* random process from the stochastic model results in significant underestimation of the in-track uncertainty while including it results in model agreement is evidence that modeling B^* as the lone random variable of air drag is a viable stochastic foundation for these stochastic prediction models.

A core benefit of this paradigm is that the resultant stochastic prediction models are effective for a wide range of atmospheric density models. This is confirmed by the very close agreement of results obtained using SP A and SP B, which employ disparate atmospheric density models. Additionally, that the performance of the predictor when using a relatively simple atmosphere model compares so closely with the performance when using a much more refined atmosphere model is further evidence that modeling B^* as a random variable and then forming the system stochastics around a time series of B^* estimates compensates for modeling errors very well and enables realistic characterizations of uncertainty.

Finally, results for the SOS scenario demonstrate that the stochastic prediction methods presented above remain effective with less refined input data. This result, coupled with the advantage that an atmospheric model which requires no external input data can be used, means that the stochastic prediction model may be suitable for use on-board an orbiting satellite.

The results presented in this chapter confirm the expectations of Research Hypothesis 3.

VII. Conclusion

This chapter presents conclusions based on the results of this research, reinforces the contributions made by this research, and lists several possible research avenues that could be pursued in the future.

7.1 Research Conclusions

The aim of this research was to investigate a new paradigm related to the satellite prediction uncertainty caused by air drag: that modeling the ballistic coefficient B^* as the only dynamically random variable can yield a stochastic prediction model which realistically characterizes its modeling prediction uncertainty. The first step toward doing this was to validate the effect of air drag on LEO satellite orbit prediction.

Analyzing empirically calculated prediction covariance matrices, particularly how these covariance matrices grow with the length of the propagation time, demonstrated that air drag is the predominant source of modeling prediction uncertainty for LEO satellites. Additionally, it was found that nearly all of this prediction uncertainty is resident in the satellite's in-track direction, the principal direction of action of air drag.

It is also relevant that two special perturbations prediction models which use disparate atmospheric models produced nearly identical empirical covariance matrices and prediction accuracy by estimating B^* values from observational data. Although the dynamics formulation used for empirical analysis is deterministic, this result starts to validate the idea that B^* is a variable that can absorb and account for modeling errors very effectively by estimating its value using non-linear least squares and observational data.

Extending this insight from the regime of determinism to that of stochastic prediction, successive B^* estimates were assembled into time series and then analyzed as random processes. Analysis of ensembles and single realizations of these time series provided evidence for assuming that the B^* random process is both stationary and ergodic (the ergodicity assumption is more valid for longer single realizations than for shorter ones). The fact that the random processes possessed both stationary and ergodic properties, coupled with the nature of the processes' autocorrelation functions, led to the selection of a second-order Gauss-Markov (SOGM) process to model the B^* random process. It was then shown that the B^* random process can be parameterized programmatically using only the autocorrelation of the calculated B^* time series, and that the parameterization could be used to generate realizations of the random process with statistics that agreed quite closely with those of the calculated random processes. That the random process parameterization was completed without need of manual tuning or other operator assumptions is a distinction of this method.

The SOGM process model proved to be a suitable fit to the calculated B^* random processes, but the random processes were sensitive to how much observational data was provided to the least squares algorithm that estimated each B^* value and a different random process model may be more applicable for values of N_{LS} greater than about 900. The fact that the random process was sensitive to model parameters indicates that the model is self-consistent and provides further evidence that capturing modeling uncertainty via a B^* random process results in a model that is capable of realistic uncertainty characterization. The reason for this is that the random process sensitivity demonstrates that B^*, when estimated using observational data, takes on more information than its physical definition and becomes a correction factor which absorbs errors in the underlying model.

This B^* random process analysis was used as the stochastic foundation of Monte Carlo simulation. Monte Carlo simulation results confirmed that a stochastic prediction model which models B^* as a random process in the above manner is capable of achieving uncertainty realism. This is demonstrated by the agreement of Monte Carlo simulation results with the results empirical covariance analysis—linking the stochastic prediction model with the physical reality.

A second stochastic prediction model using the Unscented Transform proved equally capable of realistically characterizing its modeling uncertainty. This was demonstrated by agreement between the results of the Unscented Transform prediction model and those of Monte Carlo simulation which were already validated by comparison to empirical results. Additionally, the Unscented Transform prediction model was shown to be at least twice as fast as Monte Carlo simulation, with additional optimization likely being possible.

The stochastic prediction models produced nearly identical results for formulations using the same two special perturbations models as the empirical analyses. These two special perturbations models use very different atmospheric density models, which indicates that the uncertainty realism of the stochastic prediction is not linked to a choice of atmospheric model. This demonstrates two things. First, this shows that modeling B^* as a random process and the only constituent random variable of air drag is a viable method of capturing overall modeling uncertainty—via estimation from observational data B^* acts as an absorber of modeling errors which leads to realistic uncertainty characterizations. Second, the stochastic model is more adaptable than stochastic formulations which are tied either directly or indirectly to a particular atmospheric model or class of models.

An example benefit of this stochastic prediction model is that it is effective when using an atmospheric model which requires no external input data, such as that used by special perturbations model “A”. The stochastic model was also demonstrated to be effective when using the type of observational data that could be available on board a satellite equipped with a GPS receiver, as in the SOS scenario. These two facts suggest that the stochastic prediction models presented in this research, or a similar model based on this research’s novel paradigm of regarding B^* as a random variable, could be used autonomously on-board a satellite.

7.2 Contributions

The research presented here makes four distinct contributions to the field of astrodynamics. First, the results of the empirical analyses expand the verification that air drag is the predominant source of modeling prediction uncertainty and that this uncertainty is almost entirely realized in the in-track direction. This expands previous research by using more prediction models and additional data sources.

Next, previous work in the stochastics of air drag have generally focused on the air density, relative density error, or inputs to atmospheric models as random variables. This research adopts a novel paradigm: that letting B^* be the only constituent random variable of air drag frees the stochastic development from any dependency on a particular atmospheric density model.

This is also the first work to calculate a time series of B^* estimates, characterize and parameterize a random process model from said time series, and use this as the foundation of a stochastic prediction model. Further, this process is completed programmatically, requiring no manual tuning or operator assumptions. This is distinct from previous work in LEO satellite stochastic prediction, which has generally assumed a type of random process and/or manually tuned the process parameters.

The final contribution is the stochastic prediction model based on this novel paradigm. The model's chief distinctions from prior work are its adaptability to various dynamics formulations and atmospheric density models, and that the stochastic parameters can be estimated directly from observational data via estimation of B^*. The model is also likely viable for on-board use.

7.3 Future Research

There are several potential extensions to this research available for future work. For one, the Unscented Transform-based stochastic prediction model could be reformulated to use a stochastic propagator which is better able to handle non-Gaussian posterior distributions. Doing so need not invalidate the basis of the B^* random process or the paradigm on which the stochastics are founded, as other available stochastic propagation or filtering methods readily handle non-linear, stochastic dynamics. Some of these are reviewed in Chapters II and VI.

Another possible method for handling non-Gaussian prediction results could be to reformulate the prediction methods using an alternative coordinate system. Curvilinear coordinates, for example, are known to remain Gaussian in predictions longer than either Cartesian coordinates or the radial, transverse, and normal coordinates used in this research.

There are also two discrepancies in the stochastic model formulations which were noted in the preceding chapters and could be improved upon in future research. The first is the difference between uncertainty values in the normal direction when comparing empirical analysis with Monte Carlo simulation. The second is that the method used for estimating the initial covariance of a prediction likely underestimates the uncertainty, which could be rectified by exploring other methods that exist for the purpose which are mentioned in Chapter VI.

Another modification could enable the use of satellite attitude information to potentially increase prediction accuracy, if desired. By appending a dimensionless correction variable S to Equation 2 as in Equation 69 and performing the random process analysis described in Chapter V using S as the random variable, B^* could be used to incorporate knowledge of any changes in the satellite's orientation that affect cross-sectional area (or other known changes in any constituent variable of B^*).

$$\boldsymbol{a}_D = -SB^* \rho \boldsymbol{v}_{\text{rel}} v_{\text{rel}} \tag{69}$$

Approaching the stochastics this way is essentially the same method as that presented in this research, except S would be appended to the state vector and become the correction variable that characterizes the predictions' stochastics when estimated from observational data and B^* would revert to a deterministic variable with dynamics described by whatever is known about the satellite's orientation.

Additionally, this research considered prediction scenarios during periods of high and low solar activity based on the F10.7 solar flux index for the purpose of validating the stochastic model's performance for a range of space environments. The linkage between solar activity and positional uncertainty could certainly be explored further, however, including from a causation perspective.

Finally, it is postulated in this research that the stochastic prediction model is viable for use on-board a satellite with a GPS receiver, though this assertion was not rigorously tested. Future research in this area could include optimizing and re-compiling the stochastic prediction model for use on a micro-controller which is suitable for use on-board a satellite, and culminate with running a hardware-based simulation.

Appendix A. Partial Derivatives of the A Matrix

The A matrix (the Jacobian of the equations of motion) for the SP models described in Chapter III is given by Equation 70.

$$A(t) = \left.\frac{\partial \boldsymbol{f}}{\partial \boldsymbol{X}}\right|_{\boldsymbol{X}(t)} = \begin{bmatrix} 0 & 0 & 0 & 1 & 0 & 0 & 0 \\ 0 & 0 & 0 & 0 & 1 & 0 & 0 \\ 0 & 0 & 0 & 0 & 0 & 1 & 0 \\ A_{41} & A_{42} & A_{43} & A_{44} & A_{45} & A_{46} & A_{47} \\ A_{51} & A_{52} & A_{53} & A_{54} & A_{55} & A_{56} & A_{57} \\ A_{61} & A_{62} & A_{63} & A_{64} & A_{65} & A_{66} & A_{67} \\ 0 & 0 & 0 & 0 & 0 & 0 & 0 \end{bmatrix} \tag{70}$$

The non-trivial elements of A, labeled as A_{ij} in Equation 70, are given by Equations 71–91.

$$A_{41} = \frac{\partial}{\partial x}\left(-\frac{\partial V}{\partial x} + a_{D,x}\right) = -\frac{\partial^2 V}{\partial x^2} + \frac{\partial a_{D,x}}{\partial x} \tag{71}$$

$$A_{51} = \frac{\partial}{\partial x}\left(-\frac{\partial V}{\partial y} + a_{D,y}\right) = -\frac{\partial^2 V}{\partial x \partial y} + \frac{\partial a_{D,y}}{\partial x} \tag{72}$$

$$A_{61} = \frac{\partial}{\partial x}\left(-\frac{\partial V}{\partial z} + a_{D,z}\right) = -\frac{\partial^2 V}{\partial x \partial z} + \frac{\partial a_{D,z}}{\partial x} \tag{73}$$

$$A_{42} = \frac{\partial}{\partial y}\left(-\frac{\partial V}{\partial x} + a_{D,x}\right) = -\frac{\partial^2 V}{\partial y \partial x} + \frac{\partial a_{D,x}}{\partial y} \tag{74}$$

$$A_{52} = \frac{\partial}{\partial y}\left(-\frac{\partial V}{\partial y} + a_{D,y}\right) = -\frac{\partial^2 V}{\partial y^2} + \frac{\partial a_{D,y}}{\partial y} \tag{75}$$

$$A_{62} = \frac{\partial}{\partial y}\left(-\frac{\partial V}{\partial z} + a_{D,z}\right) = -\frac{\partial^2 V}{\partial y \partial z} + \frac{\partial a_{D,z}}{\partial y} \tag{76}$$

$$A_{43} = \frac{\partial}{\partial z}\left(-\frac{\partial V}{\partial x} + a_{D,x}\right) = -\frac{\partial^2 V}{\partial z \partial x} + \frac{\partial a_{D,x}}{\partial z} \tag{77}$$

$$A_{53} = \frac{\partial}{\partial z}\left(-\frac{\partial V}{\partial y} + a_{D,y}\right) = -\frac{\partial^2 V}{\partial z \partial y} + \frac{\partial a_{D,y}}{\partial z} \tag{78}$$

$$A_{63} = \frac{\partial}{\partial z}\left(-\frac{\partial V}{\partial z} + a_{D,z}\right) = -\frac{\partial^2 V}{\partial z^2} + \frac{\partial a_{D,z}}{\partial z} \tag{79}$$

$$A_{44} = \frac{\partial}{\partial v_x}\left(-\frac{\partial V}{\partial x} + a_{D,x}\right) = \frac{\partial a_{D,x}}{\partial v_x} \tag{80}$$

$$A_{54} = \frac{\partial}{\partial v_x}\left(-\frac{\partial V}{\partial y} + a_{D,y}\right) = \frac{\partial a_{D,y}}{\partial v_x} \tag{81}$$

$$A_{64} = \frac{\partial}{\partial v_x}\left(-\frac{\partial V}{\partial z} + a_{D,z}\right) = \frac{\partial a_{D,z}}{\partial v_x} \tag{82}$$

$$A_{45} = \frac{\partial}{\partial v_y}\left(-\frac{\partial V}{\partial x} + a_{D,x}\right) = \frac{\partial a_{D,x}}{\partial v_y} \tag{83}$$

$$A_{55} = \frac{\partial}{\partial v_y}\left(-\frac{\partial V}{\partial y} + a_{D,y}\right) = \frac{\partial a_{D,y}}{\partial v_y} \tag{84}$$

$$A_{65} = \frac{\partial}{\partial v_y}\left(-\frac{\partial V}{\partial z} + a_{D,z}\right) = \frac{\partial a_{D,z}}{\partial v_y} \tag{85}$$

$$A_{46} = \frac{\partial}{\partial v_z}\left(-\frac{\partial V}{\partial x} + a_{D,x}\right) = \frac{\partial a_{D,x}}{\partial v_z} \tag{86}$$

$$A_{56} = \frac{\partial}{\partial v_z}\left(-\frac{\partial V}{\partial y} + a_{D,y}\right) = \frac{\partial a_{D,y}}{\partial v_z} \tag{87}$$

$$A_{66} = \frac{\partial}{\partial v_z}\left(-\frac{\partial V}{\partial z} + a_{D,z}\right) = \frac{\partial a_{D,z}}{\partial v_z} \tag{88}$$

$$A_{47} = \frac{\partial}{\partial B^*}\left(-\frac{\partial V}{\partial x} + a_{D,x}\right) = \frac{\partial a_{D,x}}{\partial B^*} \tag{89}$$

$$A_{57} = \frac{\partial}{\partial B^*}\left(-\frac{\partial V}{\partial y} + a_{D,y}\right) = \frac{\partial a_{D,y}}{\partial B^*} \tag{90}$$

$$A_{67} = \frac{\partial}{\partial B^*}\left(-\frac{\partial V}{\partial z} + a_{D,z}\right) = \frac{\partial a_{D,z}}{\partial B^*} \tag{91}$$

The second partials of the geopotential V are obtained from the Pines algorithm as explained in Chapter III.

Separating Equation 2 into its Cartesian components and expanding $\boldsymbol{v}_{\text{rel}}$ according to Equation 9 gives the following.

$$a_{D,x} = -B^*\rho(\boldsymbol{r})\left((v_x+\omega_\oplus y)^2+(v_y-\omega_\oplus x)^2+v_z^2\right)^{\frac{1}{2}}(v_x+\omega_\oplus y) \tag{92}$$

$$a_{D,y} = -B^*\rho(\boldsymbol{r})\left((v_x+\omega_\oplus y)^2+(v_y-\omega_\oplus x)^2+v_z^2\right)^{\frac{1}{2}}(v_y-\omega_\oplus x) \tag{93}$$

$$a_{D,z} = -B^*\rho(\boldsymbol{r})\left((v_x+\omega_\oplus y)^2+(v_y-\omega_\oplus x)^2+v_z^2\right)^{\frac{1}{2}}v_z \tag{94}$$

The final values needed for A matrix are the partial derivatives of Equations 92–94, given below (note that ρ is used as shorthand for $\rho(\boldsymbol{r}) = \rho(x, y, z)$).

$$\frac{\partial a_{D,x}}{\partial x} = -B^* v_{\text{rel},x}\left(\tfrac{\partial\rho}{\partial x}v_{\text{rel}} - \frac{\omega_\oplus\rho v_{\text{rel},y}}{v_{\text{rel}}}\right) \tag{95}$$

$$\frac{\partial a_{D,x}}{\partial y} = -B^*\left(v_{\text{rel},x}v_{\text{rel}}\tfrac{\partial\rho}{\partial y} + \frac{\omega_\oplus {v_{\text{rel},x}}^2\rho}{v_{\text{rel}}} + \omega_\oplus\rho v_{\text{rel}}\right) \tag{96}$$

$$\frac{\partial a_{D,x}}{\partial z} = -B^* v_{\text{rel},x}\tfrac{\partial\rho}{\partial z}v_{\text{rel}} \tag{97}$$

$$\frac{\partial a_{D,y}}{\partial x} = -B^*\left(v_{\text{rel},y}\tfrac{\partial\rho}{\partial x}v_{\text{rel}} - \frac{\omega_\oplus {v_{\text{rel},y}}^2\rho}{v_{\text{rel}}} - \omega_\oplus\rho v_{\text{rel}}\right) \tag{98}$$

$$\frac{\partial a_{D,y}}{\partial y} = -B^* v_{\text{rel},y}\left(\frac{\omega_\oplus\rho v_{\text{rel},x}}{v_{\text{rel}}} + \tfrac{\partial\rho}{\partial y}v_{\text{rel}}\right) \tag{99}$$

$$\frac{\partial a_{D,y}}{\partial z} = -B^* v_{\text{rel},y}\tfrac{\partial\rho}{\partial z}v_{\text{rel}} \tag{100}$$

$$\frac{\partial a_{D,z}}{\partial x} = -B^* v_z\left(\tfrac{\partial\rho}{\partial x}v_{\text{rel}} - \frac{\omega_\oplus v_{\text{rel},y}\rho}{v_{\text{rel}}}\right) \tag{101}$$

$$\frac{\partial a_{D,z}}{\partial y} = -B^* v_z\left(\frac{\omega_\oplus v_{\text{rel},x}\rho}{v_{\text{rel}}} + \tfrac{\partial\rho}{\partial y}v_{\text{rel}}\right) \tag{102}$$

$$\frac{\partial a_{D,z}}{\partial z} = -B^* v_z\tfrac{\partial\rho}{\partial z}v_{\text{rel}} \tag{103}$$

$$\frac{\partial a_{D,x}}{\partial v_x} = -B^*\rho\left(\frac{{v_{\text{rel},x}}^2}{v_{\text{rel}}} + v_{\text{rel}}\right) \tag{104}$$

$$\frac{\partial a_{D,x}}{\partial v_y} = \frac{-B^* v_{\text{rel},y}v_{\text{rel},x}\rho}{v_{\text{rel}}} \tag{105}$$

$$\frac{\partial a_{D,x}}{\partial v_z} = \frac{-B^* v_z v_{\text{rel},x} \rho}{v_{\text{rel}}} \tag{106}$$

$$\frac{\partial a_{D,y}}{\partial v_x} = \frac{-B^* v_{\text{rel},y} v_{\text{rel},x} \rho}{v_{\text{rel}}} \tag{107}$$

$$\frac{\partial a_{D,y}}{\partial v_y} = -B^* \rho \left(\frac{{v_{\text{rel},y}}^2}{v_{\text{rel}}} + v_{\text{rel}} \right) \tag{108}$$

$$\frac{\partial a_{D,y}}{\partial v_z} = \frac{-B^* v_z v_{\text{rel},y} \rho}{v_{\text{rel}}} \tag{109}$$

$$\frac{\partial a_{D,z}}{\partial v_x} = \frac{-B^* v_z v_{\text{rel},x} \rho}{v_{\text{rel}}} \tag{110}$$

$$\frac{\partial a_{D,z}}{\partial v_y} = \frac{-B^* v_z v_{\text{rel},y} \rho}{v_{\text{rel}}} \tag{111}$$

$$\frac{\partial a_{D,z}}{\partial v_z} = -B^* \rho \left(\frac{v_z^2}{v_{\text{rel}}} + v_{\text{rel}} \right) \tag{112}$$

Finally, some atmospheric models (such as the Regan and Anandakrishnan one used in this research) provide the density gradient in the form $\frac{\partial \rho}{\partial r}$ where $r = ||\boldsymbol{r}|| = \sqrt{x^2 + y^2 + z^2}$. This can be separated into Cartesian coordinates for use in the above equations via Equations 113–115.

$$\frac{\partial \rho}{\partial x} = \frac{\partial \rho}{\partial r} \frac{\partial r}{\partial x} = \frac{\partial \rho}{\partial r} \frac{x}{r} \tag{113}$$

$$\frac{\partial \rho}{\partial y} = \frac{\partial \rho}{\partial r} \frac{\partial r}{\partial y} = \frac{\partial \rho}{\partial r} \frac{y}{r} \tag{114}$$

$$\frac{\partial \rho}{\partial z} = \frac{\partial \rho}{\partial r} \frac{\partial r}{\partial z} = \frac{\partial \rho}{\partial r} \frac{z}{r} \tag{115}$$

Appendix B. Non-Linear Least Squares Estimation Algorithm

The non-linear least squares implementation used in this research is adapted from Wiesel [2, pgs. 69–72] and begins with a reference orbit $\boldsymbol{X}_{\text{ref}}$ which is numerically integrated from the time of the first observational data point t_0, and its differential state transition matrix $\Phi(t, t_0)$ (see Equation 11). In this research $\boldsymbol{X}_{\text{ref}}$ was initialized using the position and velocity of the first observation point and a guessed initial value for B^* (the value of 0.00045 was used throughout this research as convergence occurred very quickly and there was no need to alter the guess between scenarios).

Let each subsequent observation at time t_i be $\boldsymbol{z}_i$, and define the residual $\boldsymbol{r}_i$ as the difference between the actual observation $\boldsymbol{z}_i$ and the expected observation given reference orbit $\boldsymbol{X}_{\text{ref}}(t_i)$

$$\boldsymbol{r}_i = \boldsymbol{z}_i - \boldsymbol{z}_{i,\text{predicted}} = \boldsymbol{z}_i - H\boldsymbol{X}_{\text{ref}} \tag{116}$$

where H is a linear relationship (in this case) between the state and observation data given by Equation 117.

$$H \equiv \left[\ I(6 \times 6)\ \middle|\ \mathbf{0}(6 \times 1)\ \right] \tag{117}$$

Each observation $\boldsymbol{z}_i$ has uncertainty associated with it, given by the matrix Q_i. For this research Q_i is constant, diagonal, and composed of the σ_r and σ_v values given in Table 1, as shown in Equation 118.

$$Q_i = \begin{bmatrix} \sigma_r & 0 & 0 & 0 & 0 & 0 \\ 0 & \sigma_r & 0 & 0 & 0 & 0 \\ 0 & 0 & \sigma_r & 0 & 0 & 0 \\ 0 & 0 & 0 & \sigma_v & 0 & 0 \\ 0 & 0 & 0 & 0 & \sigma_v & 0 \\ 0 & 0 & 0 & 0 & 0 & \sigma_v \end{bmatrix} \tag{118}$$

As Q_i is diagonal, its inverse is easily calculated by taking the reciprocal of each individual element, as in Equation 119.

$$Q_i^{-1} = \begin{bmatrix} \sigma_r^{-1} & 0 & 0 & 0 & 0 & 0 \\ 0 & \sigma_r^{-1} & 0 & 0 & 0 & 0 \\ 0 & 0 & \sigma_r^{-1} & 0 & 0 & 0 \\ 0 & 0 & 0 & \sigma_v^{-1} & 0 & 0 \\ 0 & 0 & 0 & 0 & \sigma_v^{-1} & 0 \\ 0 & 0 & 0 & 0 & 0 & \sigma_v^{-1} \end{bmatrix} \tag{119}$$

At this point data rejection can be implemented if desired by rejecting observations for which the residual is “larger” than a threshold value. In this research data was rejected if the magnitude of the position vector of the observational data point differed from the magnitude of the position vector of the reference orbit by more than a threshold value. This threshold value was set to 250 kilometers, however (effectively deactivating data rejection), as data rejection turned out not to be necessary due to the quality of the available data (including for SOS).

The output of each iteration of the non-linear least squares method is a correction to the initial state of the reference orbit $\delta \boldsymbol{X}(t_0)$. Assuming that this correction is small, it can be propagated using the first-order linear approximation of the satellite dynamics given by $\Phi(t_i, t_0)$ according to Equation 120.

$$\delta \boldsymbol{X}(t_i) = \Phi(t_i, t_0)\delta \boldsymbol{X}(t_0) \tag{120}$$

Each residual $\boldsymbol{r}_i$ is related to the propagated correction according to Equation 121

$$\boldsymbol{r}_i = H\Phi(t_i, t_0)\delta \boldsymbol{X}(t_0) = T_i \delta \boldsymbol{X}(t_0) \tag{121}$$

where $T_i = H\Phi(t_i, t_0)$ is an intermediate variable introduced for convenience.

The necessary correction to the reference orbit at t_0 and the covariance of this correction are then (as given by Wiesel, see [2] for greater detail if desired)

$$\delta \boldsymbol{X}(t_0) = \left(T^T Q^{-1} T\right)^{-1} T^T Q^{-1} \boldsymbol{r} \tag{122}$$

$$P_{\delta X} = \left(T^T Q^{-1} T\right)^{-1} \tag{123}$$

where T, Q, and $\boldsymbol{r}$ are matrices formed by concatenating T_i, Q_i, and $\boldsymbol{r}_i$ for each accepted observation per Equations 124–126 [2, pg. 63]. In practice, these results are calculated using running summations inside programmatic loops as given in Algorithm 2, which summarizes the non-linear least squares implementation.

$$T \equiv \begin{bmatrix} T_1 \\ T_2 \\ \vdots \\ T_N \end{bmatrix} \tag{124}$$

$$Q \equiv \begin{bmatrix} Q_1 & 0 & \dots & 0 \\ 0 & Q_2 & \dots & 0 \\ \vdots & \vdots & \ddots & \vdots \\ 0 & 0 & \dots & Q_N \end{bmatrix} \tag{125}$$

$$\boldsymbol{r} \equiv \begin{bmatrix} \boldsymbol{r}_1 \\ \boldsymbol{r}_2 \\ \vdots \\ \boldsymbol{r}_N \end{bmatrix} \tag{126}$$

Once the correction $\delta\boldsymbol{X}(t_0)$ is available, it is applied to the previous initial state of the reference orbit and the process is iterated until it converges. In this implementation convergence is determined by examining the relative change in S which is the quantity minimized by the algorithm (S is akin to the sum of the squares of the error in a scalar case) and is given by Equation 127.

$$S = \boldsymbol{r}^T Q^{-1} \boldsymbol{r} \tag{127}$$

Again in practice running summations are used rather than the concatenated matrices $\boldsymbol{r}$ and Q.

The least squares algorithm was considered converged if the relative change in S between the current iteration j and the previous iteration $j-1$ was less than a threshold value S_{ratio}, as in Equation 128.

$$\frac{|S_j - S_{j-1}|}{S_{j-1}} < S_{\text{ratio}} \tag{128}$$

The value for S_{ratio} used in this research was 1×10^{-4}, or 0.01%.

Algorithm 2: Non-Linear Least Squares Estimation Algorithm

```
Data: Collection of observations $(\boldsymbol{z}_i, \boldsymbol{z}_{i+1}, \ldots, \boldsymbol{z}_n)$, reference orbit $\boldsymbol{X}_{\text{ref}}(t_0)$,
      $H$, $Q_i$
Result: Estimate of corrected state vector $\boldsymbol{X}_{\text{ref}}(t_0)$
while not converged do
    for each obs $i - 1$, starting at $i = 1$ to $n$ do
        numerically integrate $\boldsymbol{X}_{\text{ref}}(t_{i-1})$ and $\Phi(t_{i-1}, t_0)$ to $t_i$, yielding $\boldsymbol{X}_{\text{ref}}(t_i)$
          and $\Phi(t_i, t_0)$
        read observation $\boldsymbol{z}_i$
        calculate $T_i \equiv H\Phi(t_i, t_0)$
        calculate $\boldsymbol{z}_{i,\text{predicted}} = T_i \boldsymbol{X}_{\text{ref}}(t_0)$
        calculate residual $\boldsymbol{r}_i = \boldsymbol{z}_i - \boldsymbol{z}_{i,\text{predicted}}$
        add to running sums
            $T^T Q^{-1} T \mathrel{+}= T_i^T Q_i^{-1} T_i$
            $T^T Q^{-1} \boldsymbol{r} \mathrel{+}= T_i^T Q_i^{-1} \boldsymbol{r}_i$
            $S \mathrel{+}= \boldsymbol{r}_i^T Q_i^{-1} \boldsymbol{r}_i$
    end
    calculate $P_{\delta X}^{-1} = \sum_i T_i^T Q^{-1} T_i$
    invert $P_{\delta X}^{-1}$ to obtain $P_{\delta X}$
    calculate correction $\delta \boldsymbol{X}(t_0) = P_{\delta X} \left( \sum_i T_i^T Q^{-1} \boldsymbol{r}_i \right)$
    update current estimate $\boldsymbol{X}_{\text{ref}}(t_0) \leftarrow \boldsymbol{X}_{\text{ref}}(t_0) + \delta \boldsymbol{X}(t_0)$
    check convergence
    reset running sums
        $T^T Q^{-1} T = [0]$
        $T^T Q^{-1} \boldsymbol{r} = [0]$
        $S = 0$
end
```

Appendix C. Third Body Gravity Perturbations

The effects of a third astronomical body's gravitation on a satellite orbiting the Earth can be represented as the potential function given in Equation 129 [159, pg. 103]

$$V_3 = -\mu_3 \left(\frac{1}{\rho_{23}} - \frac{\boldsymbol{\rho}_3 \cdot \boldsymbol{\rho}}{\rho_3^3} \right) \tag{129}$$

where the reference frame is an inertial one centered at the Earth and μ_3 is the gravitational parameter of the third body, ρ_{23} is the magnitude of the relative position vector from the satellite to the third body, $\boldsymbol{\rho}_3$ is the position vector of the third body relative to the Earth and ρ_3 is its magnitude, and $\boldsymbol{\rho}$ is the position vector of the satellite relative to the Earth. Figure 42 depicts an example arrangement of objects and the relevant position vectors in which the moon is the third body. Relative position vectors from Earth to any major third body in the solar system (specifically the moon and the sun) were obtained using the SPICE library mentioned in Chapter III.

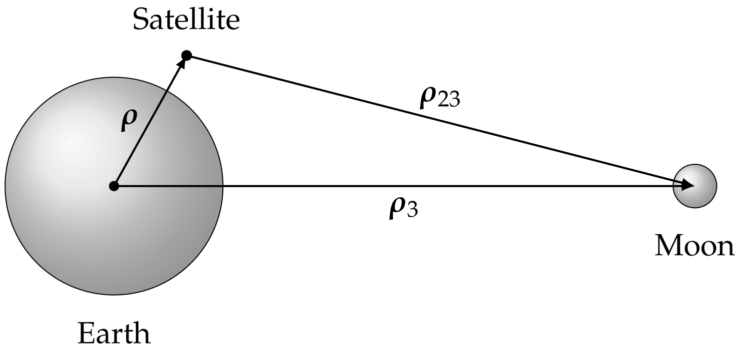

Figure 42. Third Body Perturbations Arrangement and Position Vector Example (Not to Scale)

In this case the relative positions of the third body and the satellite with respect to Earth are the same as their position vectors in the Earth-centered inertial frame, but ρ is used in place of r for consistency. Additionally, Wiesel notes that this formulation ignores the gravitational force exerted by the satellite on the third body, which in the case of a satellite is minuscule [159, pg. 103].

Applying Equation 129 to a satellite's equations of motion is done by calculating the first partials with respect to x, y, z and adding the results as additional acceleration terms in Equation 8. To compute these partial derivatives, let $\boldsymbol{\rho} = [x, y, z]^T$, $\boldsymbol{\rho}_3 = [s, t, u]^T$, and therefore $\boldsymbol{\rho}_{23} = \boldsymbol{\rho}_3 - \boldsymbol{\rho} = [(s-x), (t-y), (u-z)]^T$. Substituting into Equation 129 the yields

$$V_3 = -\mu_3 \left(\frac{1}{\sqrt{(s-x)^2 + (t-y)^2 + (u-z)^2}} - \frac{s\,x + t\,y + u\,z}{{\rho_3}^3} \right) \tag{130}$$

and the first partials required for the equations of motion are given in Equations 131–133.

$$\frac{\partial V_3}{\partial x} = -\mu_3 \left(\frac{s-x}{{\rho_{23}}^3} - \frac{s}{{\rho_3}^3} \right) \tag{131}$$

$$\frac{\partial V_3}{\partial y} = -\mu_3 \left(\frac{t-y}{{\rho_{23}}^3} - \frac{t}{{\rho_3}^3} \right) \tag{132}$$

$$\frac{\partial V_3}{\partial z} = -\mu_3 \left(\frac{u-z}{{\rho_{23}}^3} - \frac{u}{{\rho_3}^3} \right) \tag{133}$$

Regarding third-body gravity's contribution to the system's A matrix (see Chapter III and Appendix A), Equation 129 does not contain any velocity components or B^* so the third-body gravity contribution is limited to a 3×3 sub-block of the A matrix $A_{3\mathrm{B}}$ as in Equation 134.

$$A_{3\mathrm{B}}(t) = \begin{bmatrix} 0 & 0 & 0 & 0 & 0 & 0 & 0 \\ 0 & 0 & 0 & 0 & 0 & 0 & 0 \\ 0 & 0 & 0 & 0 & 0 & 0 & 0 \\ A_{3\mathrm{B},41} & A_{3\mathrm{B},42} & A_{3\mathrm{B},43} & 0 & 0 & 0 & 0 \\ A_{3\mathrm{B},51} & A_{3\mathrm{B},52} & A_{3\mathrm{B},53} & 0 & 0 & 0 & 0 \\ A_{3\mathrm{B},61} & A_{3\mathrm{B},62} & A_{3\mathrm{B},63} & 0 & 0 & 0 & 0 \\ 0 & 0 & 0 & 0 & 0 & 0 & 0 \end{bmatrix} \tag{134}$$

The second partials of the third-body potential are given by Equations 135–143.

$$A_{3\mathrm{B},41} = \frac{\partial^2 V_3}{\partial x^2} = -\mu_3 \left(\frac{3(s-x)^2}{{\rho_{23}}^5} - \frac{1}{{\rho_{23}}^3} \right) \tag{135}$$

$$A_{3\mathrm{B},42} = \frac{\partial^2 V_3}{\partial y \partial x} = -\mu_3 \left(\frac{3(s-x)(t-y)}{{\rho_{23}}^5} \right) \tag{136}$$

$$A_{3\mathrm{B},43} = \frac{\partial^2 V_3}{\partial z \partial x} = -\mu_3 \left(\frac{3(s-x)(u-z)}{{\rho_{23}}^5} \right) \tag{137}$$

$$A_{3\mathrm{B},51} = \frac{\partial^2 V_3}{\partial x \partial y} = A_{3\mathrm{B},42} \tag{138}$$

$$A_{3\mathrm{B},52} = \frac{\partial^2 V_3}{\partial y^2} = -\mu_3 \left(\frac{3(t-y)^2}{{\rho_{23}}^5} - \frac{1}{{\rho_{23}}^3} \right) \tag{139}$$

$$A_{3\mathrm{B},53} = \frac{\partial^2 V_3}{\partial z \partial y} = -\mu_3 \left(\frac{3(t-y)(u-z)}{{\rho_{23}}^5} \right) \tag{140}$$

$$A_{3\mathrm{B},61} = \frac{\partial^2 V_3}{\partial x \partial z} = A_{3\mathrm{B},43} \tag{141}$$

$$A_{3\mathrm{B},62} = \frac{\partial^2 V_3}{\partial y \partial z} = A_{3\mathrm{B},53} \tag{142}$$

$$A_{3\mathrm{B},63} = \frac{\partial^2 V_3}{\partial z^2} = -\mu_3 \left(\frac{3(u-z)^2}{{\rho_{23}}^5} - \frac{1}{{\rho_{23}}^3} \right) \tag{143}$$

Bibliography

[1] A. B. Poore, J. M. Aristoff, J. T. Horwood, R. Armellin, W. T. Cerven, Y. Cheng, C. M. Cox, R. S. Erwin, J. H. Frisbee, M. D. Hejduk, B. A. Jones, P. Di Lizia, D. J. Scheeres, D. A. Vallado, and R. M. Weisman. *Covariance and Uncertainty Realism in Space Surveillance and Tracking*. Tech. rep. Numerica Corporation Fort Collins United States, 2016.

[2] W. E. Wiesel. *Modern Orbit Determination*. CreateSpace Independent Publishing Platform, 2010.

[3] Inter-Agency Space Debris Coordination Committee. *IADC Space Debris Mitigation Guidelines*. Available online. 2007. URL: `https://www.unoosa.org/documents/pdf/spacelaw/sd/IADC-2002-01-IADC-Space_Debris-Guidelines-Revision1.pdf` (visited on 01/06/2020).

[4] United States Air Force. *Space Safety and Mishap Prevention Program*. Air Force Instruction. United States Air Force, 2014.

[5] D. A. Vallado. *Fundamentals of Astrodynamics and Applications*. Fourth Edition. Microcosm Press, 2013.

[6] L. Sagnieres and I. Sharf. "Uncertainty Characterization of Atmospheric Density Models for Orbit Prediction of Space Debris". In: *7th European Conference on Space Debris*. 1. 2017, pp. 18–21.

[7] E. M. Gaposchkin. *Calculation of satellite drag coefficients*. Tech. rep. Massachusetts Institute of Technology Lincoln Labs, 1994.

[8] D. A. Vallado and D. Finkleman. "A critical assessment of satellite drag and atmospheric density modeling". In: *Acta Astronautica* 95 (2014), pp. 141–165. DOI: `10.1016/j.actaastro.2013.10.005`.

[9] A. T. Rich, K. J. Stuart, and W. E. Wiesel. "Stochastic Dynamics of and Collision Prediction for Low Altitude Earth Satellites". In: *Journal of the Astronautical Sciences* 65.3 (2018), pp. 307–320. DOI: `10.1007/s40295-018-0129-9`.

[10] H. K. Karrenberg, E. Levin, and D. H. Lewis. "Variation of Satellite Position With Uncertainties in the Mean Atmospheric Density". In: *ARS Journal* 32.4 (1962), pp. 576–582. DOI: `10.2514/8.6071`.

[11] J. T. Emmert, J. Byers, H. Warren, and A. Segerman. "Propagation of Forecast Errors from the Sun to LEO Trajectories: How Does Drag Uncertainty Affect Conjunction Frequency?" In: *Advanced Maui Optical and Space Surveillance Technologies Conference*. 2014.

[12] J. T. Emmert, H. P. Warren, A. M. Segerman, J. M. Byers, and J. M. Picone. "Propagation of atmospheric density errors to satellite orbits". In: *Advances in Space Research* 59.1 (2017), pp. 147–165. DOI: `10.1016/j.asr.2016.07.036`.

[13] M. D. Hejduk and D. E. Snow. "The Effect of Neutral Density Estimation Errors on Satellite Conjunction Serious Event Rates". In: *Space Weather* 16.7 (2018), pp. 849–869. DOI: `10.1029/2017sw001720`.

[14] D. J. Lee and K. T. Alfriend. "Effect of atmospheric density uncertainty on collision probability". In: *Advances in the Astronautical Sciences* 105.II (2000), pp. 1255–1272.

[15] M. R. Akella, J. L. Junkins, and K. T. Alfriend. "Some consequences of force model uncertainty on probability of collision with orbital debris". In: *Advances in the Astronautical Sciences* 97.1 (1997), pp. 111–121.

[16] M. P. Wilkins and K. T. Alfriend. "Characterizing orbit uncertainty due to atmospheric uncertainty". In: *Astrodynamics Specialist Conference*. 2000, pp. 19–29. DOI: `10.2514/6.2000-3931`.

[17] C. D. Bussy-Virat, A. J. Ridley, and J. W. Getchius. "Effects of Uncertainties in the Atmospheric Density on the Probability of Collision Between Space Objects". In: *Space Weather* 16.5 (2018), pp. 519–537. DOI: `10.1029/2017sw001705`.

[18] C. Bussy-Virat, J. W. Getchius, and A. J. Ridley. "The Spacecraft Orbital Characterization Kit and its Applications to the CYGNSS Mission". In: *2018 Space Flight Mechanics Meeting*. American Institute of Aeronautics and Astronautics, 2018. DOI: `10.2514/6.2018-1973`.

[19] G. Scheifele and E. L. Stiefel. *Linear and Regular Celestial Mechanics*. 1st ed. Berlin: Springer-Verlag Berlin Heidelberg, 1971.

[20] F. Schiemenz, J. Utzmann, and H. Kayal. "Propagating EUV solar flux uncertainty to atmospheric density uncertainty". In: *Advances in Space Research* 63.12 (2019), pp. 3936–3952. DOI: `10.1016/j.asr.2019.02.040`.

[21] F. Schiemenz, J. Utzmann, and H. Kayal. "Least squares orbit estimation including atmospheric density uncertainty consideration". In: *Advances in Space Research* 63.12 (2019), pp. 3916–3935. DOI: `10.1016/j.asr.2019.02.039`.

[22] V. Szebehely and R. B. Curran. "The History and Background of Astrodynamics". In: *Acta Astronautica* 20 (1989), pp. 79–81.

[23] G. F. Gronchi. "Classical and modern orbit determination for asteroids". In: *Proceedings of the International Astronomical Union* 2004.IAUC196 (2004), pp. 293–303. DOI: `10.1017/s174392130500147x`.

[24] F. R. Hoots, P. W. Schumacher Jr., and R. A. Glover. "History of analytical orbit modeling in the US space surveillance system". In: *Journal of Guidance, Control, and Dynamics* 27.2 (2004), pp. 174–185.

[25] D. Brouwer. "Solution of the problem of artificial satellite theory without drag". In: *The Astronomical Journal* 64.1274 (1959), pp. 378–396. DOI: `10.1086/107958`.

[26] Y. Kozai. "The motion of a close earth satellite". In: *The Astronomical Journal* 64 (1959), pp. 367–377. DOI: `10.1086/107957`.

[27] R. H. Lyddane. "Small eccentricities or inclinations in the Brouwer theory of the artificial satellite". In: *The Astronomical Journal* 68 (1963), pp. 555–558. DOI: `10.1086/109179`.

[28] M. H. Lane and F. R. Hoots. *General Perturbations Theories Derived from the 1965 Lane Drag Theory*. Tech. rep. SPACETRACK Report No. 2. Aerospace Defense Command, 1979.

[29] F. R. Hoots and R. L. Roehrich. *Models for propagation of NORAD element sets*. Tech. rep. Aerospace Defense Command, 1980.

[30] Combined Force Space Component Command. *SGP4*. Available online. 2019. URL: `https://www.space-track.org/documentation%5C#sgp4` (visited on 08/25/2019).

[31] D. A. Vallado. *Astrodynamics Software*. Available online. 2019. URL: `https://www.celestrak.com/software/vallado-sw.php` (visited on 08/25/2019).

[32] D. A. Vallado, P. Crawford, R. Hujsak, and T. S. Kelso. "Revisiting Spacetrack Report #3". In: *AIAA/American Astronautical Society Astrodynamics Specialist Conference and Exhibit*. 2006. DOI: `10.2514/6.2006-6753`.

[33] E. Wnuk. "Recent progress in analytical orbit theories". In: *Advances in Space Research* 23.4 (1999), pp. 677–687. DOI: `10.1016/S0273-1177(99)00148-9`.

[34] A. Deprit and A. Rom. "The Main Problem of Artificial Satellite Theory for Small and Moderate Eccentricities". In: *Celestial Mechanics* 2.2 (1970), pp. 166–206. DOI: `10.1007/BF01229494`.

[35] K. Aksnes. "A Second-Order Artificial Satellite Theory Based on an Intermediate Orbit". In: *The Astronomical Journal* 75.9 (1970), pp. 1066–1094. DOI: `10.1086/111061`.

[36] H. Kinoshita. *Third-Order Solution of an Artificial-Satellite Theory*. Tech. rep. 1977.

[37] S. Coffey and A. Deprit. "Third-Order Solution to the Main Problem in Satellite Theory". In: *Journal of Guidance, Control, and Dynamics* 5.4 (1982), pp. 366–371. DOI: `10.2514/3.56183`.

[38] S. Breiter. "Second-Order Solution for the Zonal Problem of Satellite Theory". In: *Celestial Mechanics and Dynamical Astronomy* 67.3 (1997), pp. 237–249. DOI: `10.1023/A:1008234420951`.

[39] A. S. Sochilina. "On the Motion of a Satellite in Resonance with its Rotating Planet". In: *Celestial Mechanics* 26.4 (1981), pp. 337–352. DOI: `10.1007/BF01230415`.

[40] M. T. Lane. "An Analytical Treatment of Resonance Effects on Satellite Orbits". In: *Celestial Mechanics* 42 (1988).

[41] F. Delhaise and J. Henrard. “The Problem of Critical Inclination Combined with a Resonance in Mean Motion in Artificial Satellite Theory”. In: *Celestial Mechanics & Dynamical Astronomy* 55.3 (1993), pp. 261–280. DOI: `10.1007/BF00692514`.

[42] V. R. Bond. “The Uniform, Regular Differential Equations of the KS Transformed Perturbed Two-Body Problem”. In: *Celestial Mechanics* 10.3 (1974), pp. 303–318. DOI: `10.1007/BF01586860`.

[43] R. C. Engels and J. L. Junkins. “The gravity-perturbed Lambert problem - A KS variation of parameters approach”. In: *Celestial Mechanics* 24 (1981), pp. 3–21. DOI: `10.1007/BF01228790`.

[44] M. X. J. Raj and R. K. Sharma. “Analytical orbit predictions with air drag using KS uniformly regular canonical elements”. In: *Planetary and Space Science* 54.3 (2006), pp. 310–316. DOI: `10.1016/j.pss.2005.12.006`.

[45] R. K. Sharma. “Analytical Approach Using KS Elements to Near-Earth Orbit Predictions Including Drag”. In: *Proceedings: Mathematical and Physical Sciences* 433.1887 (1991), pp. 121–130. DOI: `10.1098/rspa.1991.0038`.

[46] V. Martinusi, L. Dell’Elce, and G. Kerschen. “Analytic propagation of near-circular satellite orbits in the atmosphere of an oblate planet”. In: *Celestial Mechanics and Dynamical Astronomy* 123.1 (2015), pp. 85–103. DOI: `10.1007/s10569-015-9630-7`.

[47] M. Lara, J. F. San-Juan, L. M. López-Ochoa, and P. Cefola. “Long-term evolution of Galileo operational orbits by canonical perturbation theory”. In: *Acta Astronautica* 94.2 (2014), pp. 646–655. DOI: `10.1016/j.actaastro.2013.09.008`.

[48] O. Montenbruck. “Numerical Integration Methods for Orbital Motion”. In: *Celestial Mechanics and Dynamical Astronomy* 53.1 (1992), pp. 59–69. DOI: `10.1007/BF00049361`.

[49] B. K. Bradley, B. A. Jones, G. Beylkin, and P. Axelrad. “A new numerical integration technique in astrodynamics”. In: *Advances in the Astronautical Sciences* 143 (2012), pp. 1709–1728.

[50] B. K. Bradley, B. A. Jones, G. Beylkin, K. Sandberg, and P. Axelrad. “Bandlimited implicit Runge-Kutta integration for Astrodynamics”. In: *Celestial Mechanics and Dynamical Astronomy* 119.2 (2014), pp. 143–168. DOI: `10.1007/s10569-014-9551-x`.

[51] B. A. Jones and R. L. Anderson. “A survey of symplectic and collocation integration methods for orbit propagation”. In: *Advances in the Astronautical Sciences* 143 (2012), pp. 1669–1688.

[52] W. E. Wiesel. “A Theory of Low Eccentricity Earth Satellite Motion”. In: *Journal of the Astronautical Sciences* 59 (2012), pp. 629–649. DOI: `10.1007/s40295-014-0007-z`.

[53] S. J. Setty, P. J. Cefola, O. Montenbruck, and H. Fiedler. “Application of Semi-analytical Satellite Theory orbit propagator to orbit determination for space object catalog maintenance”. In: *Advances in Space Research* 57.10 (2016), pp. 2218–2233. DOI: `10.1016/j.asr.2016.02.028`.

[54] J. G. J. Neelon, P. J. Cefola, and R. J. Proulx. “Current development of the Draper Semianalytical Satellite Theory standalone orbit propagator package”. In: *Advances in the Astronautical Sciences* 97.January 1997 (2018), pp. 2037–2052.

[55] M. Lara, J. F. San-Juan, L. M. López, and P. J. Cefola. “On the third-body perturbations of high-altitude orbits”. In: *Celestial Mechanics and Dynamical Astronomy* 113.4 (2012), pp. 435–452. DOI: `10.1007/s10569-012-9433-z`.

[56] T. Nie, P. Gurfil, and S. Zhang. “Semi-analytical model for third-body perturbations including the inclination and eccentricity of the perturbing body”. In: *Celestial Mechanics and Dynamical Astronomy* 131.6 (2019), pp. 1–31. DOI: `10.1007/s10569-019-9905-5`.

[57] Y. Zhong-Luo and Z. Yang. “A review of uncertainty propagation in orbital mechanics”. In: *Progress in Aerospace Sciences* 89.September 2016 (2017), pp. 23–39. DOI: `10.1016/j.paerosci.2016.12.002`.

[58] D. K. Geller. “Linear covariance techniques for orbital rendezvous analysis and autonomous onboard mission planning”. In: *Journal of Guidance, Control, and Dynamics* 29.6 (2006), pp. 1404–1414. DOI: `10.2514/1.19447`.

[59] D. K. Geller, M. Ben Rose, and D. C. Woffinden. “Event triggers in linear covariance analysis with applications to orbital rendezvous”. In: *Journal of Guidance, Control, and Dynamics* 32.1 (2009), pp. 102–111. DOI: `10.2514/1.36834`.

[60] S. Lee, H. Lyu, and I. Hwang. “Analytical uncertainty propagation for satellite relative motion along elliptic orbits”. In: *Journal of Guidance, Control, and Dynamics* 39.7 (2016), pp. 1593–1601. DOI: `10.2514/1.G001848`.

[61] N. Arora, V. Vittaldev, and R. P. Russell. “Parallel computation of trajectories using graphics processing units and interpolated gravity models”. In: *Journal of Guidance, Control, and Dynamics* 38.8 (2015), pp. 1345–1355. DOI: `10.2514/1.G000571`.

[62] J. L. Junkins, M. R. Akella, and K. T. Alfriend. “Non-Gaussian error propagation in orbital mechanics”. In: *Journal of the Astronautical Sciences* 44.4 (1996), pp. 541–563.

[63] C. Sabol, K. Hill, K. Alfriend, and T. Sukut. “Nonlinear effects in the correlation of tracks and covariance propagation”. In: *Acta Astronautica* 84 (2013), pp. 69–80. DOI: `10.1016/j.actaastro.2012.08.023`.

[64] J. L. Junkins and P. Singla. "How nonlinear is it? A tutorial on nonlinearity of orbit and attitude dynamics". In: *Journal of the Astronautical Sciences* 52.1-2 (2004), pp. 7–60.

[65] D. J. Scheeres, F.-Y. Hsiao, R. S. Park, B. F. Vilac, and J. M. Maruskin. "Fundamental limits on spacecraft orbit uncertainty and distribution propagation". In: *Journal of the Astronautical Sciences* 54.3-4 (2006), pp. 505–523.

[66] G. Terejanu, P. Singla, T. Singh, and P. D. Scott. "Uncertainty propagation for nonlinear dynamic systems using gaussian mixture models". In: *Journal of Guidance, Control, and Dynamics* 31.6 (2008), pp. 1623–1633. DOI: `10.2514/1.36247`.

[67] J. T. Horwood, N. D. Aragon, A. B. Poore, J. T. Horwood, N. D. Aragon, and A. B. Poore. "Gaussian Sum Filters for Space Surveillance: Theory and Simulations". In: *Journal of Guidance, Control, and Dynamics* 34.6 (2011), pp. 1839–1851. DOI: `10.2514/1.53793`.

[68] K. J. DeMars. "Nonlinear orbit uncertainty prediction and rectification for space situational awareness". PhD thesis. University of Texas at Austin, 2010.

[69] K. J. DeMars, Y. Cheng, R. H. Bishop, and M. Jah. "Methods for splitting Gaussian distributions and applications within the AEGIS filter". In: *Advances in the Astronautical Sciences* 143 (2012), pp. 2379–2398.

[70] K. J. DeMars, R. H. Bishop, and M. K. Jah. "Entropy-based approach for uncertainty propagation of nonlinear dynamical systems". In: *Journal of Guidance, Control, and Dynamics* 36.4 (2013), pp. 1047–1057. DOI: `10.2514/1.58987`.

[71] S. J. Julier, J. K. Uhlmann, and H. F. Durrant-Whyte. "A New approach for filtering nonlinear systems". In: *Proceedings of the American Control Conference* 3.June (1995), pp. 1628–1632. DOI: `10.1109/acc.1995.529783`.

[72] S. J. Julier, J. K. Uhlmann, and H. F. Durrant-Whyte. "A New Method for the Nonlinear Transformation of Means and Covariances in Filters and Estimators". In: *IEEE Transactions on Automatic Control* 45.3 (2000), pp. 477–482. DOI: `10.1109/TAC.1985.1104072`.

[73] D. A. V. Raihan and S. Chakravorty. "An Unscented Kalman-Particle Hybrid Filter for Space Object Tracking". In: *Journal of the Astronautical Sciences* 65.1 (2018), pp. 111–134.

[74] D. B. Xiu and G. E. Karniadakis. "The Wiener-Askey polynomial chaos for stochastic differential equations". In: *SIAM Journal on Scientific Computing* 24.2 (2002), pp. 619–644.

[75] B. A. Jones, A. Doostan, and G. H. Born. "Nonlinear propagation of orbit uncertainty using non-intrusive polynomial chaos". In: *Journal of Guidance, Control, and Dynamics* 36.2 (2013), pp. 430–444. DOI: `10.2514/1.57599`.

[76] B. A. Jones and A. Doostan. “Satellite collision probability estimation using polynomial chaos expansions”. In: *Advances in Space Research* 52.11 (2013), pp. 1860–1875. DOI: `10.1016/j.asr.2013.08.027`.

[77] B. A. Jones, N. Parrish, and A. Doostan. “Postmaneuver collision probability estimation using sparse polynomial chaos expansions”. In: *Journal of Guidance, Control, and Dynamics* 38.8 (2015), pp. 1425–1437. DOI: `10.2514/1.G000595`.

[78] R. S. Park and D. J. Scheeres. “Nonlinear mapping of Gaussian statistics: Theory and applications to spacecraft trajectory design”. In: *Journal of Guidance, Control, and Dynamics* 29.6 (2006), pp. 1367–1375. DOI: `10.2514/1.20177`.

[79] R. S. Park and D. J. Scheeres. “Nonlinear semi-analytic methods for trajectory estimation”. In: *Journal of Guidance, Control, and Dynamics* 30.6 (2007), pp. 1668–1676. DOI: `10.2514/1.29106`.

[80] M. Majji, J. L. Junkins, and J. Turner. “A High Order Method for Estimation of Dynamic Systems”. In: *Journal of the Astronautical Sciences* 56.3 (2008), pp. 401–440.

[81] I. Park, K. Fujimoto, and D. J. Scheeres. “Effect of dynamical accuracy for uncertainty propagation of perturbed keplerian motion”. In: *Journal of Guidance, Control, and Dynamics* 38.12 (2015), pp. 2287–2300. DOI: `10.2514/1.G000956`.

[82] I. Park. “Dynamical Realism and Uncertainty Propagation”. PhD thesis. University of Colorado, 2015.

[83] B. A. Jones and R. Weisman. “Multi-fidelity orbit uncertainty propagation”. In: *Acta Astronautica* 155 (2019), pp. 406–417. DOI: `10.1016/j.actaastro.2018.10.023`.

[84] J. M. Aristoff, J. T. Horwood, and A. B. Poore. “Implicit-Runge-Kutta-based methods for fast, precise, and scalable uncertainty propagation”. In: *Celestial Mechanics and Dynamical Astronomy* 122.2 (2015), pp. 169–182. DOI: `10.1007/s10569-015-9614-7`.

[85] V. Vittaldev, R. P. Russell, and R. Linares. “Spacecraft uncertainty propagation using Gaussian mixture models and Polynomial chaos expansions”. In: *Journal of Guidance, Control, and Dynamics* 39.12 (2016), pp. 2615–2626. DOI: `10.2514/1.G001571`.

[86] T. S. Kelso. “Validation of SGP4 and IS-GPS-200D against GPS precision ephemerides”. In: *17th AAS/AIAA Spaceflight Mechanics Conference, Sedona, AZ, USA*. 2007.

[87] G. E. Peterson, R. G. Gist, and D. L. Oltrogge. "Covariance Generation for Space Objects Using Public Data". In: *Proceedings of the 11 th Annual American Astronautical Society/AIAA Space Flight Mechanics Meeting, Santa Barbara, CA*. 2001, pp. 201–214.

[88] J. Geul, E. Mooij, and R. Noomen. "TLE uncertainty estimation using robust weighted differencing". In: *Advances in Space Research* 59.10 (2017), pp. 2522–2535. DOI: `10.1016/j.asr.2017.02.038`.

[89] V. P. Osweiler. "Covariance estimation and autocorrelation of NORAD two-line element sets". MA thesis. Air Force Institute of Technology, Wright Patterson AFB, OH, 2006.

[90] Y. Hyeon-Jeong and C. Dae-Won. "Validation on residual variation and covariance matrix of USSTRATCOM two line element". In: *Journal of Astronomy and Space Science* 29.3 (2012), pp. 287–293. DOI: `10.5140/JASS.2012.29.3.287`.

[91] S. G. Hesar, M. Duncan, and J. H. Pawloski. "Realistic covariance generation for the GPM spacecraft". In: *15th International Conference on Space Operations, 2018* (2018). DOI: `10.2514/6.2018-2699`.

[92] F. A. Marcos, M. J. Kendra, J. M. Griffin, J. N. Bass, D. R. Larson, and J. J. F. Liu. "Precision low earth orbit determination using atmospheric density calibration". In: *Advances in the Astronautical Sciences* 97.Part 1 (1997), pp. 501–506.

[93] A. L. Nazarenko, P. J. Cefola, and V. Yurasov. "Estimating atmosphere density variations to improve leo orbit prediction accuracy". In: *Advances in the Astronautical Sciences* 99.2 (1998), pp. 1235–1256.

[94] C. A. McLaughlin, A. Hiatt, and T. Lechtenberg. "Precision Orbit Derived Total Density". In: *Journal of Spacecraft and Rockets* 48.1 (2011), pp. 166–174. DOI: `10.2514/1.47624`.

[95] C. A. McLaughlin, T. Lechtenberg, E. Fattig, and D. M. Krishna. "Estimating Density Using Precision Satellite Orbits from Multiple Satellites". In: *The Journal of the Astronautical Sciences* 59.1-2 (2012). DOI 10.1007/s40295-013-0007-4, pp. 84–100.

[96] J. Hinks and M. Psiaki. "Simultaneous Orbit and Atmospheric Density Estimation for a Satellite Constellation". In: *AIAA/AAS Astrodynamics Specialist Conference*. 2010. DOI: `10.2514/6.2010-8258`.

[97] M. F. Storz, B. R. Bowman, J. I. Branson, S. J. Casali, and W. K. Tobiska. "High accuracy satellite drag model (HASDM)". In: *Advances in Space Research* 36.12 (2005), pp. 2497–2505. DOI: `10.1016/j.asr.2004.02.020`.

[98] J. R. Wright and J. Woodburn. "Simultaneous real-time estimation of atmospheric density and ballistic coefficient". In: *Advances in the Astronautical Sciences*. Vol. 119. 2005, pp. 1155–1183.

[99] L. Dell'Elce, M. Arnst, and G. Kerschen. "Probabilistic Assessment of the Lifetime of Low-Earth-Orbit Spacecraft: Uncertainty Characterization". In: *Journal of Guidance, Control, and Dynamics* 38.5 (2015), pp. 900–912. DOI: `10.2514/1.g000148`.

[100] R. L. Anderson, G. H. Born, and J. M. Forbes. "Sensitivity of orbit predictions to density variability". In: *Journal of Spacecraft and Rockets* 46.6 (2009), pp. 1214–1230. DOI: `10.2514/1.42138`.

[101] R. L. Anderson, C. P. Guignet, G. H. Born, and J. M. Forbes. "Effect of density model time-delay errors on orbit prediction". In: *Journal of Spacecraft and Rockets* 50.5 (2013), pp. 1096–1105. DOI: `10.2514/1.A32368`.

[102] J. M. Leonard, J. M. Forbes, and G. H. Born. "Impact of tidal density variability on orbital and reentry predictions". In: *Space Weather* 10.12 (2012). DOI: `10.1029/2012SW000842`.

[103] F. L. Markley, E. D. Seidewitz, and M. Nicholson. "A general model for attitude determination error analysis". In: *Flight Mechanics (Estimation Theory Symposium 1988)*. 1988, pp. 3–25.

[104] F. L. Markley, E. D. Seidewitz, and J. Deutschmann. "Attitude determination error analysis - General model and specific application". In: *Proceedings of the International Symposium, Toulouse, France, Nov. 6-10, 1989 (A91-12276 02-12)*. 1990, pp. 251–266.

[105] J. Woodburn and V. Coppola. "Effect of coordinate selection on orbit determination". In: *AAS/AIAA Spaceflight Mechanics Meeting*. 2013.

[106] K. Hill, K. T. Alfriend, and C. Sabol. "Covariance-based Uncorrelated Track association". In: *AIAA/AAS Astrodynamics Specialist Conference and Exhibit* (2008). DOI: `10.2514/6.2008-7211`.

[107] V. T. Coppola and S. Tanygin. "Using bent ellipsoids to represent large position covariance in orbit propagation". In: *Journal of Guidance, Control, and Dynamics* 38.9 (2015), pp. 1775–1784. DOI: `10.2514/1.G001011`.

[108] K. Hill, C. Sabol, and K. T. Alfriend. "Comparison of Covariance-Based Track Association Approaches Using Simulated Radar Data". In: *Journal of the Astronautical Sciences* 59.1-2 (2012), pp. 287–306. DOI: `10.1007/s40295-013-0018-1`.

[109] S. Tanygin. "Efficient Covariance Interpolation Using Blending of Approximate Covariance Propagations". In: *Journal of the Astronautical Sciences* 61.1 (2014), pp. 107–132. DOI: `10.1007/s40295-015-0041-5`.

[110] D. A. Vallado and S. Alfano. "Curvilinear coordinate transformations for relative motion". In: *Celestial Mechanics and Dynamical Astronomy* 118.3 (2014), pp. 253–271. DOI: `10.1007/s10569-014-9531-1`.

[111] Combined Force Space Component Command. *Satellite Box Score*. Available online. 2020. URL: `https://www.space-track.org/basicspacedata/query/class/boxscore/format/html` (visited on 06/01/2021).

[112] Y. Kozai. "Second-order solution of artificial satellite theory without air drag". In: *The Astronomical Journal* 67 (1962), pp. 446–461. DOI: `10.1086/108753`.

[113] M. X. J. Raj and R. K. Sharma. "Analytical short-term orbit prediction with J2, J3, J4in terms of K-S uniformly regular canonical elements". In: *Advances in Space Research* 31.8 (2003), pp. 2019–2025. DOI: `10.1016/S0273-1177(03)00175-3`.

[114] J. H. Frisbee. "An Empirical State Error Covariance Matrix for the Weighted Least Squares Estimation Method". In: (2019), pp. 1–18.

[115] G. Casella and R. L. Berger. *Statistical Inference*. 2e. Duxbury Press, 2002.

[116] P. S. Maybeck. *Stochastic Models, Estimation, and Control Volume 1*. Academic Press, 1979.

[117] B. Ristic, S. Arulampalam, and N. Gordon. *Beyond the Kalman Filter: Particle Filters for Tracking Applications*. Artech House, 2003.

[118] N. Wiener. "The Homogeneous Chaos". In: *American Journal of Mathematics* 60.4 (1938), pp. 897–936.

[119] L. G. Jacchia. *Thermospheric temperature, density, and composition: New models*. Tech. rep. Cambridge, MA, United States: Smithsonian Astrophysical Observatory, 1977.

[120] D. J. C. Jara, J. A. S. Torrico, and O. L. R. Suárez. "Atmospheric density uncertainty effects on the orbital lifetime estimation for CubeSats at LEO". In: (2017). arXiv: `1709.09128v2`.

[121] J. Geul, E. Mooij, and R. Noomen. "Analysis of Uncertainties and Modeling in Short-Term Reentry Predictions". In: *Journal of Guidance, Control, and Dynamics* 41.6 (2018), pp. 1276–1289. DOI: `10.2514/1.g003258`.

[122] Analytical Graphics, Inc. *STK Covariance*. Available online. 2019. URL: `http://help.agi.com/stk/index.htm#hpop/hpop-covariance.htm` (visited on 12/13/2019).

[123] The GMAT Development Team. *General Mission Analysis Tool (GMAT)*. Available online. 2019. URL: `http://gmat.sourceforge.net/docs/R2017a/help.html#Propagator_ForceModel` (visited on 12/13/2019).

[124] a.i. solutions. *Atmospheric Forces*. Available online. 2019. URL: `https://ai-solutions.com/_help_Files/atmospheric_forces.htm` (visited on 12/13/2019).

[125] D. Gaylor, R. Page, and K. Bradley. "Testing of the Java Astrodynamics Toolkit Propagator". In: *AIAA/AAS Astrodynamics Specialist Conference and Exhibit*. 2006. DOI: `10.2514/6.2006-6754`.

[126] Combined Force Space Component Command. *Two Line Element (TLE) Data*. Available online. 2020. URL: `https://www.space-track.org/` (visited on 07/07/2020).

[127] R. A. Eckman, A. J. Brown, D. R. Adamo, and R. G. Gottlieb. *Normalization and Implementation of Three Gravitational Acceleration Models*. Tech. rep. NASA Johnson Space Center, Houston, Texas, 2016.

[128] S. Pines. "Uniform representation of the gravitational potential and its derivatives". In: *AIAA Journal* 11.11 (1973), pp. 1508–1511. DOI: `10.2514/3.50619`.

[129] F. G. Lemoine, D. E. Smith, L. Kunz, R. Smith, E. C. Pavlis, N. K. Pavlis, S. M. Klosko, D. S. Chinn, M. H. Torrence, R. G. Williamson, C. M. Cox, K. E. Rachlin, Y. M. Wang, S. C. Kenyon, R. Salman, R. Trimmer, R. H. Rapp, and R. S. Nerem. *The Development of the Joint NASA GSFC and the National Imagery and Mapping Agency (NIMA) Geopotential Model EGM96*. Tech. rep. July. Greenbelt, MD United States.: NASA Goddard Space Flight Center, 1998. DOI: `10.1007/978-3-662-03482-8_62`.

[130] S. M. Anandakrishnan and F. F. Regan. *Dynamics of Atmospheric Re-Entry*. American Institute of Aeronautics and Astronautics, 1993.

[131] N. K. Pavlis, S. A. Holmes, S. C. Kenyon, and J. K. Factor. "The development and evaluation of the Earth Gravitational Model 2008 (EGM2008)". In: *Journal of Geophysical Research: Solid Earth* 117.B4 (2012). DOI: `10.1029/2011JB008916`.

[132] J. M. Picone, A. E. Hedin, D. P. Drob, and A. C. Aikin. "NRLMSISE-00 empirical model of the atmosphere: Statistical comparisons and scientific issues". In: *Journal of Geophysical Research: Space Physics* 107.A12 (2002), SIA–15. DOI: `10.1029/2002JA009430`.

[133] L. F. Shampine and M. K. Gordon. *Computer solution of ordinary differential equations: the initial value problem*. Freeman, 1975.

[134] L. F. Shampine and M. W. Reichelt. "The MATLAB ODE suite". In: *SIAM Journal on Scientific Computing* 18.1 (1997), pp. 1–22.

[135] The MathWorks, Inc. *ode113*. Available online. 2019. URL: `https://www.mathworks.com/help/matlab/ref/ode113.html` (visited on 01/11/2020).

[136] J. Burkardt. *Shampine and Gordon ODE Solver*. Available online. 2012. URL: `https://people.sc.fsu.edu/~jburkardt/cpp_src/ode/ode.html` (visited on 07/22/2019).

[137] *CHAMP (Challenging Minisatellite Payload) CHAMP*. Available online. 2019. URL: `https://earth.esa.int/web/eoportal/satellite-missions/c-missions/champ` (visited on 07/13/2019).

[138] A. Helm. *CHAMP Mission and Orbit*. Available online. 2000. URL: `http://op.gfz-potsdam.de/champ/orbit/index_PRD.html` (visited on 01/09/2020).

[139] NASA. *Challenging Mini-satellite Payload (CHAMP)*. Available online. URL: `https://eospso.nasa.gov/sites/default/files/sat/CHAMP.jpg` (visited on 08/09/2021).

[140] *GRACE Mission Overview*. Available online. 2019. URL: `https://www.nasa.gov/mission%7B%5C_%7Dpages/Grace/overview/index.html` (visited on 07/15/2019).

[141] *GRACE 1*. Available online. 2021. URL: `https://nssdc.gsfc.nasa.gov/nmc/spacecraft/displayTrajectory.action?id=2002-012A` (visited on 05/14/2021).

[142] NASA. *Gravity Recovery and Climate Experiment (GRACE)*. Available online. URL: `https://www.nasa.gov/sites/default/files/images/623369main_pia04236-full_full.jpg` (visited on 08/09/2021).

[143] Earth Observation Portal. *GPIM (Green Propellant Infusion Mission) / STP-2*. Available online. 2020. URL: `https://directory.eoportal.org/web/eoportal/satellite-missions/g/gpim` (visited on 04/13/2020).

[144] NASA. *Green Propellant Infusion Mission (GPIM)*. Available online. URL: `https://www.nasa.gov/sites/default/files/thumbnails/image/gpim_updated.jpg` (visited on 08/09/2021).

[145] R. Konig. *Format Description: The CHAMP Orbit Format CHORB*. Tech. rep. GeoForschungsZentrum Potsdam, 2001.

[146] G. Michalak and R. König. "Rapid Science Orbits for CHAMP and GRACE Radio Occultation Data Analysis". In: *System Earth via Geodetic-Geophysical Space Techniques*. Berlin, Heidelberg: Springer Berlin Heidelberg, 2010, pp. 67–77. DOI: `10.1007/978-3-642-10228-8_6`.

[147] M. Rothacher. *CHAMP Postprocessed Science Orbit for GPS and CHAMP*. Information System and Data Center, GeoForschungszentrum Potsdam. Germany, 2000. DOI: `10.1594/GFZ.ISDC.CHAMP/CH-OG-4-PSO`.

[148] *Penticton Solar Radio Flux at 10.7cm, Time Series*. Available online. Boulder, CO: LASP Interactive Solar Irradiance Datacenter, University of Colorado, 2020. URL: `http://lasp.colorado.edu/lisird/data/penticton_radio_flux/` (visited on 07/16/2020).

[149] J. Matzka, O. Bronkalla, K. Tornow, K. Elger, and C. Stolle. *Geomagnetic Kp index*. GeoForschungszentrum Potsdam Data Services. Germany, 2020. DOI: `10.5880/Kp.0001`.

[150] C. H. Acton. "Ancillary Data Services of NASA's Navigation and Ancillary Information Facility". In: *Planetary and Space Science* 44.1 (1996), pp. 65–70. DOI: `10.1016/0032-0633(95)00107-7`.

[151] C. Acton, N. Bachman, B. Semenov, and E. Wright. "A look toward the future in the handling of space science mission geometry". In: *Planetary and Space Science* 150 (2017), pp. 9–12. DOI: `10.1016/j.pss.2017.02.013`.

[152] O. A. Vanli and C. N. Taylor. "Covariance Estimation for Factor Graph Based Bayesian Estimation". In: *2020 IEEE 23rd International Conference on Information Fusion (FUSION)*. IEEE. 2020. DOI: `10.23919/FUSION45008.2020.9190223`.

[153] J. Duník, O. Straka, O. Kost, and J. Havlík. "Noise covariance matrices in state-space models: A survey and comparison of estimation methods—Part I". In: *International Journal of Adaptive Control and Signal Processing* 31.11 (2017), pp. 1505–1543. DOI: `10.1002/acs.2783`.

[154] S. Sarkka. "On Unscented Kalman Filtering for State Estimation of Continuous-Time Nonlinear Systems". In: *IEEE Transactions on Automatic Control* 52.9 (2007), pp. 1631–1641. DOI: `10.1109/tac.2007.904453`.

[155] E. A. Wan and R. Van Der Merwe. "The unscented Kalman filter for nonlinear estimation". In: *Proceedings of the IEEE 2000 Adaptive Systems for Signal Processing, Communications, and Control Symposium (Cat. No. 00EX373)*. IEEE. 2000, pp. 153–158.

[156] R. Van Der Merwe and E. A. Wan. "The square-root unscented Kalman filter for state and parameter-estimation". In: *2001 IEEE International Conference on Acoustics, Speech, and Signal Processing. Proceedings (Cat. No. 01CH37221)*. Vol. 6. IEEE. 2001, pp. 3461–3464.

[157] C. Van Loan. "Computing integrals involving the matrix exponential". In: *IEEE Transactions on Automatic Control* 23.3 (1978), pp. 395–404.

[158] R. G. Brown and P. Y. C. Hwang. *Introduction to Random Signals and Applied Kalman Filtering, 3rd Edition*. John Wiley & Sons, 1997.

[159] W. E. Wiesel. *Modern Astrodynamics*. CreateSpace Independent Publishing Platform, 2010.

REPORT DOCUMENTATION PAGE

Form Approved
OMB No. 0704–0188

1. REPORT DATE *(DD–MM–YYYY)*	**2. REPORT TYPE**	**3. DATES COVERED** *(From — To)*
08–01–2021	Doctoral Dissertation	Sept 2018 — Sept 2021

4. TITLE AND SUBTITLE Stochastic Satellite Air Drag with the Ballistic Coefficient as a Random Variable	**5a. CONTRACT NUMBER** **5b. GRANT NUMBER** **5c. PROGRAM ELEMENT NUMBER**
6. AUTHOR(S) Everett B. Palmer IV, Maj, USAF	**5d. PROJECT NUMBER** **5e. TASK NUMBER** **5f. WORK UNIT NUMBER**
7. PERFORMING ORGANIZATION NAME(S) AND ADDRESS(ES) Air Force Institute of Technology Graduate School of Engineering and Management (AFIT/EN) 2950 Hobson Way WPAFB OH 45433-7765	**8. PERFORMING ORGANIZATION REPORT NUMBER** AFIT-ENY-DS-21-S-103
9. SPONSORING / MONITORING AGENCY NAME(S) AND ADDRESS(ES) Department of Aeronautics and Astronautics 2950 Hobson Way WPAFB OH 45433-7765 DSN 271-0690, COMM 937-255-3636 Email: william.wiesel@afit.edu	**10. SPONSOR/MONITOR'S ACRONYM(S)** AFIT/ENY **11. SPONSOR/MONITOR'S REPORT NUMBER(S)**

12. DISTRIBUTION / AVAILABILITY STATEMENT

DISTRIBUTION STATEMENT A:
APPROVED FOR PUBLIC RELEASE; DISTRIBUTION UNLIMITED.

13. SUPPLEMENTARY NOTES

14. ABSTRACT

The drag acceleration caused by the Earth's atmosphere is a significant cause of prediction uncertainty for low Earth orbit satellites. Most existing research has focused on improving deterministic atmospheric density predictions or on density as a random variable. This research investigates a new paradigm and focuses on modeling the uncertainty caused by air drag using the ballistic coefficient, a component of air drag that is independent of the model used to predict atmospheric density. Time series of ballistic coefficient values are calculated and analyzed as random processes. These random processes are then used as the foundation of a stochastic satellite prediction model that calculates the parameters of the random process and predicts satellite orbits with realistic uncertainty. The model is developed using the Unscented Transform and is validated using Monte Carlo simulation and empirical analysis, and proves effective for any choice of atmospheric density model and a variety of dynamical formulations.

15. SUBJECT TERMS

Stochastic Astrodynamics, Satellite Air Drag, Orbit Prediction

16. SECURITY CLASSIFICATION OF:			**17. LIMITATION OF ABSTRACT**	**18. NUMBER OF PAGES**	**19a. NAME OF RESPONSIBLE PERSON**
a. REPORT	**b. ABSTRACT**	**c. THIS PAGE**			Dr. William E. Wiesel, AFIT/ENY
U	U	U	U	176	**19b. TELEPHONE NUMBER** *(include area code)* (937) 255-3636; william.wiesel@afit.edu